EXHIBIT 10

ACS central science

ACS AUTHORCHOICE

Research Article

Cite This: ACS Cent. Sci. 2019, 5, 1079−1084

Targeted Protein Internalization and Degradation by ENDosome TArgeting Chimeras (ENDTACs)

Dhanusha A. Nalawansha,[†] Stacey-Lynn Paiva,[†] Diane N. Rafizadeh,[‡] Mariell Pettersson,[†] Liena Qin,[†] and Craig M. Crews*[,†,‡,§]

[†]Department of Molecular, Cellular and Developmental Biology, Yale University, 219 Prospect Street, New Haven, Connecticut 06511, United States

[‡]Department of Chemistry, Yale University, New Haven, Connecticut 06511, United States

[§]Department of Pharmacology, Yale University, New Haven, Connecticut 06511, United States

ACS Cent. Sci. **2020**, *6*, DOI: 10.1021/acscentsci.0c00021

Supporting Information

ABSTRACT: Targeted protein degradation has generated excitement in chemical biology and drug discovery throughout academia and industry. By hijacking the machinery responsible for protein degradation via the ubiquitin proteasome system (UPS), various cellular targets have been selectively degraded. However, since the tools used, often termed PROteolysis TArgeting Chimeras (PROTACs), hijack the intracellular quality control machinery, this technology can only access targets within the cell. Extracellular targets such as growth factors, cytokines, and chemokines bind to cell surface receptors, often initiating aberrant signaling in multiple diseases such as cancer and inflammation. However, efforts to develop small molecule inhibitors for these extracellular target proteins have been challenging. Herein, we developed a proof-of-concept approach to evaluate if extracellular proteins can be internalized and degraded via the receptor-mediated endolysosomal pathway. Using a heterodimeric molecule, termed "ENDosome TArgeting Chimera" (ENDTAC), internalization and degradation of an extracellular recombinant eGFP-HT7 fusion protein was achieved by hijacking the decoy GPCR receptor, CXCR7. This proof-of-concept study suggests that using ENDTACs to co-opt the endosomal−lysosomal degradation pathway, in contrast to PROTACs using the UPS, may provide an avenue for degrading extracellular targets such as cytokines. Overall, the technology described herein provides a novel expansion to the field of targeted protein degradation.

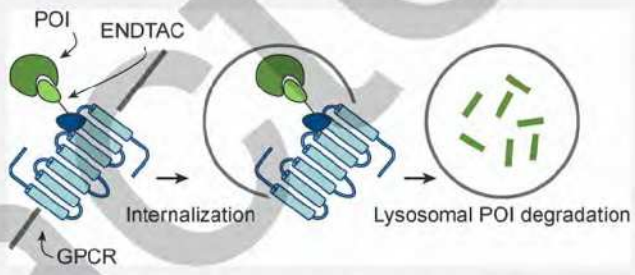

INTRODUCTION

Traditional drug development efforts are focused mainly on small molecules that target druggable protein classes such as enzymes and receptors.[1] The majority of drugs operate as inhibitors of protein function; however, because this mode of action utilizes a target occupancy paradigm requiring high drug concentrations to sustain the biological response, it also can lead to undesirable off-target effects. As an alternative, PROteolysis TArgeting Chimeras (PROTACs) hold great promise as a therapeutic modality since they require only a transient interaction with the target protein to promote its degradation.[2−4] However, despite promoting the degradation of various proteins, PROTACs are limited to target engagement within the intracellular space for ubiquitination.[5−9] PROTACs are therefore unable to act on secreted proteins, such as cytokines and chemokines, which exert their biological activity from the extracellular space.[10,11] These proteins bind to cell surface receptors and can initiate the aberrant signaling implicated in multiple diseases (Figure 1A). While monoclonal antibodies can target secreted proteins or their cognate receptors to block signaling, efforts to develop small molecule inhibitors for secreted proteins have so far been less successful.[12,13] Given the functional importance of secreted proteins in diseases and the current limitations on inhibiting their activities, alternative technologies to efficiently target them are needed.

Receptor−ligand-mediated delivery systems have gained significant attention in the past few years.[14,15] Several studies have reported that cell surface receptors such as transferrin receptor, asialoglycoprotein (ASGPr), and folate receptor can be used to selectively deliver a wide range of therapeutic agents into cancer cells via receptor-mediated endocytosis.[16−18] In addition, a recent study has shown that Cas9 could be selectively delivered into cells by harnessing the receptor−ligand interactions followed by endosomal escape.[19] Here we report a new approach to potentially target extracellular proteins for receptor-facilitated lysosomal degradation using chimeric molecules termed ENDosome TArgeting Chimeras (ENDTACs) (Figure 1B). An ENDTAC is a heterodimeric molecule consisting of a small molecule (agonist) that binds to a plasma

Received: March 5, 2019
Published: May 9, 2019

DOI: 10.1021/acscentsci.9b00224
ACS Cent. Sci. 2019, 5, 1079−1084

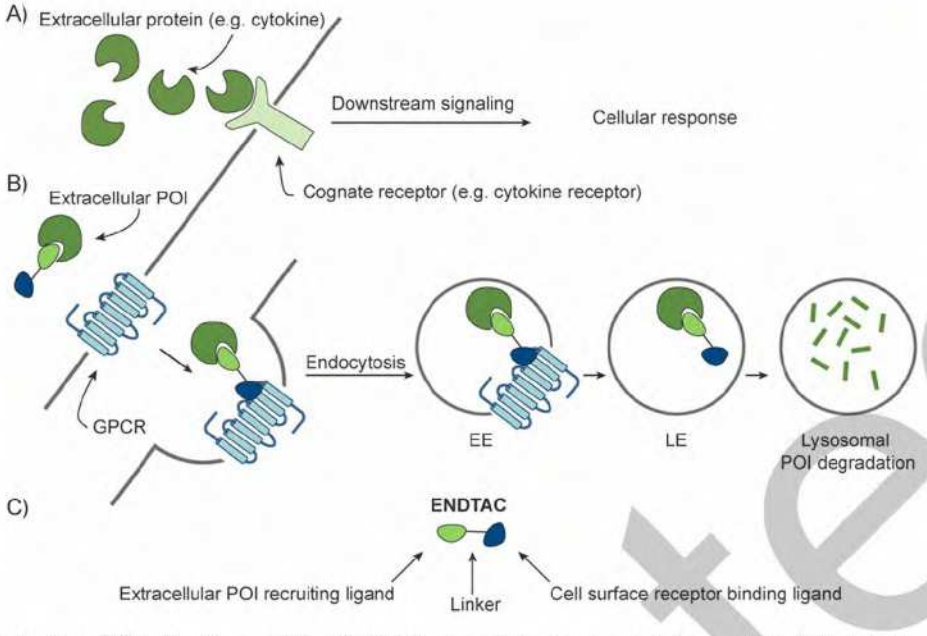

Figure 1. ENDTAC technology. (A) In the absence of the ENDTAC, extracellular target protein (e.g., cytokine) binds to its cognate receptor (e.g., cytokine receptor) and activates downstream signaling leading to a cellular response (e.g., cell proliferation, apoptosis, and/or inflammation). (B) Upon ENDTAC addition, the target extracellular protein of interest (POI) is endocytosed via a decoy GPCR, CXCR7, and subsequently degraded by the lysosome. EE = early endosome, LE = late endosome. (C) An ENDosome TArgeting Chimera (ENDTAC) is a heterodimeric molecule consisting of an agonist ligand that binds to a cell surface receptor (e.g., CXCR7) coupled to a ligand that recruits the extracellular POI (e.g., cytokine).

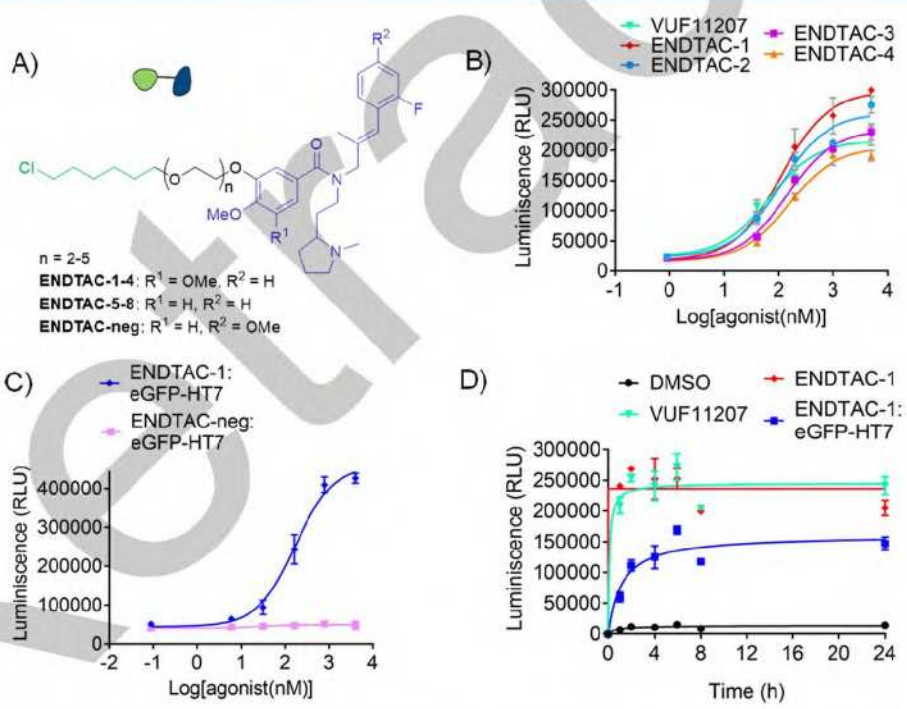

Figure 2. Characterization of ENDTACs. (A) Core structure of ENDTACs. (B) Characterization of agonist activity of **ENDTACs-1−4** using the Tango assay ($n = 4$). (C) Activity of **ENDTAC-1** and **ENDTAC-neg** after prereacting with eGFP-HT7 measured by Tango assay ($n = 2$). (D) Pulse chase Tango assay for warhead **VUF11207**, **ENDTAC-1**, and precomplexed **ENDTAC-1**:eGFP-HT7 (4 μM) ($n = 2$). Curves were fitted using GraphPad Prism 5. All data represent mean ± SEM.

membrane-localized receptor of interest (e.g., a GPCR) while the other end, connected via a linker, of the ENDTAC binds and recruits the extracellular protein of interest (POI) (e.g., a cytokine) (Figure 1C). Upon binding to the GPCR, the tethered extracellular protein can undergo receptor-mediated endocytosis and subsequently degradation by the lysosome (Figure 1B).

DOI: 10.1021/acscentsci.9b00224
ACS Cent. Sci. 2019, 5, 1079−1084

Table 1. EC_{50} Values of VUF11207 and CXCR7-Recruiting ENDTACs As Determined in the Tango Assay[a]

entry	compound ID	n	EC_{50} (nM) compound alone	EC_{50} (nM) compound + eGFP − HT7	EC_{50} (nM) compound + Nanoluc − HT7
1	**VUF11207**	N/A[b]	68 ± 1.2		
2	**ENDTAC-1**	2	113 ± 1.3	169 ± 1.5	146 ± 1.3
3	**ENDTAC-2**	3	111 ± 1.2	251 ± 1.5	
4	**ENDTAC-3**	4	145 ± 1.1	373 ± 2.0	
5	**ENDTAC-4**	5	158 ± 1.2	287 ± 3.0	
6	**VUF11403**	N/A[b]	76 ± 1.3		
7	**ENDTAC-5**	2	1360 ± 3.8	ND	
8	**ENDTAC-6**	3	2453 ± 1.1	ND	
9	**ENDTAC-7**	4	4705 ± 5.2	ND	
10	**ENDTAC-8**	5	1815 ± 1.4	ND	
11	**ENDTAC-neg**	2	ND	ND	

[a]ENDTACs (**1**−**4**) contain OMe at the R_1 position and H at the R_2 position whereas ENDTACs (**5**−**8**) contain H at both R_1 and R_2 positions. These ENDTACs are generated by adding a chloroalkane to **VUF11207** or **VUF11403** via varying linker lengths. The **ENDTAC-neg** structure is slightly different than **ENDTACs-1**−**4** where R_1 is H, and R_2 is OMe. **VUF11207** and **VUF11403** are known small molecule agonists of CXCR7. eGFP-HT7 is HA-eGFP-Halotag7 protein, and Nanoluc-HT7 is a HA-nanoluciferase-Halotag7 fusion protein. ND: not determined. All data represent mean ± SEM. [b]N/A: not applicable.

RESULTS AND DISCUSSION

To validate the feasibility of the ENDTAC approach, we performed a proof-of-concept study using the decoy receptor, CXCR7 (ACKR3), as the cell surface receptor and an engineered HA-eGFP-HaloTag7 (eGFP-HT7) fusion protein as the extracellular target protein. The GPCR CXCR7 is constitutively endocytosed at a low level to degrade its cognate chemokines via transport to the lysosome.[20] A previous report has shown that two potent small molecule agonists **VUF11207** and **VUF11403** induce CXCR7 internalization (Figure S1).[21] Since both these 3,4-dimethoxy and 3,4,5-trimethoxy styrene amides (**VUF11403** and **VUF11207**, respectively) exhibit similar agonist activity in various pairwise comparisons,[21] we incorporated the HT7-recruiting chloroalkane at their 5-position (Figure 2A). Using a facile synthetic method (Scheme S1, in the Supporting Information), linkers ranging from a diethylene glycol to pentaethylene glycol were incorporated in both series (R1: H or OMe) to afford **ENDTACs-1**−**8** (Figure 2A). Agonist activity for **ENDTACs-1**−**8** was evaluated by the Tango GPCR assay[22,23] (Table 1). Interestingly, the dimethoxy-containing ENDTAC series (**ENDTACs-1**−**4**; R_1, OMe; R_2, H) displayed only slightly reduced potency compared to the parent warhead **VUF11207** (Figure 2B; Table 1; left EC_{50} column), while the monomethoxy-containing ENDTACs (**ENDTACs-5**−**8**; R_1, H; R_2, H) exhibited greater than 10- to 40-fold reduction in activity compared to the respective warhead, **VUF11403** (Figure S1 and Table 1). Accordingly, we focused on the dimethoxy-containing ENDTAC series and measured the ability of the prereacted **ENDTAC**:eGFP-HT7 complex to activate the CXCR7 receptor. Purified eGFP-HT7 was used as the reporter POI (Figures S2 and S3) to evaluate **ENDTACs-1**−**4**. The reaction between purified eGFP-HT7 and ENDTACs was confirmed by LC-MS analysis (Figures S4 and S5 and Table S1).

Among these four ENDTACs, **ENDTAC-1** retained a similar potency compared to **VUF11207** after reacting with eGFP-HT7 (Table 1). On the basis of this initial activity profile, we selected **ENDTAC-1** for use in subsequent experiments. To ensure that eGFP-HT7 internalization is mediated via CXCR7 activity, we synthesized a negative control molecule, **ENDTAC-neg**, using a similar synthetic approach (Figure 2A; Scheme S2). The *para*-methoxy group on the styrene ring (R_1, H; and R_2, OMe) of **ENDTAC-neg** was previously identified to abrogate CXCR7 agonist activity.[21] Therefore, **ENDTAC-neg** was evaluated for activity in the absence or presence of eGFP-HT7. According to Tango assay data, prereacted **ENDTAC-neg**:eGFP-HT7 did not show any CXCR7 activation compared to **ENDTAC-1**:eGFP-HT7, supporting the use of **ENDTAC-neg** as a negative control. (Figure 2C and Figure S6). Furthermore, we also analyzed the saturation kinetics of the prereacted **ENDTAC-1**:eGFP-HT7 complex using the Tango assay. The warhead **VUF11207** and **ENDTAC-1** show fast saturation kinetics, whereas **ENDTAC-1**:eGFP-HT7 reaches saturation within 4 h (Figure 2D). Given the similar agonistic activities of the warhead and corresponding ENDTAC, as well as favorable binding kinetics, we next proceeded to study ENDTAC-induced internalization of eGFP-HT7 protein.

CXCR7-expressing MCF7 cells were treated for 4 h with either **ENDTAC-1** or **ENDTAC-neg** conjugated to purified eGFP-HT7 (10 μM), and internalization was monitored by confocal microscopy. Internalized eGFP-HT7 was visualized as GFP-positive puncta (green), and we observed a greater uptake of eGFP-HT7 in the presence of 10 μM **ENDTAC-1** after 4 h (Figure 3A). The quantitation of GFP-positive cells suggests **ENDTAC-1** induced internalization of eGFP-HT7, as compared to **ENDTAC-neg** (Figure 3B). We also analyzed eGFP-HT7 internalization by immunostaining with HA antibody and observed an overlay between the GFP and HA puncta in the presence of **ENDTAC-1** (Figure S7). eGFP-HT7 uptake was confirmed as being ENDTAC-dependent in CXCR7-expressing MCF7s and MIA PaCa-2 cells, where greater uptake is observed in the presence of 500 nM **ENDTAC-1**, compared to **ENDTAC-neg**, via immunoblotting (Figure 3C). To corroborate this finding, we used purified Nanoluc-HT7 (Figures S2 and S3) as the extracellular POI and evaluated Nanoluc-HT7 uptake by measuring luciferase activity in MCF7 and HTLA cells (Figure 3D and Figure S8). As was observed with the **ENDTAC-1**:eGFP-HT7 adduct, **ENDTAC-1** retained CXCR7 agonistic activity after reacting with Nanoluc-HT7 (Table 1). We first incubated prereacted Nanoluc-HT7 + **ENDTAC-1** (1 μM) with MCF7 cells for 2 h and then changed to ENDTAC-free media and assayed for Nanoluc-HT7 uptake over 24 h. Consistent with previous data, we observed a 2.5-fold uptake of Nanoluc-HT7 in the presence of **ENDTAC-1** compared to **ENDTAC-neg** in the first 2−6 h (Figure 3D, Figure S8). In both MCF7 and HTLA cells, there is an observed reduction in Nanoluc-HT7 activity at

DOI: 10.1021/acscentsci.9b00224
ACS Cent. Sci. 2019, 5, 1079−1084

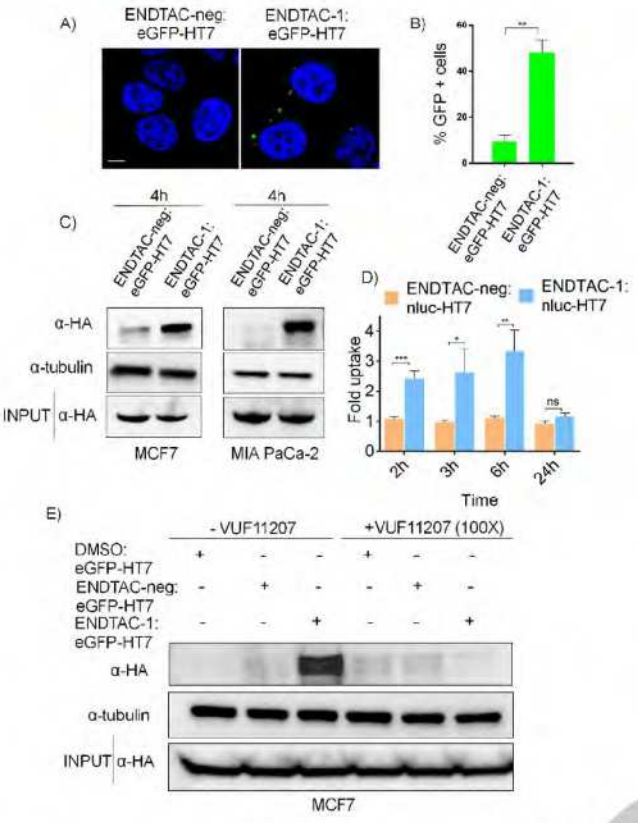

Figure 3. Internalization of eGFP-HT7 in the presence of **ENDTAC-1**. (A) Confocal microscopy analysis of internalized eGFP-HT7 (green puncta) with 10 μM **ENDTAC-1**. Nuclei are stained with Hoechst stain (blue). Scale bar: 5 μm. (B) eGFP-positive cells were quantified and presented as a percentage. Quantified data represent mean ± SEM, n = 3. *p < 0.05. (C) Cellular uptake of eGFP-HT7 in MCF7 and MIA PaCa-2 cells was analyzed by immunoblotting after incubating for 4 h with **ENDTAC-neg**:eGFP-HT7 or **ENDTAC-1**:eGFP-HT7 (500 nM). (D) Cellular uptake of Nanoluc-HT7 in MCF7 cells was analyzed by evaluating luciferase activity. The relative luminescence units of **ENDTAC-1**:Nanoluc-HT7 were normalized to **ENDTAC-neg**:Nanoluc-HT7 and presented as the fold uptake using GraphPad Prism 5 (n = 6). Data represent mean ± SEM; *p < 0.05; ns, not significant. (E) Cellular uptake of eGFP-HT7 in MCF7 cells was analyzed by immunoblotting after incubating for 4 h with DMSO:eGFP-HT7, **ENDTAC-neg**:eGFP-HT7, or **ENDTAC-1**:eGFP-HT7 (250 nM) in the absence or presence of excess warhead, **VUF11207** (25 μM).

24 h, suggesting that internalized protein has been degraded in the lysosome.

Given the possibility that bulk endocytosis could lead to nonspecific uptake of proteins, we performed a ligand competition assay with excess CXCR7 agonist **VUF11207** to probe that the **ENDTAC-1**-mediated HT7 uptake is CXCR7-dependent. We incubated MCF7 cells with DMSO:eGFP-HT7, **ENDTAC-neg**:eGFP-HT7, and **ENDTAC-1**:eGFP-HT7 in the absence or presence of excess warhead (**VUF11207**). The **ENDTAC-1**-mediated HT7 uptake was completely inhibited in the presence of the excess warhead (Figure 3E), suggesting that the ternary complex formation between eGFP-HT7, **ENDTAC-1**, and CXCR7 is required to facilitate selective internalization of eGFP-HT7.

We next sought to determine whether the level of CXCR7 expression could play a key role in efficiency of the ENDTAC system. To probe the hypothesis, we first compared the uptake of eGFP-HT7 in CXCR7-overexpressing 293T cells. Upon incubation of **ENDTAC-1**:eGFP-HT7 with 293T cells, we observed an **ENDTAC-1**-dependent uptake of eGFP-HT7 compared to nontransfected cells (Figure S9A), suggesting that increased expression of CXCR7 enhances the **ENDTAC-1**-mediated internalization of HT7. To further support this result, we compared the **ENDTAC-1**-dependent cellular uptake in MDA-MB-231 cells (CXCR7-negative) and MCF7 cells (CXCR7-positive). Compared to MDA-MB-231 cells, we observed an increased eGFP-HT7 uptake in **ENDTAC-1** treated MCF7 cells (Figure S9B), suggesting that the level of CXCR7 surface expression is a key parameter that dictates ENDTAC efficiency.

Upon receptor-mediated endocytosis, we propose that the eGFP-HT7 protein traffics sequentially to the early endosome and the late endosome and subsequently is degraded in the lysosome. To evaluate this hypothesis, we treated MCF7 and MIA PaCa-2 cells with **ENDTAC-1**:eGFP-HT7 or **ENDTAC-neg**:eGFP-HT7 for 4 h, washed the cells, replaced the medium with fresh medium, and cultured the cells for another 3 h, to monitor the fate of internalized eGFP-HT7. We observed eGFP-HT7 uptake by the cells after a continuous 4 h **ENDTAC-1**:eGFP-HT7 incubation, followed by the disappearance of eGFP-HT7 after a 3 h chase (Figure 4A,B). Therefore, it is possible that internalized eGFP-HT7 protein traffics to the lysosome and is therein degraded, given the mechanism of CXCR7 internalization following agonist treatment.[20] To evaluate if lysosomal-mediated eGFP-HT7 degradation occurs, we incubated cells with **ENDTAC-neg**:eGFP-HT7 or **ENDTAC-1**:eGFP-HT7 for 4 h, washed the cells, and cultured them in the absence or presence of the lysosome inhibitor, bafilomycin A1 (bafA1). Interestingly, eGFP-HT7 is degraded only in the absence of bafA1, suggesting that eGFP-HT7 degradation indeed occurs via the lysosomal pathway (Figure 4C,D).

To further confirm endolysosomal accumulation of eGFP-HT7 in the presence of ENDTAC, we examined the uptake and degradation of eGFP-HT7 in MCF7 cells by confocal microscopy. MCF7 cells were treated with either Alexa Fluor 488-conjugated transferrin (TFN488), a positive control for endocytosis,[24] or the **ENDTAC-1**/**ENDTAC-neg**:eGFP-HT7 conjugate (10 μM) for 4 h, fixed, and analyzed by confocal microscopy. Interestingly, as similarly observed with TFN488 treatment, eGFP-HT7-positive cells were observed in the presence of **ENDTAC-1**:eGFP-HT7 (Figure 5A–C). These eGFP-HT7 foci colocalize with the early endosome marker (EEA1) suggesting that internalized eGFP-HT7 traffics to the endosome (Figure 5, panel C). Furthermore, we also observed that eGFP-HT7-positive foci partially colocalize with the lysosome marker (LysoTracker), suggesting that **ENDTAC-1** promotes receptor-mediated uptake and lysosomal degradation of eGFP-HT7 protein (Figure 5D,E).

While PROTACs are widely used in the field to target many intracellular proteins,[9] a key limitation is their inability to target extracellular proteins. Here we show for the first time that chimeric molecules, which we designate as "ENDTACs", are capable of recruiting an extracellular protein (eGFP-HT7), for internalization and lysosomal degradation by hijacking a GPCR-mediated endocytosis pathway. Although we present a proof-of-concept approach using a covalent HaloTag-based system, we anticipate that the ENDTAC technology could be further optimized and modified for a noncovalent setting. In summary, the ENDTAC technology represents a new chemical biology

DOI: 10.1021/acscentsci.9b00224
ACS Cent. Sci. 2019, 5, 1079−1084

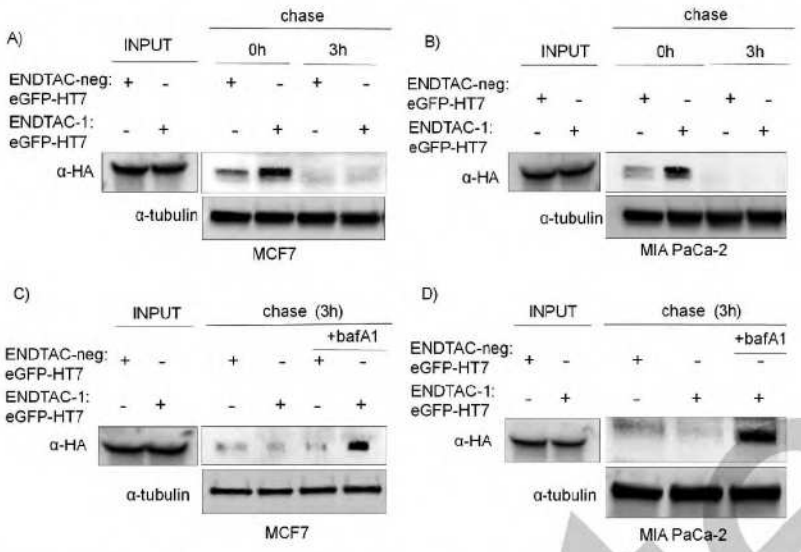

Figure 4. Cellular uptake and lysosomal degradation of eGFP-HT7 in the presence of **ENDTAC-1**. (A) Immunoblot analysis of uptake and fate of internalized eGFP-HT7 after 4 h of incubation followed by a 3 h chase in **ENDTAC-neg**/**ENDTAC-1**:eGFP-HT7-free medium in MCF7 ($n = 4$) and (B) MIA PaCa-2 cells ($n = 3$). (C) MCF7 or (D) MIA PaCa-2 cells were incubated with **ENDTAC-neg**/**ENDTAC-1**:eGFP-HT7 (500 nM) for 4 h, released to ENDTAC-free medium, and chased for an additional 3 h in the absence or presence of bafilomycin A1 (bafA1) (100 nM) ($n = 3$).

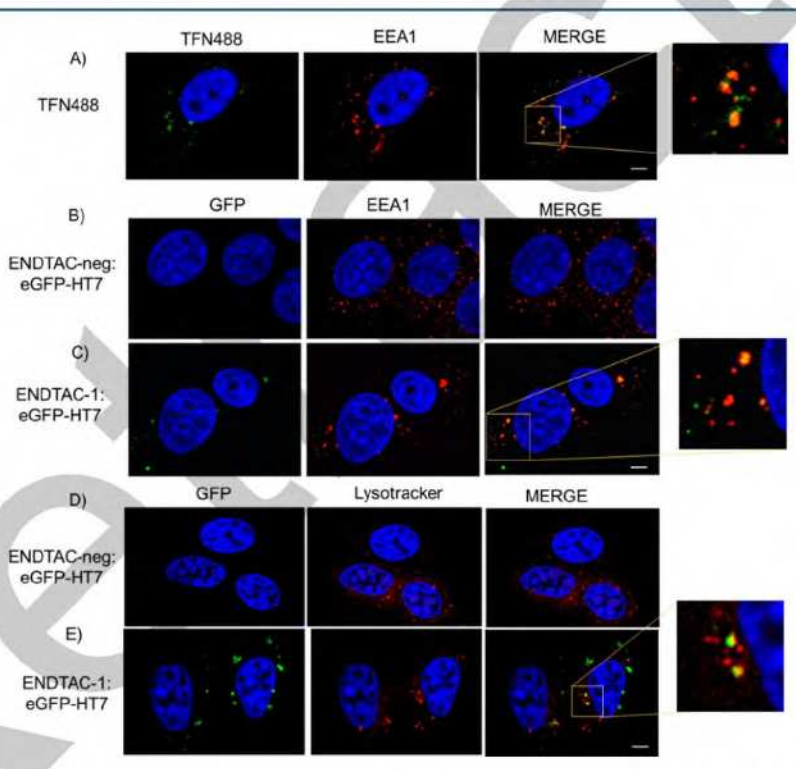

Figure 5. Endolysosomal trafficking of eGFP-HT7 in the presence of **ENDTAC-1**. Confocal microscopy analysis of (A) AF488-conjugated transferrin (TFN488) was used as a positive control for endocytosis. (B–E) Trafficking of internalized eGFP-HT7 (10 μM) to the endolysosome compartment after 4 h. (B, C) EEA1, early endosome marker, and (D, E) LysoTracker, lysosome marker. Red, EEA1 and LysoTracker; green, eGFP-HT7; yellow, merged images; blue, Hoechst stain for nuclei. Scale bar: 5 μm.

tool to study extracellular proteins and has the potential for depleting disease-causing extracellular proteins in the future.

■ ASSOCIATED CONTENT

Supporting Information

The Supporting Information is available free of charge on the ACS Publications website at DOI: 10.1021/acscentsci.9b00224.

Experimental procedures and synthesis and characterization of ENDTACs (PDF)

■ AUTHOR INFORMATION

Corresponding Author

*E-mail: craig.crews@yale.edu.

DOI: 10.1021/acscentsci.9b00224
ACS Cent. Sci. 2019, 5, 1079−1084

ORCID
Craig M. Crews: 0000-0002-8456-2005

Notes

The authors declare the following competing financial interest(s): C.M.C. is a consultant to and shareholder in Arvinas, which partially supports research in his lab.

■ ACKNOWLEDGMENTS

This work was supported by the NIH (R35 CA197589). M.P. gratefully acknowledges the Swedish Research Council (Vetenskapsrådet) for international postdoctoral funding (2016-00294). HTLA (a HEK293 cell line stably expressing a tTA-dependent luciferase reporter and a β-arrestin2-TEV fusion gene) cells were generously provided by Gilad Barnea (Brown University, RI). We thank the Alanna Schepartz lab for their technical help and John Hines for reviewing the manuscript.

■ REFERENCES

(1) Hopkins, A. L.; Groom, C. R. The druggable genome. *Nat. Rev. Drug Discovery* **2002**, *1* (9), 727−730.
(2) Sakamoto, K. M.; Kim, K. B.; Kumagai, A.; Mercurio, F.; Crews, C. M.; Deshaies, R. J. Protacs: chimeric molecules that target proteins to the Skp1-Cullin-F box complex for ubiquitination and degradation. *Proc. Natl. Acad. Sci. U. S. A.* **2001**, *98* (15), 8554−8559.
(3) Sakamoto, K. M.; Kim, K. B.; Verma, R.; Ransick, A.; Stein, B.; Crews, C. M.; Deshaies, R. J. Development of Protacs to target cancer-promoting proteins for ubiquitination and degradation. *Mol. Cell. Proteomics* **2003**, *2* (12), 1350−1358.
(4) Schneekloth, J. S., Jr.; Fonseca, F. N.; Koldobskiy, M.; Mandal, A.; Deshaies, R.; Sakamoto, K.; Crews, C. M. Chemical genetic control of protein levels: selective in vivo targeted degradation. *J. Am. Chem. Soc.* **2004**, *126* (12), 3748−3754.
(5) Burslem, G. M.; Smith, B. E.; Lai, A. C.; Jaime-Figueroa, S.; McQuaid, D. C.; Bondeson, D. P.; Toure, M.; Dong, H.; Qian, Y.; Wang, J.; Crew, A. P.; Hines, J.; Crews, C. M. The advantages of targeted protein degradation over inhibition: An RTK case study. *Cell Chem. Biol.* **2018**, *25* (1), 67−77.
(6) Lai, A. C.; Toure, M.; Hellerschmied, D.; Salami, J.; Jaime-Figueroa, S.; Ko, E.; Hines, J.; Crews, C. M. Modular PROTAC design for the degradation of oncogenic BCR-ABL. *Angew. Chem., Int. Ed.* **2016**, *55* (2), 807−810.
(7) Lu, J.; Qian, Y.; Altieri, M.; Dong, H.; Wang, J.; Raina, K.; Hines, J.; Winkler, J. D.; Crew, A. P.; Coleman, K.; Crews, C. M. Hijacking the E3 ubiquitin ligase cereblon to efficiently target BRD4. *Chem. Biol.* **2015**, *22* (6), 755−763.
(8) Bondeson, D. P.; Crews, C. M. Targeted Protein Degradation by Small Molecules. *Annu. Rev. Pharmacol. Toxicol.* **2017**, *57*, 107−123.
(9) Cromm, P. M.; Crews, C. M. Targeted Protein Degradation: from Chemical Biology to Drug Discovery. *Cell Chem. Biol.* **2017**, *24* (9), 1181−1190.
(10) Davoine, F.; Lacy, P. Eosinophil cytokines, chemokines, and growth factors: emerging roles in immunity. *Front. Immunol.* **2014**, *5*, 570.
(11) Majka, M.; Janowska-Wieczorek, A.; Ratajczak, J.; Ehrenman, K.; Pietrzkowski, Z.; Kowalska, M. A.; Gewirtz, A. M.; Emerson, S. G.; Ratajczak, M. Z. Numerous growth factors, cytokines, and chemokines are secreted by human CD34(+) cells, myeloblasts, erythroblasts, and megakaryoblasts and regulate normal hematopoiesis in an autocrine/paracrine manner. *Blood* **2001**, *97* (10), 3075−3085.
(12) Patel, D.; Lahiji, A.; Patel, S.; Franklin, M.; Jimenez, X.; Hicklin, D. J.; Kang, X. Monoclonal antibody cetuximab binds to and down-regulates constitutively activated epidermal growth factor receptor vIII on the cell surface. *Anticancer Res.* **2007**, *27* (5A), 3355−3366.
(13) Tiseo, M.; Bartolotti, M.; Gelsomino, F.; Bordi, P. Emerging role of gefitinib in the treatment of non-small-cell lung cancer (NSCLC). *Drug Des., Dev. Ther.* **2010**, *4*, 81−98.
(14) Wang, S.; Meng, Y.; Li, C.; Qian, M.; Huang, R. Receptor-mediated drug delivery systems targeting to glioma. *Nanomaterials* **2016**, *6* (1), 3.
(15) Galliford, C. V.; Low, P. S. Receptor-mediated drug delivery. In *Drug Delivery: Principles and Applications*, 2nd ed.; John Wiley & Sons, Inc., 2016; pp 451−474.
(16) Low, P. S.; Henne, W. A.; Doorneweerd, D. D. Discovery and development of folic-acid-based receptor targeting for imaging and therapy of cancer and inflammatory diseases. *Acc. Chem. Res.* **2008**, *41* (1), 120−129.
(17) Monestier, M.; Charbonnier, P.; Gateau, C.; Cuillel, M.; Robert, F.; Lebrun, C.; Mintz, E.; Renaudet, O.; Delangle, P. ASGPR-mediated uptake of multivalent glycoconjugates for drug delivery in hepatocytes. *ChemBioChem* **2016**, *17* (7), 590−594.
(18) Singh, M. Transferrin As A targeting ligand for liposomes and anticancer drugs. *Current pharmaceutical design* **1999**, *5* (6), 443−451.
(19) Rouet, R.; Thuma, B. A.; Roy, M. D.; Lintner, N. G.; Rubitski, D. M.; Finley, J. E.; Wisniewska, H. M.; Mendonsa, R.; Hirsh, A.; de Onate, L.; Compte Barron, J.; McLellan, T. J.; Bellenger, J.; Feng, X.; Varghese, A.; Chrunyk, B. A.; Borzilleri, K.; Hesp, K. D.; Zhou, K.; Ma, N.; Tu, M.; Dullea, R.; McClure, K. F.; Wilson, R. C.; Liras, S.; Mascitti, V.; Doudna, J. A. Receptor-mediated delivery of CRISPR-Cas9 endonuclease for cell-type-specific gene editing. *J. Am. Chem. Soc.* **2018**, *140* (21), 6596−6603.
(20) Luker, K. E.; Steele, J. M.; Mihalko, L. A.; Ray, P.; Luker, G. D. Constitutive and chemokine-dependent internalization and recycling of CXCR7 in breast cancer cells to degrade chemokine ligands. *Oncogene* **2010**, *29* (32), 4599−4610.
(21) Wijtmans, M.; Maussang, D.; Sirci, F.; Scholten, D. J.; Canals, M.; Mujic-Delic, A.; Chong, M.; Chatalic, K. L.; Custers, H.; Janssen, E.; de Graaf, C.; Smit, M. J.; de Esch, I. J.; Leurs, R. Synthesis, modeling and functional activity of substituted styrene-amides as small-molecule CXCR7 agonists. *Eur. J. Med. Chem.* **2012**, *51*, 184−192.
(22) Kroeze, W. K.; Sassano, M. F.; Huang, X. P.; Lansu, K.; McCorvy, J. D.; Giguere, P. M.; Sciaky, N.; Roth, B. L. PRESTO-Tango as an open-source resource for interrogation of the druggable human GPCRome. *Nat. Struct. Mol. Biol.* **2015**, *22* (5), 362−369.
(23) Barnea, G.; Strapps, W.; Herrada, G.; Berman, Y.; Ong, J.; Kloss, B.; Axel, R.; Lee, K. J. The genetic design of signaling cascades to record receptor activation. *Proc. Natl. Acad. Sci. U. S. A.* **2008**, *105* (1), 64−69.
(24) Cao, H.; Schroeder, B.; Chen, J.; Schott, M. B.; McNiven, M. A. The endocytic fate of the transferrin receptor is regulated by c-Abl kinase. *J. Biol. Chem.* **2016**, *291* (32), 16424−16437.

DOI: 10.1021/acscentsci.9b00224
ACS Cent. Sci. 2019, 5, 1079−1084

EXHIBIT 11

nature chemical biology

ARTICLES

https://doi.org/10.1038/s41589-021-00770-1

Check for updates

LYTACs that engage the asialoglycoprotein receptor for targeted protein degradation

Green Ahn[1], Steven M. Banik[1], Caitlyn L. Miller[2], Nicholas M. Riley[1], Jennifer R. Cochran[2] and Carolyn R. Bertozzi[1,3]✉

Selective protein degradation platforms have afforded new development opportunities for therapeutics and tools for biological inquiry. The first lysosome-targeting chimeras (LYTACs) targeted extracellular and membrane proteins for degradation by bridging a target protein to the cation-independent mannose-6-phosphate receptor (CI-M6PR). Here, we developed LYTACs that engage the asialoglycoprotein receptor (ASGPR), a liver-specific lysosome-targeting receptor, to degrade extracellular proteins in a cell-type-specific manner. We conjugated binders to a triantenerrary *N*-acetylgalactosamine (tri-GalNAc) motif that engages ASGPR to drive the downregulation of proteins. Degradation of epidermal growth factor receptor (EGFR) by GalNAc-LYTAC attenuated EGFR signaling compared to inhibition with an antibody. Furthermore, we demonstrated that a LYTAC consisting of a 3.4-kDa peptide binder linked to a tri-GalNAc ligand degrades integrins and reduces cancer cell proliferation. Degradation with a single tri-GalNAc ligand prompted site-specific conjugation on antibody scaffolds, which improved the pharmacokinetic profile of GalNAc-LYTACs in vivo. GalNAc-LYTACs thus represent an avenue for cell-type-restricted protein degradation.

Targeted protein degradation (TPD) is a promising new therapeutic modality and a tool for probing biological pathways as well as the cellular degradation machinery. Most TPD platforms, such as immunomodulatory imide drugs (IMiDs)[1,2], proteolysis-targeting chimeras (PROTACs)[3,4], degradation tags (dTAGs)[5,6], Trim-Away[7] and specific and non-genetic inhibitor of apoptosis protein-dependent protein erasers (SNIPERs)[8], rely on the ubiquitin proteasome system (UPS). Recently, autophagy targeting chimeras (AUTACs)[9] and autophagosome-tethering compounds (ATTECs)[10,11] have emerged as approaches that exploit the intracellular autophagy machinery for mediating TPD. Advances in TPD strategies have accelerated over the past two decades, and PROTACs have recently entered clinical trials[12]. However, the cytosolic localization of the UPS and targetable autophagy machinery restricts these approaches to proteins with cytosolic domains and requires degraders to be cell permeable. To relax these constraints and expand the scope of TPD to extracellular targets, we have developed LYTACs, which bind and direct plasma membrane-associated or secreted proteins to lysosomes[13]. First-generation LYTACs used the CI-M6PR that endogenously traffics hydrolases and other cargo to the lysosome (Fig. 1a)[14]. LYTACs were composed of a target-binding moiety (for example, an antibody or small molecule) linked to a CI-M6PR-binding ligand, mannose-6-phosphonate (M6Pn). These M6Pn-LYTACs promoted lysosomal degradation of disease-relevant extracellular and membrane proteins by bridging the target protein with CI-M6PR.

CI-M6PR is one of several lysosome-trafficking receptors that could, in principle, be harnessed for the design of LYTACs. Indeed, whereas CI-M6PR is broadly expressed in most tissues, other lysosome-trafficking receptors have tissue-specific expression patterns. Such receptors offer the opportunity to achieve tissue-specific LYTAC activity. For therapeutic development, the ability to select in which tissue degradation occurs could have benefits for the therapeutic window.

Here, we developed LYTACs that engage the liver-specific ASGPR[15] as a lysosome-targeting receptor (Fig. 1b). ASGPR recognizes glycoproteins bearing GalNAc or galactose (Gal) ligands and internalizes them via clathrin-mediated endocytosis[16,17]. Following internalization and endosomal acidification, ASGPR releases GalNAc or Gal and recycles back to the plasma membrane, while glycoproteins proceed to the lysosome[18]. ASGPR has been exploited to achieve efficient delivery of various cargo to the liver, most notably short interfering RNA (siRNA) and antisense oligonucleotide (ASO) therapeutics[15,19–22]. We developed LYTACs consisting of an antibody against a target of interest conjugated to homogeneous GalNAc ligands that induce targeted, cell-type-specific degradation. In doing so, we demonstrated that receptor-mediated degradation is generalizable beyond CI-M6PR. Additionally, we showed that a synthetic 3.4-kDa peptide, a much smaller binder than an antibody, can be linked to a single tri-GalNAc ligand to degrade integrins, resulting in antiproliferative effects in hepatocellular carcinoma (HCC) cells. We then simplified the structural architecture of antibody-based GalNAc-LYTACs through site-specific conjugation, which enabled modulation of the pharmacokinetic profile of GalNAc-LYTACs.

Results

Construction and internalization of GalNAc-LYTACs. Previous work on siRNA therapeutics revealed that tri-GalNAc ligands engage ASGPR with low nanomolar affinity[23–25] and showed promising efficacy and safety profiles[26,27]. The homogeneous nature of a tri-GalNAc ligand was additionally appealing as it would enable precise characterization of ligand to antibody ratios, which was challenging with the heterogenous polymers utilized in the initial M6Pn-LYTACs[13]. Therefore, we synthesized tri-GalNAc-DBCO (1) in eight steps from peracetylated GalNAc and a carboxybenzyl (Cbz)-protected dendrimer scaffold[21,28] (Fig. 1c and Supplementary Note 1). Tri-GalNAc-DBCO

[1]Department of Chemistry and Stanford ChEM-H, Stanford University, Stanford, CA, USA. [2]Department of Bioengineering, Stanford University, Stanford, CA, USA. [3]Howard Hughes Medical Institute, Stanford, CA, USA. ✉e-mail: bertozzi@stanford.edu

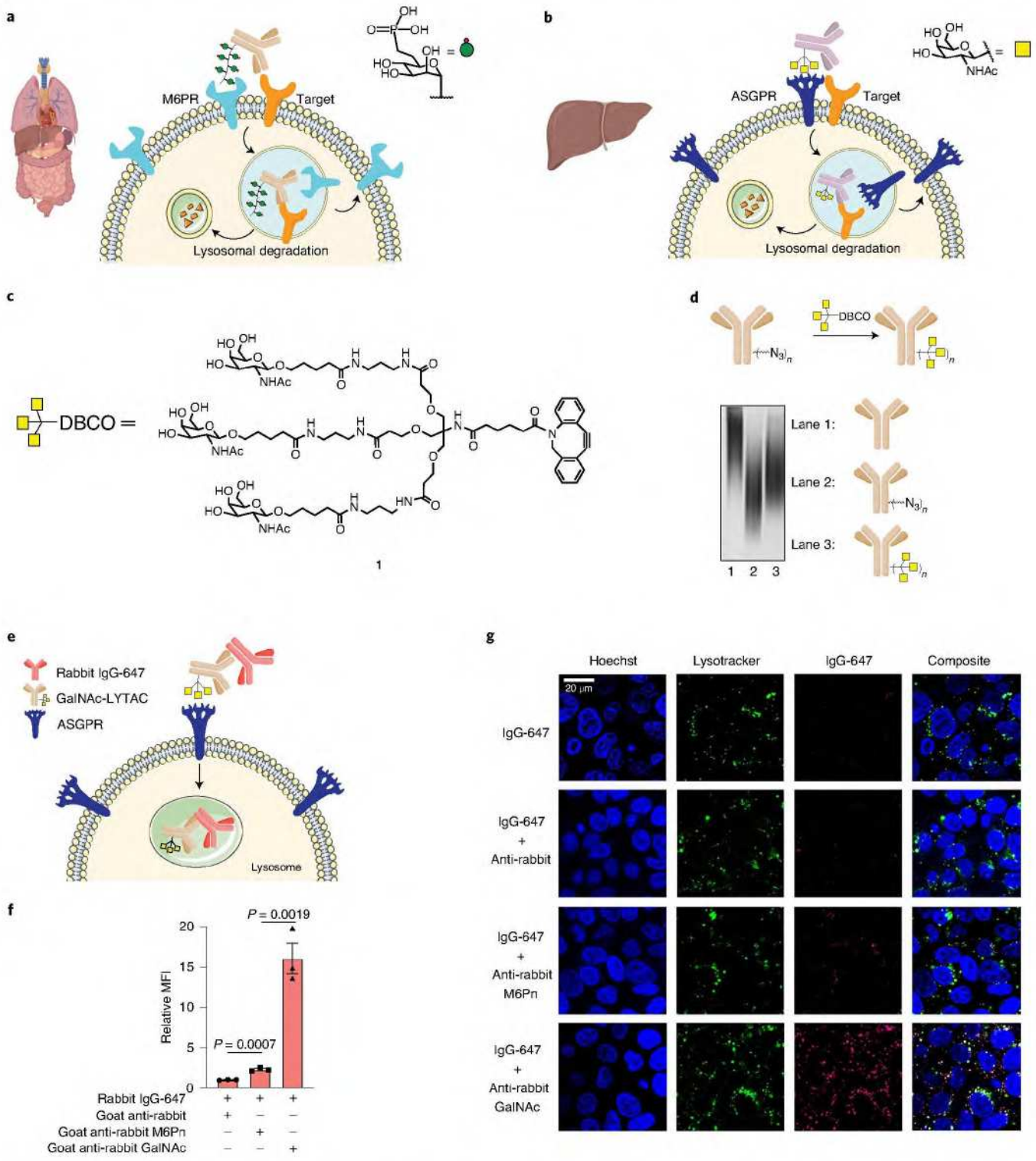

Fig. 1 | LYTACs can hijack the ASPGR for targeted and cell-specific protein degradation. a, First-generation LYTACs co-opt the broadly expressed CI-M6PR. **b**, GalNAc-LYTACs hijack the liver-specific ASGPR to target hepatocytes. **c**, Structure of the tri-GalNAc-DBCO (**1**) ligand for ASGPR targeting. **d**, Synthesis of antibody-tri-GalNAc conjugates (GalNAc-LYTACs). Native gel electrophoresis of IgG, IgG-N_3 and IgG-GalNAc. **e**, LYTAC-mediated internalization of rabbit IgG-647 in HEPG2 cells. **f**, Mean fluorescence intensity (MFI) relative to the control (rabbit IgG-647 only) for HEPG2 cells incubated at 37 °C for 1 h with 50 nM rabbit IgG-647 and 25 nM goat anti-rabbit, goat anti-rabbit M6Pn or goat anti-rabbit GalNAc. MFI was determined by live-cell flow cytometry. **g**, Live-cell imaging of HEPG2 cells that were incubated at 37 °C for 1 h with 50 nM rabbit IgG-647 and 25 nM goat anti-rabbit, goat anti-rabbit M6Pn or goat anti-rabbit GalNAc. Scale bar, 20 μm. Gels (**d**) and images (**g**) are representative of two independent experiments. Data in **f** are represented as the mean of three independent experiments ± s.e.m. *P* values were determined by unpaired two-tailed *t*-tests.

was conjugated to azides on non-specifically labeled antibodies via Cu-free strain-promoted azide–alkyne cycloaddition (Supplementary Fig. 1). The conjugation reaction was monitored by native gel electrophoresis, as the GalNAc-conjugated antibody migrates slower than the azide-functionalized starting material as a result of increased hydrodynamic size (Fig. 1d). To confirm that antibody-GalNAc conjugates can trigger internalization of extracellular targets via ASGPR, we examined LYTAC-mediated uptake in an HCC cell line, HEPG2. We included the first-generation LYTAC (M6Pn-LYTAC)[13] that engages the CI-M6PR as a comparison. HEPG2 cells were incubated with rabbit IgG-647 and goat anti-rabbit (control), goat anti-rabbit M6Pn (M6Pn-LYTAC) or goat anti-rabbit GalNAc (GalNAc-LYTAC) for 1 h, and intracellular fluorescence was analyzed by flow cytometry (Fig. 1e). M6Pn-LYTAC increased cellular fluorescence 2-fold relative to the control, while GalNAc-LYTAC increased cellular fluorescence 16-fold relative to the control (Fig. 1f). This result was confirmed by confocal microscopy, where GalNAc-LYTAC treatment resulted in high IgG-647 signal that colocalized with Lysotracker, indicating that GalNAc-LYTACs traffic to acidic compartments in cells (Fig. 1g). The superior internalizing efficiency of GalNAc-LYTAC compared to M6Pn-LYTAC is potentially due to the higher surface expression of ASGPR than CI-M6PR in hepatocytes (Supplementary Fig. 2).

Degradation of EGFR via GalNAc-LYTAC. We next asked if GalNAc-LYTACs could mediate the degradation of membrane proteins in HCC cell lines. We chose EGFR as a target as it is overexpressed in individuals with HCC and its dysregulated activity has been implicated in primary resistance to sorafenib, the standard of care for advanced HCC[29,30]. Moreover, as EGFR was previously targeted with our first-generation M6Pn-LYTACs, we sought to compare GalNAc-LYTACs to earlier congeners. Cetuximab (Ctx) is an FDA-approved blocking antibody against EGFR for colorectal cancer and head and neck cancer[31,32]. We conjugated Ctx to the tri-GalNAc ligand (Fig. 2a), and MALDI–MS analysis of the product (Ctx-GalNAc) revealed an average of 10.5 tri-GalNAc moieties per antibody (Supplementary Fig. 3). We treated HEP3B cells with Ctx-GalNAc and measured surface levels of EGFR by flow cytometry using an orthogonal detection antibody. Ctx-GalNAc degraded >70% of cell surface EGFR in HEP3B cells, a level similar to the M6Pn-LYTACs (Fig. 2b).

We then evaluated the depletion of total EGFR in HEP3B, HEPG2 and HUH7 HCC cell lines. We observed >70% total degradation with Ctx-GalNAc in HEP3B cells, consistent with the observations from cell surface degradation. HEPG2 and HUH7 cells also exhibited comparable degradation efficiency (Fig. 2c). Degradation was found to be dependent on concentration, as Ctx-GalNAc mediated 50% degradation of cell surface EGFR in HEP3B cells at a concentration as low as 1 nM. Maximum degradation was reached at a concentration of 10 nM, and this degree of degradation persisted at higher concentrations, indicating that these LYTACs do not display a notable 'hook effect' within this concentration regimen, a characteristic of other bifunctional molecules[33] (Fig. 2d and Supplementary Fig. 4). Ctx-GalNAc mediated the degradation of cell surface EGFR over 48 h, reaching >50% degradation at 24 h (Fig. 2e and Supplementary Fig. 5). Visualization and quantification of EGFR by confocal microscopy following LYTAC treatment showed diminished membrane EGFR signals, consistent with the observations from flow cytometry and western blot (Fig. 2f and Supplementary Fig. 6). Through several measurements, we showed that GalNAc-LYTACs perform comparably to M6Pn-LYTACs, demonstrating the potential generality of the lysosome-targeting receptor-mediated degradation mechanism and extending the internalizing ligand set to scalable, homogeneous structures.

Mechanism of ASGPR-mediated degradation. To confirm that depletion of EGFR by Ctx-GalNAc was dependent on ASGPR, HEP3B cells were treated with siRNA targeting ASGPR. Degradation via Ctx-GalNAc LYTAC was completely abolished following ASGPR knockdown, while EGFR degradation proceeded in cells transfected with non-targeting siRNA. Furthermore, Ctx-GalNAc treatment did not alter ASGPR levels in these cells (Fig. 3a and Supplementary Fig. 7). Co-incubation with excess exogeneous tri-GalNAc (**10**) (Supplementary Fig. 8) also inhibited degradation by Ctx-GalNAc (Fig. 3b), indicating a dependency on GalNAc binding. Treatment with bafilomycin A1 or chloroquine ablated EGFR degradation mediated by Ctx-GalNAc, confirming that the degradation mechanism promoted by GalNAc-LYTACs depends on a functional endocytic pathway (Fig. 3c).

Functional effect following LYTAC-mediated degradation. Next, we sought to determine whether degradation of EGFR would impact downstream kinase signaling compared to treatment with Ctx alone. Following LYTAC treatment, HEP3B cells were stimulated with 100 ng ml^{-1} or 50 ng ml^{-1} of EGF for 1 h to activate downstream kinase phosphorylation. After EGF stimulation, the levels of phosphorylated EGFR (pEGFR), Akt (pAkt) and MAPK (pERK1/2) were reduced following Ctx-GalNAc or Ctx-M6Pn treatment compared to Ctx treatment alone. Stimulation with lower concentrations of EGF resulted in greater relative reductions in pEGFR, pAkt and pERK1/2 in cells treated with either Ctx conjugate than in cells treated with Ctx alone (Fig. 3d). These results highlight that LYTAC-driven degradation can exert more profound effects on downstream signaling than blocking of EGFR by Ctx alone.

GalNAc-LYTAC enables cell-specific degradation. The exclusive expression of ASGPR on hepatocytes should enable the selective degradation of membrane proteins on liver cells. To test this hypothesis, we cocultured HEP3B cells (ASGPR$^+$, EGFR$^+$, M6PR$^+$) and HeLa–GFP cells (ASGPR$^-$, EGFR$^+$, M6PR$^+$), treated the coculture with Ctx conjugates and analyzed EGFR degradation in each cell type by flow cytometry (Fig. 4a). Ctx-GalNAc selectively ablated cell surface EGFR from HEP3B cells, while HeLa–GFP cells maintained high EGFR expression. The small reduction of EGFR in HeLa–GFP cells resulted from covalent modification of the antibody and was independent of the ASGPR pathway and GalNAc binding (Supplementary Fig. 9). By contrast, Ctx-M6Pn degraded EGFR in both cell types, as CI-M6PR is expressed in both HEP3B and HeLa–GFP cells (Fig. 4b,c). These data support the hypothesis that harnessing a recycling receptor with restricted expression enables LYTACs to degrade proteins in a cell-specific manner.

GalNAc-LYTACs can target HER2. To examine the ability of ASGPR-directed LYTACs to degrade additional membrane targets, we developed a GalNAc-LYTAC targeting HER2. HER2 may regulate tumor progression in individuals with early stage HCC by inducing epithelial–mesenchymal transition and can be upregulated in HCC[34]. Briefly, pertuzumab (Ptz), an approved HER2 antibody for HER2-positive breast cancer, was conjugated to the tri-GalNAc ligand, and MALDI–MS analysis confirmed that Ptz had been labeled with 11 tri-GalNAc moieties (Ptz-GalNAc) (Supplementary Fig. 10). Ptz-GalNAc reduced 75% of total HER2 in HEPG2 cells, while Ptz alone degraded only 30% (Fig. 5a). Degradation by Ptz-GalNAc was ablated by co-incubation of excess exogenous tri-GalNAc (**10**) (Extended Data Fig. 1). Visualization by confocal microscopy revealed a stark reduction and relocalization of HER2 signal in HEPG2 cells treated with Ptz-GalNAc compared to cells treated with unmodified Ptz (Fig. 5b). Strikingly, 2-h treatment with Ptz-GalNAc resulted in a punctate localization pattern of HER2 by confocal microscopy (Extended Data Fig. 2a). These puncta did not colocalize with early endosome antigen 1 (EEA1),

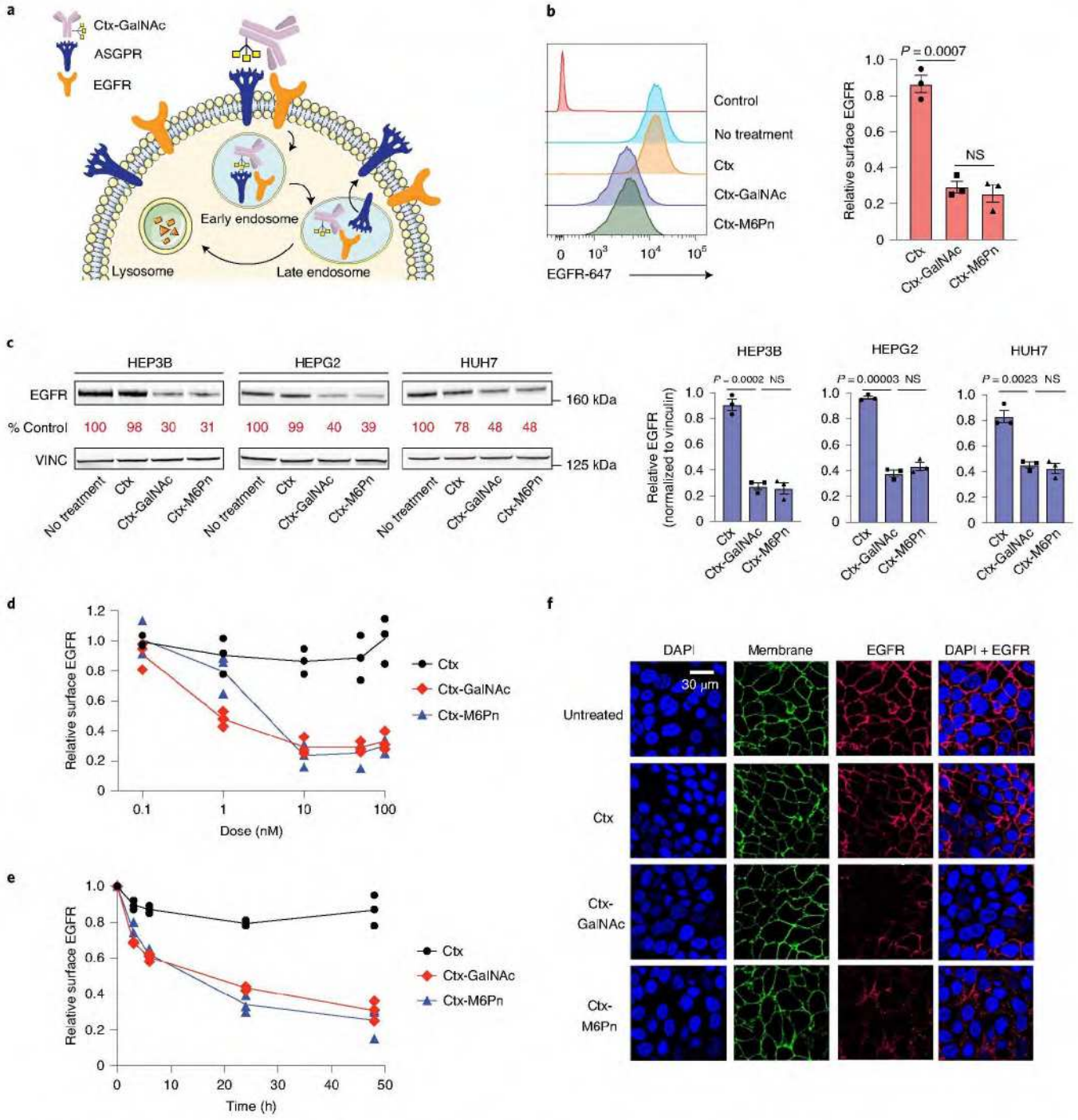

Fig. 2 | GalNAc-LYTACs promote degradation of EGFR in HCC cell lines. a, EGFR degradation mediated by Ctx-GalNAc. **b**, Degradation of cell surface EGFR in HEP3B cells as determined by live-cell flow cytometry following 48 h of treatment with 10 nM Ctx or Ctx conjugates. **c**, Western blot analysis of total EGFR levels in HEP3B, HEPG2 and HUH7 cells after treatment with 10 nM Ctx or Ctx conjugates for 48 h. **d**, Dose–response curve for cell surface EGFR degradation in HEP3B cells incubated with 0.1 nM, 1 nM, 10 nM, 50 nM or 100 nM Ctx or Ctx conjugates for 48 h. Relative surface expression of EGFR was determined by live-cell flow cytometry. **e**, Time course of degradation of cell surface EGFR in HEP3B cells incubated with 10 nM Ctx or Ctx conjugates for 3, 6, 24 and 48 h. Relative surface expression of EGFR was determined by live-cell flow cytometry. **f**, Visualization of EGFR degradation in HEP3B cells by confocal microscopy after treatment with 10 nM Ctx or Ctx conjugates for 48 h. For **b**–**e**, data represent three independent experiments, and data are shown as mean ± s.e.m. for **b**,**c**. Images in **f** are representative of two independent experiments. *P* values were determined by unpaired two-tailed *t*-tests. NS, not significant.

suggesting that HER2 may be sequestered in alternate endocytic vesicles within 2 h of treatment. Treatment with Ptz-M6Pn for 2 h showed membrane-localized HER2 and did not indicate similar internalization. After 48 h, treatment with Ptz-M6Pn also induced a reduction and relocalization of HER2 signal (Extended Data Fig. 2b). These results suggest that there is a kinetic difference in internalization mediated by M6Pn-LYTACs and GalNAc-LYTACs, and that Ptz-GalNAc can remove membrane HER2 within 2 h.

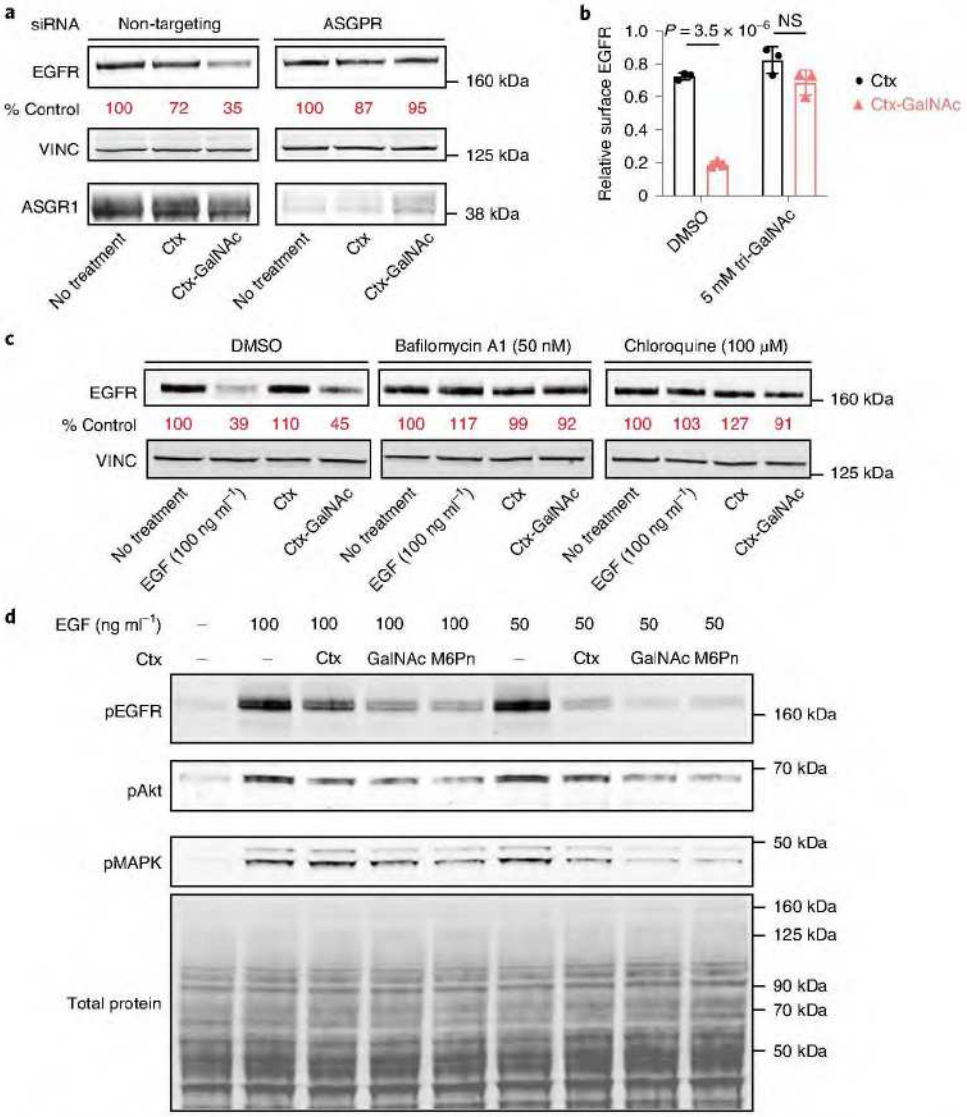

Fig. 3 | GalNAc-LYTACs operate via an endo-lysosomal mechanism and attenuate EGFR-driven signaling. a, Western blot of EGFR in HEP3B cells treated with 10 nM Ctx conjugates for 48 h following knockdown of ASGPR by siRNA. Non-targeting siRNA is included as a control. **b**, Degradation of EGFR in HEP3B cells as determined by live-cell flow cytometry following treatment for 24 h with 10 nM Ctx conjugates and either DMSO or 5 mM of exogenous tri-GalNAc ligand (**10**). **c**, Western blot of EGFR degradation in HEP3B cells incubated with 10 nM Ctx conjugates and 50 nM bafilomycin A1 or 10 μM chloroquine for 24 h. **d**, Western blot of pEGFR, pAkt and pMAPK in HEP3B cells following incubation with 10 nM Ctx conjugates for 48 h and 1 h of stimulation with 100 ng ml^{-1} or 50 ng ml^{-1} of EGF. Data in and **c** are representative of two independent experiments, and data in **d** are representative of three independent experiments. Data in **b** are shown as the mean of three independent experiments ± s.e.m. *P* values were determined by unpaired two-tailed *t*-tests.

GalNAc-LYTACs do not affect lysosomal health. Given that LYTACs mediate trafficking of membrane proteins to lysosomes, we asked if GalNAc-LYTACs affect lysosomal health in cells. Untreated HEP3B cells and cells treated with Ctx-GalNAc exhibited a similar number of lysosomes upon staining with Lysotracker, while staining intensity was reduced in cells treated with L-leucyl-L-leucine methyl ester (LLOMe), a lysosome-damaging reagent (Extended Data Fig. 3a). Untreated cells and Ctx-GalNAc-treated cells exhibited greater cathepsin B activity (Magic Red) than LLOMe-treated cells. Although per cell quantitation showed that Ctx-GalNAc treatment resulted in a reduction of cathepsin B activity compared to untreated cells, both displayed more activity than Ctx-treated cells (Extended Data Fig. 3b). This reduction of Magic Red signal by Ctx did not extend to other antibody treatments, as Ptz and Ptz-GalNAc did not show a significant change in cathepsin B activity compared to untreated HEPG2 cells (Extended Data Fig. 4a). We also examined the expression levels of ALG2-interacting protein X (ALIX), a marker for lysosomal membrane damage repair. While ALIX levels were increased in LLOMe-treated cells, untreated and Ctx-GalNAc-treated or Ptz-GalNAc-treated cells exhibited substantial reduction of ALIX staining. Ctx treatment induced a modest increase in ALIX staining, but this phenomenon was not observed following Ptz treatment (Extended Data Figs. 3c and 4b). Taken together, these data indicate that treatment with GalNAc-LYTACs does not disrupt lysosomal health relative to untreated cells.

Peptide-based LYTACs potentiate antiproliferation. Previous LYTACs targeting membrane proteins were based on antibody or antibody fragments as the target binders. Although antigen-binding fragments (Fab) non-specifically conjugated to several M6Pn polymers

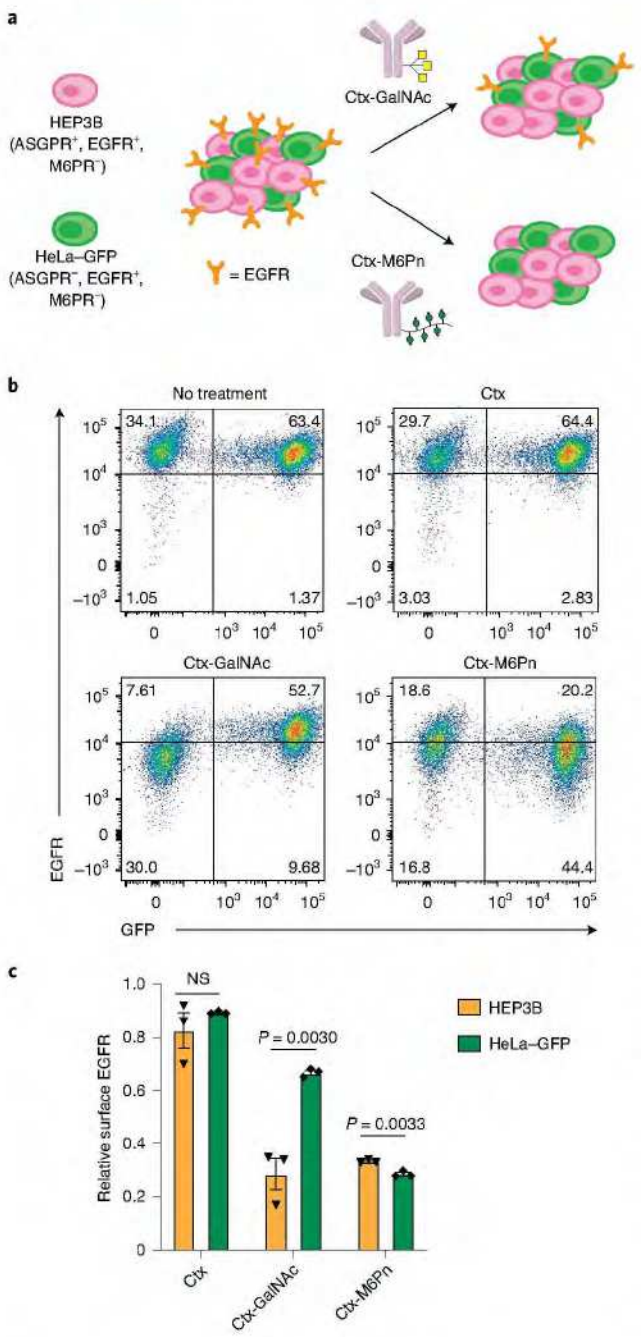

Fig. 4 | Ctx-GalNAc mediates selective degradation of EGFR in ASGPR-expressing cells. a, HEP3B cells (ASGPR+, EGFR+, M6PR+) and HeLa–GFP cells (ASGPR−, EGFR+, M6PR+) were cocultured and treated with Ctx conjugates. Ctx-GalNAc degrades EGFR selectively in HEP3B cells. **b**, Representative flow cytometry plot of cell surface EGFR levels in HEP3B cells and HeLa–GFP cells following coculture and treatment with 50 nM Ctx or Ctx conjugates for 48 h. **c**, Quantification of relative surface expression of EGFR in **b** as determined by live-cell flow cytometry. Data in **b** are representative of three independent experiments. Data in **c** are shown as the mean of three independent experiments ± s.e.m. *P* values were determined by unpaired two-tailed *t*-tests.

could induce degradation[13], we wondered if a small, synthetic peptide binder containing a single ASGPR ligand can promote degradation and induce enhanced functional consequences. To test this hypothesis, we used a targeting ligand composed of a polyspecific integrin-binding peptide (PIP), also known as EETI 2.5F, that was previously engineered to bind several tumor-associated integrins with high affinity[35]. In particular, PIP binds to $\alpha_v\beta_1$, $\alpha_v\beta_3$, $\alpha_v\beta_5$, $\alpha_v\beta_6$ and $\alpha_5\beta_1$ integrins, which are known to be overexpressed in various cancer types and facilitate proliferation, migration and metastasis[36]. Given that the 3.4-kDa PIP peptide is produced by solid-phase peptide synthesis[37], we readily incorporated azido-L-norvaline into the sequence to enable site-specific conjugation via a single tri-GalNAc-DBCO moiety, resulting in PIP-GalNAc (Fig. 5c and Supplementary Fig. 11).

We measured the surface levels of integrins by flow cytometry following treatment in HEPG2 cells and observed that PIP-GalNAc depleted cell surface $\alpha_v\beta_3$ integrin levels threefold relative to PIP treatment alone. Treatment with PIP increased the expression of integrin $\alpha_v\beta_5$ while PIP-GalNAc overturned this effect, resulting in modest degradation. Measurement of additional integrins that interact with PIP was challenging due to their low surface expression or a lack of a specific detection antibody. Nonetheless, we determined the total surface level of integrins that bind to PIP by utilizing a PIP–Fc fusion for staining of the Fc fragment[38]. Detection of PIP–Fc revealed that PIP-GalNAc depleted about 60% of integrins while PIP alone degraded 40% (Fig. 5d).

We then asked if PIP-GalNAc has an effect on the proliferation of HEPG2 cells compared to the parent peptide. PIP-GalNAc was substantially more effective at inhibiting proliferation than PIP at various concentrations and durations of treatment (Fig. 5e,f and Extended Data Fig. 5a). We validated that tri-GalNAc must be conjugated to PIP to potentiate antiproliferation, as co-incubation of PIP with an equimolar concentration of exogenous tri-GalNAc exhibited similar effects as incubation with PIP alone (Extended Data Fig. 5b). To verify the involvement of ASGPR on enhanced antiproliferation, cells were co-incubated with asialofetuin (ASF), which is a commonly used inhibitor of ASGPR[39,40] (Extended Data Fig. 5c). ASF ablated the enhanced antiproliferative effect of PIP-GalNAc, confirming that PIP-GalNAc must engage ASGPR. The antiproliferative phenotype induced by PIP-GalNAc persisted after conjugate wash-out, while wash-out rescued proliferation in PIP-treated cells. The long-acting inhibition of cell growth by PIP-GalNAc indicates that continuous incubation with a LYTAC is not required for modulating the phenotypic consequences resulting from cell surface depletion of certain targets (Fig. 5g). Moreover, cells treated with PIP-GalNAc displayed noticeable morphological changes. Untreated and PIP-treated cells generally displayed epithelial-like clusters, whereas the PIP-GalNAc-treated cells formed smaller, circular clusters over the course of 5 d following treatment (Fig. 5h). Previous work demonstrated that $\alpha_v\beta_3$ integrin expression is associated with tumor size, invasion and metastasis of HCC, and that antisense gene transfections of α_v and β_3 integrin reduced proliferation in HEPG2 cells[41,42]. Our results suggest that increased degradation of integrins by LYTACs can result in remarkably enhanced functional effects compared to the parent binder alone.

Site-specific LYTACs improve pharmacokinetics in vivo. Our original LYTACs were constructed by non-specific conjugation of M6Pn polymers to lysine residues on antibodies or Fabs. However, the heterogenous nature of both the polymeric ligands and conjugation chemistry prevented rigorous structure–function relationship studies. Similarly, non-specific functionalization with tri-GalNAc affords heterogeneous LYTACs that are difficult to rigorously analyze for rational improvement. The ability of PIP-GalNAc to promote degradation with a single tri-GalNAc ligand (Fig. 5) suggested that simplified antibody-based LYTACs might be similarly effective and enable the study of architectural features essential for optimal LYTAC activity. Therefore, we generated a panel of GalNAc-LYTACs based on Ctx and Ptz using site-specific conjugation chemistry

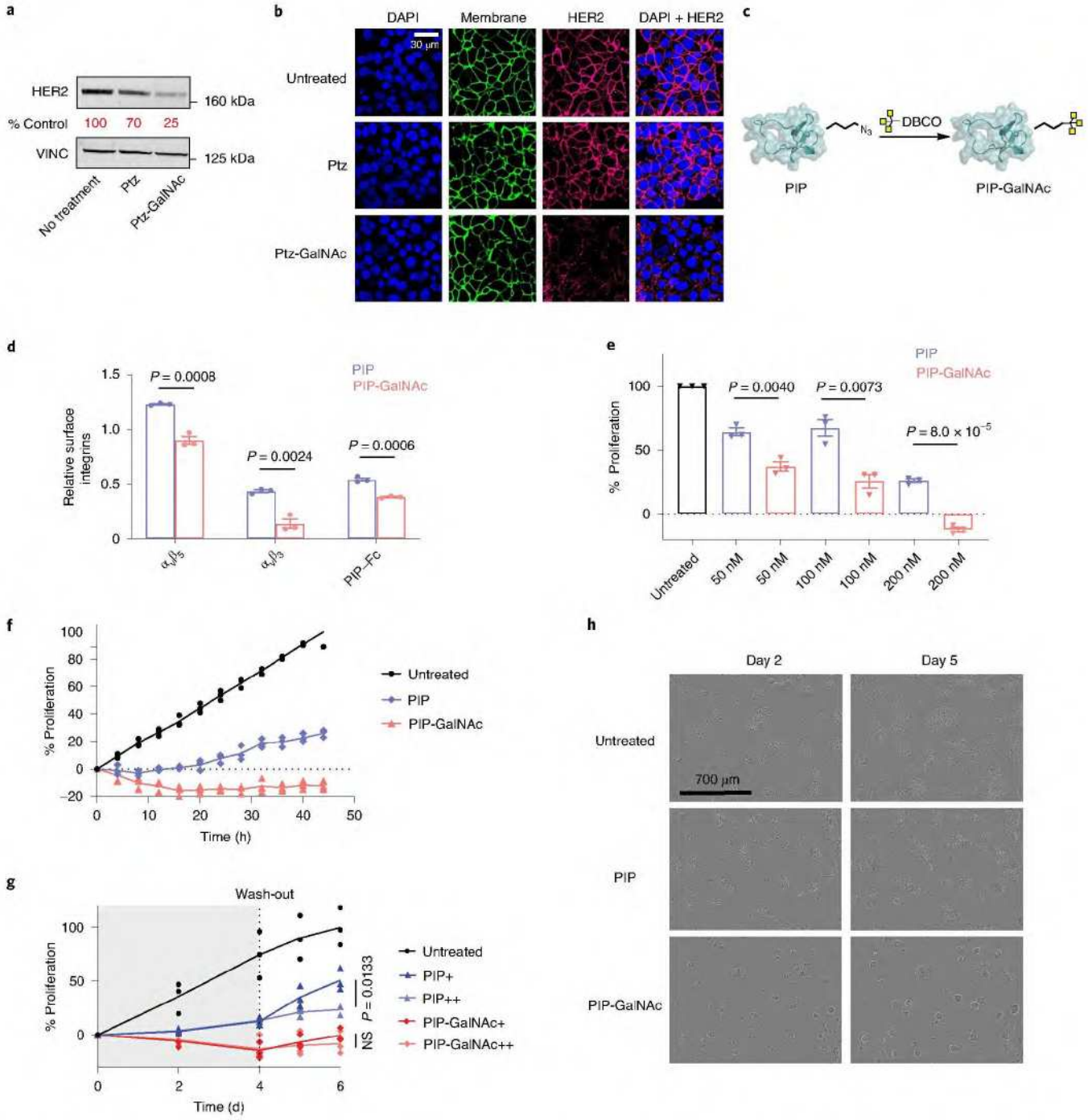

Fig. 5 | GalNAc-LYTAC degrades the membrane proteins HER2 and integrins and induces antiproliferative effects in HEPG2 cells. a, Western blot of HER2 degradation in HEPG2 cells following incubation with 100 nM Ptz or Ptz conjugates for 48 h. **b**, Visualization of HER2 degradation in HEPG2 cells by confocal microscopy after treatment with 100 nM Ptz or Ptz conjugates for 48 h. **c**, Synthesis of PIP-GalNAc. Tri-GalNAc-DBCO was conjugated to PIP, a knottin peptide that binds to multiple integrins. **d**, Degradation of cell surface integrins in HEPG2 cells as determined by live-cell flow cytometry following 44 h of treatment with 100 nM PIP or PIP-GalNAc. Anti-$\alpha_v\beta_3$, anti-$\alpha_v\beta_5$ and PIP-Fc fusion construct were used for detection. PIP was genetically fused to the Fc domain of a mouse IgG2a to generate a PIP-Fc fusion construct that measures the surface expression of integrins recognized by PIP. **e**, Percent proliferation of HEPG2 cells following 44 h of treatment with 50 nM, 100 nM or 200 nM PIP or PIP-GalNAc. Proliferation was quantified by phase confluence over time using IncuCyte. **f**, Time course of percent proliferation of HEPG2 cells during 44 h of treatment with 200 nM PIP or PIP-GalNAc. **g**, Percent proliferation of HEPG2 cells for 6 d following wash-out. Cells were treated with 200 nM PIP or PIP-GalNAc on day 0. PIP+ and PIP-GalNAc+ indicate the conditions where cells were washed on day 4 and replaced with fresh medium without treatment. PIP++ and PIP-GalNAc++ indicate the conditions where cells were washed on day 4 and replaced with fresh medium containing 200 nM PIP or PIP-GalNAc. **h**, Live HEPG2 imaging by IncuCyte throughout the 5 d after treatment with 100 nM PIP or PIP-GalNAc. Data in **a** are representative of three independent experiments. Images are representative of two independent experiments for **b** and three independent experiments for **h**. Data in **d**–**g** represent three independent experiments, where **d**,**e** show the mean of three independent experiments ± s.e.m. *P* values were determined by unpaired two-tailed *t*-tests.

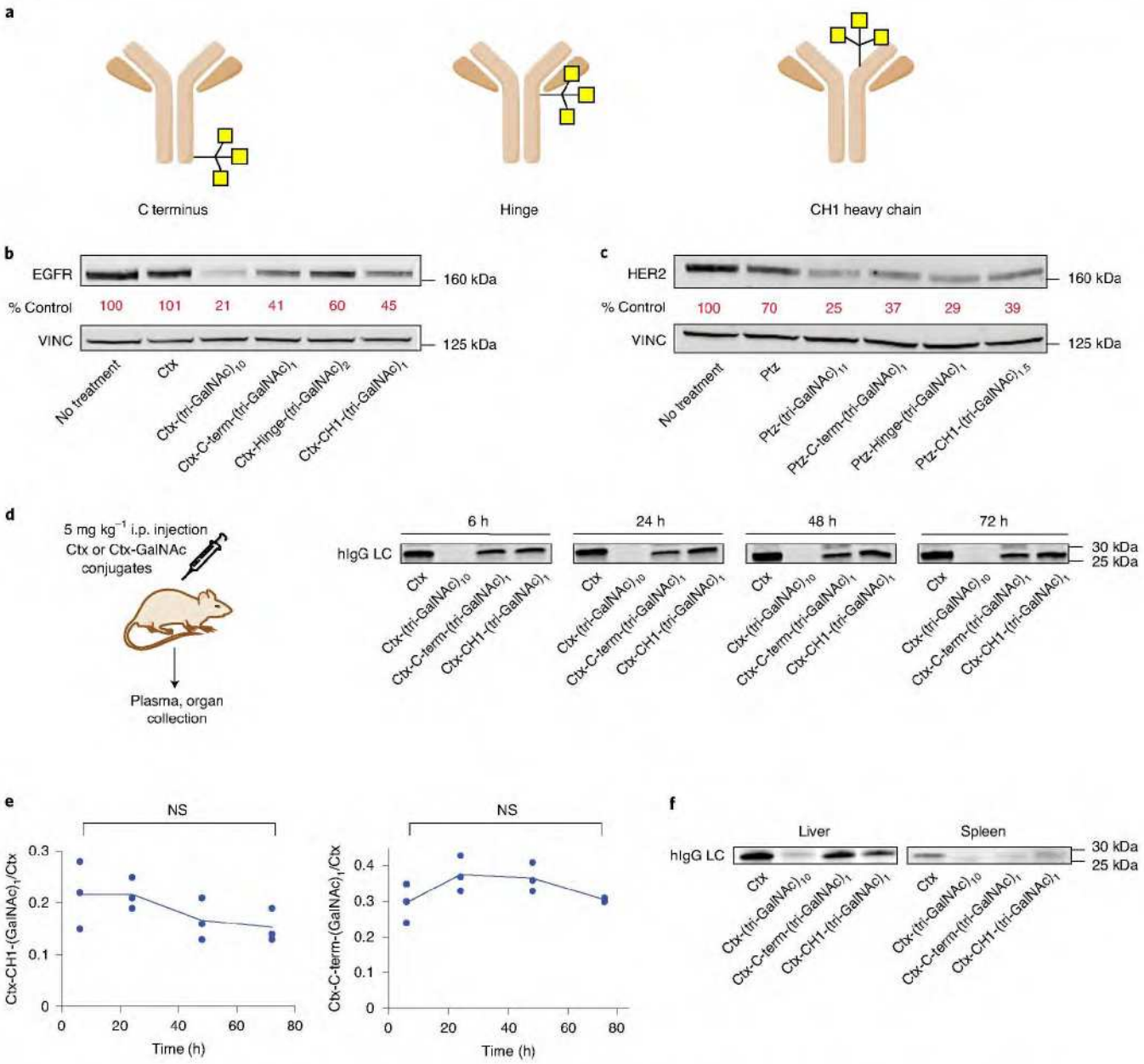

Fig. 6 | Site-specific conjugation improves pharmacokinetics of antibody-based GalNAc-LYTACs. a, Site-specific conjugation of antibody at the C-terminus, hinge and CH1 domain using SMARTag technology[43]. **b**, Western blot of EGFR degradation in HEP3B cells after treatment with 10 nM site-specific Ctx conjugates for 48 h. **c**, Western blot of HER2 degradation in HEPG2 cells after treatment with 100 nM site-specific Ptz conjugates for 48 h. **d**, In vivo pharmacokinetic study of GalNAc-LYTACs. Representative human IgG light chain (hIgG LC) western blot of plasma following 5 mg kg^{-1} intraperitoneal (i.p.) injection of Ctx, Ctx-(tri-GalNAc)$_{10}$, Ctx-CH1-(tri-GalNAc)$_1$ or Ctx-C-term-(tri-GalNAc)$_1$. Plasma was collected 6, 24, 48 and 72 h after injection. **e**, Quantification of **d**; data are shown as the ratio of site-specific Ctx conjugates over unmodified Ctx. Data represent the average of three independent mice ± s.e.m. **f**, Representative human IgG light chain blot of liver and spleen 72 h after Ctx and Ctx conjugate injections. Data in **b**–**d** and **f** are representative of three independent experiments. Data in **e** represent the mean of three independent experiments ± s.e.m. *P* values were determined by unpaired two-tailed *t*-tests.

via the SMARTag technology, which involves genetic encoding of a reactive aldehyde handle on a specific site of the antibody scaffold[43]. To create a stable linkage between the tri-GalNAc motif and the aldehyde, we utilized a hydrazino-iso-Pictet–Spangler (HIPS) reaction scheme[44,45] (Supplementary Fig. 12). To determine whether the location of tri-GalNAc ligand on the antibody scaffold would impact the degradation profile, we labeled three different sites of the antibodies, the C terminus, hinge and CH1 heavy chain (Fig. 6a and Extended Data Fig. 6a). For Ctx, conjugation at the hinge resulted in a ligand to antibody ratio of 2, while conjugation at the C terminus and CH1 positions resulted in a ligand to antibody ratio of 1 (Extended Data Fig. 6b,c). LYTACs resulting from site-specific conjugation at the C terminus and the CH1 heavy chain of Ctx demonstrated >50% degradation of EGFR, while conjugation at the hinge only showed 40% degradation despite the increased ligand to antibody ratio (Fig. 6b). Steric hindrance may be an issue in the

hinge region for bridging EGFR and ASGPR, resulting in modest differences in degradation efficiency. The degradation efficiency of the site-specific Ctx conjugates was slightly lower than that of the non-specifically labeled LYTACs. This could imply either that the antibody requires several tri-GalNAc moieties to achieve maximum degradation or that an optimal site for conjugation remains to be identified. However, we also generated site-specific conjugates based on Ptz (Extended Data Fig. 7) and observed that a single tri-GalNAc conjugation at the hinge showed comparable degradation (70%) as the non-specific Ptz-GalNAc, while attachment at the C terminus or the CH1 domain resulted in 60% degradation (Fig. 6c). This indicates that a homogeneous, site-specific GalNAc-LYTAC can achieve comparable degradation as the non-specific conjugate and that the optimal site of conjugation may differ between antibodies, potentially due to their different binding sites of the target and the resulting orientation of the LYTAC conjugate between ASGPR and the target.

We observed that site-specifically labeled Ctx conjugates maintained similar binding to EGFR but exhibited lower uptake efficiency in HEPG2 cells than the non-specific conjugates (Extended Data Fig. 8a,b). Based on these results, we asked whether site-specifically labeled conjugates might exhibit altered in vivo clearance profiles. To test this, BALB/c mice were intraperitoneally injected with 5 mg kg^{-1} of Ctx, non-specifically conjugated Ctx-$(GalNAc)_{10}$, Ctx-C-term-$(GalNAc)_1$ or Ctx-CH1-$(GalNAc)_1$, and plasma was collected at 6, 24, 48 and 72 h to analyze their clearance rate. Ctx-$(GalNAc)_{10}$ cleared rapidly before 6 h (Fig. 6d), implying frequent treatments would be required to maintain reduced EGFR levels given that degradation was not durable for more than 24 h in vitro following wash-off after LYTAC treatment (Extended Data Fig. 9). However, site-specific conjugates showed an initial clearance followed by sustained presence 72 h after injection (Fig. 6d,e), demonstrating that site-specific GalNAc-LYTACs may be advantageous in vivo due to less frequent dosing versus non-specific conjugates, thereby enhancing the potential for sustained degradation of membrane targets. However, non-specific conjugates may be preferred for rapid clearance of soluble targets.

Liver and spleen were collected at 72 h and probed for the presence of conjugates. Ctx and Ctx-GalNAc conjugates were present in the liver while only Ctx was present in the spleen, reaffirming that Ctx-GalNAc conjugates preferentially accumulate in the liver (Fig. 6f). Based on the clearance regimen of these non-specific and site-specific LYTAC conjugates, we evaluated hepatic toxicity in mice with two different dosing schedules. Both a liver function panel from mouse serum and liver histological analysis showed that neither treatment with non-specific nor site-specific Ctx-GalNAc result in toxicity in the liver compared to untreated mice (Extended Data Fig. 10). Altogether, these results demonstrate that we can modulate the clearance regimen of LYTACs by altering the number of ligands per antibody and that GalNAc-LYTACs are promising for future in vivo applications given their safety profiles even with repeated dosing.

Discussion

An advantage of LYTACs as a protein degradation modality is the ability to tune degradation to a specific cell type expressing a given lysosome-targeting receptor. To demonstrate this, we established that LYTACs can be designed to utilize ASGPR for liver cell-specific degradation. GalNAc-LYTACs efficiently ablated EGFR and HER2 in HCC cells. We verified that the mechanism of degradation was through the endo-lysosomal system and was dependent on ASGPR internalization. Increased trafficking of proteins to the lysosome did not significantly impact lysosomal health, suggesting that removal of a desired protein does not negatively impact lysosomal stability or homeostatic capabilities of a given cell and that LYTACs would be applicable to indications where avoiding cell damage is desirable. Coculture of HCC cells with cells lacking ASGPR demonstrated that GalNAc-LYTACs are indeed capable of cell-specific degradation. GalNAc-LYTACs degraded EGFR and induced more substantial abrogation of downstream kinase signaling than inhibition alone. A synthetic peptide with a single tri-GalNAc moiety was able to degrade integrins and resulted in substantial antiproliferative effects, which demonstrated that the structural design of LYTACs can be simplified to small conjugates. Finally, systematic variation of modification sites and GalNAc to antibody ratios through antibody engineering allowed us to optimize degradation activity and pharmacokinetic profiles in vivo. Broadly, GalNAc-LYTACs represent a strategy for receptor-mediated and cell-specific degradation that can be applied to membrane proteins relevant in liver diseases, such as HCC, that does not depend on cell penetrance or carrier degradation.

Additionally, we showed that GalNAc-LYTACs are far better at internalizing extracellular cargo than M6Pn-LYTACs in HEPG2 cells, likely resulting from the higher surface expression of ASGPR than CI-M6PR in hepatocytes. Despite the difference in surface levels of these receptors, GalNAc-LYTACs and M6Pn-LYTACs performed comparably in membrane protein degradation assays, although Ptz-GalNAc showed faster kinetics than Ptz-M6Pn. These observations suggest that factors other than expression levels of the recycling receptors modulate the degree of degradation. These factors might include the distinct sorting of these receptors, the rate of target release from the receptor to the lysosome, the rate of target turnover or the rate of receptor trafficking. Further studies that probe the mechanistic features influencing degradation mediated by endocytic receptors are needed and may provide insight into rational strategies to enhance degradation efficiency.

Recently, antibody-PROTAC conjugates demonstrated HER2-dependent degradation via a mechanism of delivery similar to antibody–drug conjugates[46]. However, a general approach for tissue-specific degradation utilizing the UPS or intracellular autophagy machinery would require ligand development campaigns for tissue-restricted E3 ligases or autophagy regulators[47,48]. GalNAc-LYTACs serve as an example for applications to other recycling receptors that may be exploited for cell-specific degradation, such as mannose receptors for macrophage-specific targeting[49] and CD22 for B cell-selective degradation[50]. Additional discovery of recycling receptors with distinct and exclusive localization would expand the range of tissues or cells that LYTACs can target with selectivity. We envision that further structure–function studies in combination with mechanistic investigations will determine the optimal architecture of LYTACs and provide structural understanding of degradation driven by lysosome-targeting receptors.

Online content

Any methods, additional references, Nature Research reporting summaries, source data, extended data, supplementary information, acknowledgements, peer review information; details of author contributions and competing interests; and statements of data and code availability are available at https://doi.org/10.1038/s41589-021-00770-1.

Received: 12 August 2020; Accepted: 10 February 2021;
Published online: 25 March 2021

References

1. Krönke, J. et al. Lenalidomide causes selective degradation of IKZF1 and IKZF3 in multiple myeloma cells. *Science* **343**, 301–305 (2014).
2. Lu, G. et al. The myeloma drug lenalidomide promotes the cereblon-dependent destruction of Ikaros proteins. *Science* **343**, 305–309 (2014).
3. Sakamoto, K. M. et al. Protacs: chimeric molecules that target proteins to the Skp1 Cullin F box complex for ubiquitination and degradation. *Proc. Natl Acad. Sci.* **98**, 8554–8559 (2001).

4. Winter, G. E. et al. Phthalimide conjugation as a strategy for in vivo target protein degradation. *Science* **348**, 1376–1381 (2015).
5. Nabet, B. et al. The dTAG system for immediate and target-specific protein degradation. *Nat. Chem. Biol.* **14**, 431–441 (2018).
6. Nabet, B. *et al* Rapid and direct control of target protein levels with VHL-recruiting dTAG molecules. *Nat. Commun.* **11, 4687** (2020).
7. Clift, D. et al. A method for the acute and rapid degradation of endogenous proteins. *Cell* **171**, 1692–1706 (2017).
8. Naito, M., Ohoka, N. & Shibata, N. SNIPERs—hijacking IAP activity to induce protein degradation. *Drug Discov. Today Technol.* **31**, 35–42 (2019).
9. Takahashi, D. et al. AUTACs: cargo-specific degraders using selective autophagy. *Mol. Cell.* **76**, 797–810 (2019).
10. Li, Z. et al. Allele-selective lowering of mutant HTT protein by HTT–LC3 linker compounds. *Nature* **575**, 203–209 (2019).
11. Li, Z., Zhu, C., Ding, Y., Fei, Y. & Lu, B. ATTEC: a potential new approach to target proteinopathies. *Autophagy* **16**, 185–187 (2020).
12. Mullard, A. First targeted protein degrader hits the clinic. *Nat. Rev. Drug Discov.* **18**, 237–239 (2019).
13. Banik, S. M. et al. Lysosome-targeting chimaeras for degradation of extracellular proteins. *Nature* **584**, 291–297 (2020).
14. Ghosh, P., Dahms, N. M. & Kornfeld, S. Mannose 6-phosphate receptors: new twists in the tale. *Nat. Rev. Mol. Cell Biol.* **4**, 202–213 (2003).
15. Zimmermann, T. S. et al. Clinical proof of concept for a novel hepatocyte-targeting GalNAc-siRNA conjugate. *Mol. Ther.* **25**, 71–78 (2017).
16. Spiess, M. The asialoglycoprotein receptor: a model for endocytic transport receptors. *Biochemistry* **29**, 10009–10018 (1990).
17. Park, E. I., Mi, Y., Unverzagt, C., Gabius, H.-J. & Baenziger, J. U. The asialoglycoprotein receptor clears glycoconjugates terminating with sialic acidα2,6GalNAc. *Proc. Natl Acad. Sci.* **102**, 17125–17129 (2005).
18. Stockert, R. J. The asialoglycoprotein receptor: relationships between structure, function, and expression. *Physiol. Rev.* **75**, 591–609 (1995).
19. Matsuda, S. et al. siRNA conjugates carrying sequentially assembled trivalent *N*-acetylgalactosamine linked through nucleosides elicit robust gene silencing in vivo in hepatocytes. *ACS Chem. Biol.* **10**, 1181–1187 (2015).
20. Springer, A. D. & Dowdy, S. F. GalNAc-siRNA conjugates: leading the way for delivery of RNAi therapeutics. *Nucleic Acid Ther.* **28**, 109–118 (2018).
21. Prakash, T. P. et al. Targeted delivery of antisense oligonucleotides to hepatocytes using triantennary *N*-acetyl galactosamine improves potency 10-fold in mice. *Nucleic Acids Res.* **42**, 8796–8807 (2014).
22. Kanasty, R., Dorkin, J. R., Vegas, A. & Anderson, D. Delivery materials for siRNA therapeutics. *Nat. Mater.* **12**, 967–977 (2013).
23. Lee, Y. C. et al. Binding of synthetic oligosaccharides to the hepatic Gal/GalNAc lectin. Dependence on fine structural features. *J. Biol. Chem.* **258**, 199–202 (1983).
24. Nair, J. K. et al. Multivalent *N*-acetylgalactosamine-conjugated siRNA localizes in hepatocytes and elicits robust RNAi-mediated gene silencing. *J. Am. Chem. Soc.* **136**, 16958–16961 (2014).
25. Huang, X., Leroux, J.-C. & Castagner, B. Well-defined multivalent ligands for hepatocytes targeting via asialoglycoprotein receptor. *Bioconjug. Chem.* **28**, 283–295 (2017).
26. Huang, Y. Preclinical and clinical advances of GalNAc-decorated nucleic acid therapeutics. *Mol. Ther. Nucleic Acids* **6**, 116–132 (2017).
27. Fitzgerald, K. et al. A highly durable RNAi therapeutic inhibitor of PCSK9. *N. Engl. J. Med.* **376**, 41–51 (2017).
28. Probert, M. A., Zhang, J. & Bundle, D. R. Synthesis of α- and β-linked tyvelose epitopes of the *Trichinella spiralis* glycan: 2-acetamido-2-deoxy-3-*O*-(3,6-dideoxy-D-arabino-hexopyranosyl)-β-D-galactopyranosides. *Carbohydr. Res.* **296**, 149–170 (1996).
29. Ezzoukhry, Z. et al. EGFR activation is a potential determinant of primary resistance of hepatocellular carcinoma cells to sorafenib. *Int. J. Cancer* **131**, 2961–2969 (2012).
30. Blivet-Van Eggelpoël, M.-J. et al. Epidermal growth factor receptor and HER-3 restrict cell response to sorafenib in hepatocellular carcinoma cells. *J. Hepatol.* **57**, 108–115 (2012).
31. Baselga, J. et al. Phase II multicenter study of the antiepidermal growth factor receptor monoclonal antibody cetuximab in combination with platinum-based chemotherapy in patients with platinum-refractory metastatic and/or recurrent squamous cell carcinoma of the head and neck. *J. Clin. Oncol.* **23**, 5568–5577 (2005).
32. Vermorken, J. B. et al. Open-label, uncontrolled, multicenter phase II study to evaluate the efficacy and toxicity of cetuximab as a single agent in patients with recurrent and/or metastatic squamous cell carcinoma of the head and neck who failed to respond to platinum-based therapy. *J. Clin. Oncol.* **25**, 2171–2177 (2007).
33. Bondeson, D. P. et al. Lessons in PROTAC design from selective degradation with a promiscuous warhead. *Cell Chem. Biol.* **25**, 78–87 (2018).
34. Shi, J.-H. et al. Recognition of HER2 expression in hepatocellular carcinoma and its significance in postoperative tumor recurrence. *Cancer Med.* **8**, 1269–1278 (2019).
35. Kimura, R. H., Levin, A. M., Cochran, F. V. & Cochran, J. R. Engineered cystine knot peptides that bind $\alpha_v\beta_3$, $\alpha_v\beta_5$, and $\alpha_5\beta_1$ integrins with low-nanomolar affinity. *Proteins* **77**, 359–369 (2009).
36. Desgrosellier, J. S. & Cheresh, D. A. Integrins in cancer: biological implications and therapeutic opportunities. *Nat. Rev. Cancer* **10**, 9–22 (2010).
37. Cox, N., Kintzing, J. R., Smith, M., Grant, G. A. & Cochran, J. R. Integrin-targeting knottin peptide–drug conjugates are potent inhibitors of tumor cell proliferation. *Angew. Chem. Int. Ed. Engl.* **55**, 9894–9897 (2016).
38. Kwan, B. H. et al. Integrin-targeted cancer immunotherapy elicits protective adaptive immune responses. *J. Exp. Med.* **214**, 1679–1690 (2017).
39. Arangoa, M. A., Düzgüneş, N. & Tros de Ilarduya, C. Increased receptor-mediated gene delivery to the liver by protamine-enhanced-asialofetuin-lipoplexes. *Gene Ther.* **10**, 5–14 (2003).
40. Treichel, U., Meyer zum Büschenfelde, K. H., Dienes, H. P. & Gerken, G. Receptor-mediated entry of hepatitis B virus particles into liver cells. *Arch. Virol.* **142**, 493–498 (1997).
41. Jin, Y. et al. OPN and $\alpha_v\beta_5$ expression are predictors of disease severity and worse prognosis in hepatocellular carcinoma. *PLoS ONE* **9**, e87930 (2014).
42. Li, J. et al. Antisense integrin α_v and β_3 gene therapy suppresses subcutaneously implanted hepatocellular carcinomas. *Dig. Liver Dis.* **39**, 557–565 (2007).
43. Rabuka, D., Rush, J. S., deHart, G. W., Wu, P. & Bertozzi, C. R. Site-specific chemical protein conjugation using genetically encoded aldehyde tags. *Nat. Protoc.* **7**, 1052–1067 (2012).
44. Agarwal, P. et al. Hydrazino-Pictet–Spengler ligation as a biocompatible method for the generation of stable protein conjugates. *Bioconjug. Chem.* **24**, 846–851 (2013).
45. Gray, M. et al. Targeted glycan degradation potentiates the anticancer immune response in vivo. *Nat. Chem. Bio* **16**, 1376–1374 (2020).
46. Maneiro, M. *et al* Antibody-PROTAC conjugates enable HER2-dependent targeted protein degradation of BRD4. *ACS Chem. Biol.* **15**, 1306–1312 (2020).
47. Lai, A. C. & Crews, C. M. Induced protein degradation: an emerging drug discovery paradigm. *Nat. Rev. Drug Discov.* **16**, 101–114 (2017).
48. Schapira, M., Calabrese, M. F., Bullock, A. N. & Crews, C. M. Targeted protein degradation: expanding the toolbox. *Nat. Rev. Drug Discov.* **18**, 949–963 (2019).
49. Stahl, P. D. The macrophage mannose receptor: current status. *Am. J. Respir. Cell Mol. Biol.* **2**, 317–318 (1990).
50. O'Reilly, M. K., Tian, H. & Paulson, J. C. CD22 is a recycling receptor that can shuttle cargo between the cell surface and endosomal compartments of B cells. *J. Immunol.* **186**, 1554–1563 (2011).

Methods

General chemical synthesis procedures. Reagent-grade chemical reagents were purchased from Carbosynth, Sigma-Aldrich, TCI and Click Chemistry Tools. All chemical reactions were performed in standard, flame-dried glassware capped with rubber septa under an inert atmosphere of nitrogen unless stated otherwise. Stainless steel syringes or cannulae were used to transfer moisture-sensitive liquids. Anhydrous solvents (dichloromethane and *N*,*N*-dimethylformamide) were prepared by passage through an activated alumina column. Thin layer chromatography (TLC) was conducted on precoated glass plates covered with 0.2-mm silica gel for monitoring reactions. TLC was visualized with ultraviolet (UV) light, 5% sulfuric acid in methanol and ninhydrin stain. Reaction mixtures were purified via column chromatography using Biotage SNAP KP-Sil or Ultra C18 cartridges (10–100 g) with a Biotage Isolera Prime ACI automated fraction collector.

Chemical analysis instrumentation. Proton NMR (^{1}H NMR) spectra were recorded on a Varian 400 spectrometer and proton-decoupled carbon-13 NMR (^{13}C {^{1}H} NMR) spectra were recorded on a Varian 500 NMR spectrometer at 25 °C. Spectra were reported in ppm downfield of tetramethylsilane and are referenced to the residual resonances of the protium NMR solvent (CD_2OD: 3.31 [methanol]) and carbon NMR solvent (CD_3OD: 49.00 [methanol]). MestReNova (v12.0.3) was used for all chemical NMR analysis. Data are reported as chemical shift, multiplicity (br, broad; s, singlet; d, doublet; t, triplet; q, quartet; quin, quintet; sept, septet; m, multiplet), coupling constants in Hertz (Hz) and integration. High-resolution mass spectrometric data were obtained on a Thermo Exactive Orbitrap mass spectrometer by the Stanford University Mass Spectrometry (SUMS) core facility.

Cell lines and reagents. Adherent cells were cultured in T75 flasks or 15-cm plates at 37 °C and 5% CO_2. HEP3B cells (ATCC), HUH7 cells (JCRB) and HeLa–GFP cells (MyBioSource) were cultured in DMEM supplemented with 10% FBS and 1% penicillin/streptomycin. HEPG2 cells (ATCC) were cultured in DMEM with low glucose supplemented with 10% FBS and 1% penicillin/streptomycin. Expi293 cells expressing formylglycine-generating enzyme from *Mycobacterium tuberculosis* (tbFGE) were a generous gift from M.A. Gray and were cultured with Expi293 Expression Medium (Thermo Fisher Scientific) supplemented with 2 μg ml^{-1} puromycin in 250 ml polycarbonate shaker flasks (Corning) maintained at 37 °C and 8% CO_2 with rotation (120 r.p.m.). Antibodies used in this study are listed in Supplementary Table 1.

LYTAC antibody conjugation. *General procedure for antibody azide labeling.* A 2 mg ml^{-1} solution of antibody was buffer exchanged into PBS using a 7K Zeba size-exclusion column. The antibody was reacted with 25 equiv. of NHS-$(PEG)_4$-azide (20 mg ml^{-1} in DMSO), and the reaction was incubated overnight at room temperature. The reaction mixture was filtered using a 7K Zeba size-exclusion column to yield the conjugated antibody.

General procedure for antibody tri-GalNAc labeling. Tri-GalNAc-DBCO (100 equiv.) was weighed into an Eppendorf tube, and a 2 mg ml^{-1} solution of antibody-$(PEG)_4$-N_3 was added. The reaction was manually agitated until the mixture was homogeneous. The reaction mixture was allowed to incubate at room temperature in the dark for 3 d and was filtered using a 40K Zeba size-exclusion column.

HEPG2 internalization assay. HEPG2 cells were plated (100,000 cells per well in a 24-well plate) 2 d before the experiment. Cells were incubated with 200 μl of complete growth medium with 50 nM rabbit or human IgG-647 and 25 nM goat anti-rabbit, Ctx or M6Pn or GalNAc-LYTACs for 1 h. Following incubation, cells were washed with PBS three times, trypsinized and then transferred to a 96-well V-bottom plate. Cells were washed three times with PBS + 0.5% BSA + 5 mM EDTA and incubated with Sytox Green for 15 min on ice before flow cytometry analysis.

HEPG2 colocalization live-cell imaging. To make rabbit IgG-647, a 2 mg ml^{-1} solution of rabbit IgG (Bio X Cell) was reacted with 15 equiv. of NHS-AF647 (Thermo Fisher Scientific) overnight at room temperature. The reaction mixture was filtered using a 7K Zeba size-exclusion column to yield the conjugated antibody.

HEPG2 cells were plated (30,000 cells per well in an 8-well Labtek plate) 2 d before the experiment. Cells were incubated with 200 μl of complete growth medium with 50 nM rabbit IgG-647 and 25 nM goat anti-rabbit, goat anti-rabbit M6Pn or goat anti-rabbit GalNAc for 1 h. Following incubation, cells were washed with HBSS and incubated with 50 nM Lysotracker in HBSS for 30 min at 37 °C. Cells were then washed with HBSS three times, incubated with Hoechst for 5 min and imaged by confocal microscopy.

Protein degradation analysis by western blot. Adherent cells were plated (100,000 cells per well in a 24-well plate) 1 d before the experiment. Cells were incubated with 250 μl of complete growth medium with 10 nM LYTAC or controls for the indicated amount of time. Cells were then washed with DPBS three times and lysed with RIPA buffer supplemented with protease inhibitor cocktail (Roche), 0.1% benzonase (Millipore-Sigma) and phosphatase inhibitor cocktail (Cell Signaling Technologies) on ice for 30 min. The cells were scraped, transferred to Eppendorf tubes and centrifuged at 21,000*g* for 15 min at 4 °C. The supernatant was collected and the protein concentration was determined by BCA assay (Pierce). Equal amounts of lysate were loaded onto a 4–12% Bis-Tris gel and separated by SDS–PAGE. The gel was then transferred onto a nitrocellulose membrane, stained with REVERT Total Protein Stain (LI-COR) and blocked with Odyssey Blocking Buffer (TBS) (LI-COR) for 1 h at room temperature. The membrane was incubated with primary antibody overnight at 4 °C and washed three times with TBS with 0.1% Tween-20 (TBS-T). Subsequently, the membrane was incubated with secondary antibody for 1 h at room temperature and washed three times with TBS-T for visualization with an Odyssey CLx Imager (LI-COR). Image Studio (LI-COR) was used to quantify band intensities.

Cell surface EGFR and HER2 degradation analysis by flow cytometry. Adherent cells were plated (100,000 cells per well in a 24-well plate) 1 d before the experiment. Cells were incubated with 250 μl of complete growth medium with 10 nM LYTAC or controls for the indicated amount of time, washed with PBS three times, trypsinized for <5 min and transferred to a 96-well V-bottom plate. Cells were washed three times with PBS + 0.5% BSA + 5 mM EDTA (FACS buffer), incubated with primary antibody for 30 min on ice, washed three times with FACS buffer and incubated with secondary antibody for 30 min on ice. After washing three times with FACS buffer, cells were incubated with either Sytox Green or Sytox Blue for 15 min on ice. Flow cytometry was performed on either a BD LSR II or BD Accuri C6 Plus, and FlowJo software was used to gate on single cells and live cells for analysis. A representative gating strategy is shown in Supplementary Fig. 13.

Cell surface integrin degradation analysis by flow cytometry. HEPG2 cells were plated (100,000 cells per well in a 24-well plate) 1 d before the experiment. Cells were incubated with 250 μl of complete growth medium with 100 nM of PIP or PIP-GalNAc for 48 h. Cells were washed with integrin-binding buffer (20 mM Tris pH 7.4, 0.1% BSA, 150 mM NaCl, 2 mM $CaCl_2$, 1 mM $MgCl_2$, 1 mM $MnCl_2$) and stained with primary antibodies on ice. For PIP–Fc staining, cells were washed with 5 mM EDTA in PBS to remove bound PIP following treatments and then stained with PIP–Fc (mouse IgG2a). After primary incubation, cells were washed three times with PBS + 0.5% BSA (PBSA) and incubated with secondary antibody in PBSA for 30 min on ice. After secondary incubation, cells were prepared for flow cytometry analysis as described above.

Confocal microscopy for membrane protein degradation. Adherent cells were plated (30,000 cells per well in an 8-well Labtek plate) 1 d before the experiment. Cells were incubated with 200 μl of complete growth medium with 10 nM LYTAC or controls for the indicated amount of time. Cells were then washed with DPBS and stained with Membrite according to the manufacturer's protocol. Cells were fixed with 4% paraformaldehyde in PBS for 20 min at room temperature, washed three times and permeabilized with 0.1% Triton X-100 in PBS for 5 min at 4 °C. Cells were washed three times with DPBS, blocked in 10% goat serum in PBS for 1 h at room temperature and incubated with primary antibody overnight at 4 °C. After washing with DPBS, cells were incubated with secondary antibody and DAPI for 1 h at room temperature. Cells were washed with DPBS and imaged with a Nikon A1R confocal microscope using a Plan Fluor ×60, 1.30-NA oil objective. The following laser settings were used: 405-nm violet laser, 488-nm blue laser, 561-nm green laser and 639-nm red laser.

siRNA knockdown. HEP3B cells (75,000 cells per well in a 24-well plate) were transfected with 20 pmoles of siRNA (Dharmacon) and jetPRIME reagent according to the manufacturer's specifications.

EGF-stimulated phosphorylation. HEP3B cells were plated (100,000 cells per well in a 24-well plate) 1 d before the experiment. Cells were incubated with 250 μl of complete growth medium with 10 nM LYTAC or controls for 48 h. Following incubation, cells were washed three times with PBS. EGF (50 ng ml^{-1} or 100 ng ml^{-1}) was added and cells were incubated for 1 h at 37 °C. Cells were washed and lysed for western blot analysis.

Coculture assay. HEP3B cells (100,000 cells per well) and GFP–HeLa cells (20,000 cells per well) were cocultured in 24-well plates. Cells were then treated with 50 nM of Ctx conjugates for 48 h, and surface-level EGFR was assessed by flow cytometry.

Lysosomal health assay. HEP3B cells were plated (30,000 cells per well in an 8-well Labtek plate) and treated with 10 nM Ctx or Ctx-GalNAc for 48 h or with 1 mM of LLOMe for 1 h. Cells were then treated with the indicated markers. For all conditions, ImageJ was used to set the same threshold across images and to quantify fluorescence.

Lysotracker Red. Lysotracker Red (100 nM final concentration) was added to each well and incubated at 37 °C for 30 min protected from light. Following incubation, cells were washed with DPBS, fixed with 4% paraformaldehyde, washed and stained with DAPI for 15 min.

Magic Red. Magic Red (Immunochemistry) was resuspended in DMSO and diluted according to the manufacturer's specifications. Diluted Magic Red solution (8 µl) was added to each well (200 µl), and cells were incubated at 37 °C for 30 min protected from light. Following incubation, cells were washed with DPBS, fixed with 4% paraformaldehyde, washed and stained with DAPI for 15 min.

ALIX. Cells were washed, fixed with 4% paraformaldehyde and permeabilized with 0.1% Triton X-100. Cells were washed and blocked with 10% goat serum in PBS for 1 h and incubated with ALIX primary antibody (BioLegend) overnight at 4 °C. After incubation, cells were washed and stained with secondary antibody and DAPI.

Generation of PIP-GalNAc. *Synthesis of PIP.* Solid-phase peptide synthesis, peptide cleavage and folding methods are described in previous work that utilized azide-modified knottin synthesis[37]. It is important to note that 1,2-ethanedithiol (EDT) is excluded from the cleavage cocktail in this protocol because it reduces the azide of the unnatural amino acid. Briefly, solid-phase peptide synthesis with standard Fmoc conditions was used to synthesize PIP with an unnatural amino acid, 5-azido-L-norvaline, at position 15. In this work, we also substituted tyrosine in place of phenylalanine at position 31 to facilitate peptide detection and concentration measurements by UV absorbance at 280 nm. The method used for HPLC purification was a linear gradient from 10% solvent B to 46% solvent B over 32 min (solvent A, water + 0.1% trifluoroacetic acid; solvent B, acetonitrile + 0.1% trifluoroacetic acid). A C18 prep column (Microsorb 100-5 C18 Dynamax, 5 µm, 21.4 mm × 250 mm; Agilent) was used at a 20 ml min^{-1} flow rate.

PIP-GalNAc conjugation. Tri-GalNAc-DBCO (5 mg ml^{-1}, 3 equiv.) was added to PIP (1.88 mM in PBS). The reaction was incubated overnight at room temperature and purified by HPLC using an Agilent Infinity Lab Poroshell 120 EC-C19 4.6 nm × 50 nm analytical LC column with a linear gradient from 10% solvent B to 46% solvent B over 32 min (solvent A, water + 0.1% trifluoroacetic acid; solvent B, acetonitrile + 0.1% trifluoroacetic acid) at 0.4 ml min^{-1}.

Antiproliferation assay. HEPG2 cells (100,000 cells per well in a 24-well plate) were treated with various concentrations of PIP or PIP-GalNAc. After treatments were added, cells were imaged every 4 h for the indicated times in the IncuCyte S3 Live-Cell Analysis system using the phase-imaging channel and a ×10 objective. For co-incubation experiments with ASF, 10 mg ml^{-1} of ASF (Sigma-Aldrich) was treated with either PIP or PIP-GalNAc.

The following analysis parameters were used to quantify phase confluence (%) in the Incucyte software: segmentation adjustment was set to 1, hole fill (µm²) was set to 300 and area minimum (µm²) was set to 150. No other constraints were selected.

Percent proliferation was then calculated by normalizing phase confluence values. Specifically, at any given timepoint n in the treatment time course ($t=0 \rightarrow t=n$), the change in confluence from $t=0$ to $t=n$ (Δconfluence $_{t=n}$) was calculated for each well as follows: Δconfluence $_{t=n}$ of well x = (confluence $_{t=n}$ of well x) − (confluence $_{t=0}$ of well x), where x represents any given well in the experiment. This ensures that the value of each well is set to 0 at $t=0$. The average Δconfluence at the final time point of the untreated wells was set as the 'max value' (equivalent to 100% proliferation). Finally, data were normalized as follows:

$$\%\ \text{proliferation}_{t=n}\ \text{of well}\ x = (\Delta\text{confluence}_{t=n}\ \text{of well}\ x)/(\text{max value})$$

Site-specific antibody expression. *Plasmids of antibodies with SMARTag.* Ctx and Ptz with SMARTag plasmid sequences are listed in the Supplementary Note 2. Plasmids were transformed into Stellar competent *Escherichia coli* and isolated using PureLink HiPure Plasmid Filter Maxiprep Kit (Thermo Fisher Scientific).

Expression and purification of aldehyde-tagged Ctx antibodies. Antibodies were expressed in FGE-expressing Expi293 cells (a generous gift from M.A. Gray) following Thermo Fischer Scientific's Expi293 expression protocol. One microgram (0.5 µg heavy chain- and 0.5 µg light chain-encoding plasmid) of DNA per milliter of culture was used for transfection. Antibodies were collected after 7 d by removing the supernatant following centrifugation at 300*g* for 5 min and then centrifugation at 3,200*g* for 30 min at 4 °C. The supernatant was filtered using a 0.22-µm filter unit (Thermo Fischer Scientific). Antibodies were purified using Protein A-Sepharose 4B (Thermo Fisher Scientific) column chromatography in the dark. Protein A beads were packed into an Econo-Pac chromatography column (BioRad). The beads were then washed with elution buffer (100 mM glycine in Milli-Q water, pH 2.8) and equilibrated in PBS. The filtered supernatant was run through the Protein A column three times, washed with PBS three times and eluted with elution buffer into a Falcon tube containing 100 µl of 1 M Tris buffer, pH 8. Antibody was then buffer exchanged to citrate buffer (50 mM sodium citrate, 50 mM NaCl, pH 5.5) using a 30-kDa Amicon Centrifugal Filter.

Site-specific antibody conjugation. HIPS-azide[44,45] was resuspended in DMSO to 5 mg ml^{-1} and was added to aldehyde-tagged antibody in citrate buffer. The reaction was agitated overnight at 37 °C protected from light. Upon reaction completion, the reaction mixture was filtered using a 40-kDa Zeba size-exclusion column. Tri-GalNAc-DBCO (50 equiv.) was then added to antibody labeled with HIPS-azide (>1 mg ml^{-1}), and the reaction mixture was incubated at room temperature for 3 d in the dark. The reaction mixture was filtered using a 40-kDa Zeba size-exclusion column and the protein concentration was determined from A_{280} using a Nanodrop 200 Spectrophotometer.

Mass spectrometry. *Matrix-assisted laser desorption/ionization–mass spectrometry.* Samples were prepared by mixing the antibody sample with 1 µl of SPA matrix (7.5 mg ml^{-1} in 0.1% trifluoroacetic acid and 50% acetonitrile). The mixture was vortexed and loaded onto a MALDI stainless steel plate. The sample was dried at room temperature, and the MALDI–MS was acquired by AB SCIEX TOF/TOF and a 5800 CovalX High Mass Detector with a mass range of 10,000–250,000 Da and a laser intensity of 5,000–5,300. Data were analyzed by AB SCIEX.

PIP and PIP-GalNAc mass spectrometry. Samples were analyzed by ESI–MS on an Agilent 1260 HPLC and Bruker MicroTOF-Q II. The samples were run in a BioResolve RP mAb Polyphenyl column (450 Å, 100 × 2.1 mm) from Waters with a flow rate of 0.3 ml min^{-1}. The injection volume was 2 µl. Data were collected in full scan MS mode. The collision RF setting was 800 Vpp.

Site-specific antibody analysis. Approximately 15–20 µg of each antibody conjugate in PBS was brought up to 50 µl with 100 mM Tris, pH 8. Conjugates were reduced with 5 mM dithiothreitol for 18 min at 55 °C, and cysteines were alkylated with 20 mM iodoacetamide for 30 min at room temperature in the dark. Trypsin (Promega) was added at an approximate 1:50 protease to protein ratio, and in-solution digestions proceeded overnight (~16 h) at room temperature. The digestion was quenched by acidifying with formic acid before desalting with a 10-mg Strata-X polymeric reversed-phase cartridge (Phenomenex). Desalting steps included (1) conditioning the cartridge with 1 ml of acetonitrile, (2) addition of 1 ml of 0.2% formic acid in water, (3) loading the digestion mixture onto the cartridge and (4) washing with 1 ml of 0.2% formic acid in water. Peptides were eluted with 400 ul of 0.2% formic acid in 80% acetonitrile, dried via lyophilization and resuspended at 1 µg $µl^{-1}$ in 0.2% formic acid.

Peptides were analyzed using 90-min LC–MS/MS methods with a gradient that increased from 0% to 5% B over the first 6 min of the analysis, followed by an increase from 5% to 40% B from 6 min to 70 min, an increase from 40% to 90% B from 70 min to 71 min, isocratic flow at 90% B from 71 min to 76 min and a re-equilibration at 0% for 14 min. Mobile phases A and B were water and acetonitrile, respectively, each with 0.2% formic acid. Peptides were separated over a 25-cm EASY-Spray reversed-phase LC column (75-µm inner diameter packed with 2-µm, 100-Å PepMap C18 particles; Thermo Fisher Scientific), and precursors were ionized using an EASY-Spray ionization source (Thermo Fisher Scientific) held at +2.2 kV compared to ground. The column temperature was held at 45 °C, and the inlet capillary temperature was held at 275 °C. Survey scans of peptide precursors were collected in the Orbitrap from 350–1350 Th with an AGC target of 1,000,000, a maximum injection time of 50 ms, RF lens at 60% and a resolution of 60,000 at 200 *m/z*. Monoisotopic precursor selection was enabled for peptide isotopic distributions, precursors were selected for data-dependent MS/MS scans for 2 s of cycle time and dynamic exclusion was set to exclude after three times with an exclusion duration of 10 s and a ±10 ppm window set around the precursor monoisotope. Precursor ions with $z=2$–4 were isolated with a 1-*m/z* window with the quadruple and fragmented with both HCD at a normalized collision energy of 30 and ETD with supplemental HCD activation of 25 nce (EThcD) and calibrated charged dependent ETD parameters enabled[51]. Precursor ions with $z=5$–10 were only fragmented with EThcD using the same conditions. Product ions from all MS/MS events were mass analyzed in the Orbitrap with a resolution of 60,000 at 200 *m/z* with an AGC target of 50,000 and a maximum injection time of 118 ms. The mass range was set to automatic (normal) with a first mass set to 100 *m/z*. Precursor priorities were set to favor highest charge state and lowest *m/z* precursor ions, and an isolation window of 2 Th was used to select precursor ions with the quadrupole.

Separate fasta files were created for each Ctx and Ptz conjugate. For each, the canonical antibody sequence was included in addition to sequences that included the SMARTag sequence at various locations as described in the text. SMARTag sequences included two versions, one with the cysteine remaining and one with the cysteine as a glycine to represent conversion by the formylglycine-generating enzyme. Raw files were searched against corresponding fasta sequences using MetaMorpheus[52], and custom modifications were created for formylglycine (CO), HIPS-azide modifier (C23H33N7O4) and the intact tri-GalNAc modification (105H160N18O33). These searches confirmed exclusive modification at expected SMARTag sequences. Carbamidomehtylation of cysteine was set as a fixed modification with formylglycine and HIPS-azide and tri-GalNAc as variable modifications on glycine. Tryptic cleavage specificity was set with up to two missed cleavages allowed. Appropriate *m/z* ratios for modified peptide sequences were calculated for variations that included carbamidomethylated cysteine (that is, unconverted) in the SMARTag sequence, formylglycine in the SMARTag sequence (that is, unreacted), HIPS-azide-modified glycine in the SMARTag sequence and tri-GalNAc-modified in the SMARTag sequence. An additional

modification for the GalNAc-modified sequences was also calculated to account for possible gas-phase fragmentation of the tri-GalNAc moiety (modification on glycine = C44H52N8O7). The Xcalibur QualBrowser software suite was used to calculate areas under the curve for *m/z* values of appropriate charge states for each peptide species for each conjugate using the ICIS algorithm. Areas for each sequence and modification type were summed and ratios of total signal were generated, as shown in Extended Data Figs. 6 and 7. The Interactive Peptide Spectral Annotator (IPSA) was used to aid with spectral annotation[53].

In vivo pharmacokinetic study. Mouse experiments were performed at Stanford University in compliance with ethical regulations approved by the Administrative Panel on Laboratory Animal Care (APLAC) under protocol number 31511. Mice were housed in the Stanford Veterinary Service Center (VSC) facility where they were kept at a constant temperature and humidity, exposed to 12-h cycles of alternating light and dark and continuously provided with water and standard rodent food. Female BALB/c mice (6–8 weeks old; Jackson Laboratory) were injected intraperitoneally with 5 mg kg^{-1} Ctx or Ctx conjugates. Blood was collected at 6, 24, 48 and 72 h via tail bleed and plasma was separated. Plasma (2 µl) was subjected to SDS–PAGE (4–12% Bis-Tris gels) and transferred onto a nitrocellulose membrane for detection of human antibody presence (800CW goat anti-human; LI-COR). Organs were harvested at 72 h, lysed with RIPA buffer supplemented with protease inhibitor and 0.1% benzonase. Protein concentration was determined by BCA and 50 µg of total protein was loaded onto 4–12% Bis-Tris gels, subjected to SDS–PAGE and transferred onto a nitrocellulose membrane for detection of human antibody presence (800CW goat anti-human; LI-COR).

In vivo hepatic toxicity study. Female BALB/c mice (6–8 weeks old; Jackson Laboratory) were intraperitoneally injected with 5 mg kg^{-1} of Ctx or Ctx-$(tri\text{-}GalNAc)_{10}$ every 2 d or 5 mg kg^{-1} Ctx or Ctx-C-term-$(tri\text{-}GalNAc)_1$ every 4 d for a week. Blood and liver were harvested on day 8. Blood was submitted to the Stanford VSC Diagnostics Lab for liver biochemistry testing (ALP, AST, ALP, bilirubin). Livers were fixed with 10% neutral buffered formalin and submitted to the Stanford Animal Histology Services (AHS) for histopathology analysis.

Statistical analyses. All statistical analyses were performed using GraphPad Prism 8. Two-tailed tests were used for all *t*-tests.

Figure illustrations. Illustrations of the cell membrane, organelles and organs in Figs. 1a,b,e and 2a were modified from Servier Medical Art, licensed under a Creative Common Attribution 3.0 Generic License https://smart.servier.com.

Reporting Summary. Further information on research design is available in the Nature Research Reporting Summary linked to this article.

Data availability

All data that supported the findings of this manuscript are included and are also available from the corresponding author upon request. The flow cytometry gating strategy is provided in the Supplementary Information. Source data are provided with this paper.

References

51. Rose, C. M. et al. A calibration routine for efficient ETD in large-scale proteomics. *J. Am. Soc. Mass. Spectrom.* **26**, 1848–1857 (2015).
52. Solntsev, S. K., Shortreed, M. R., Frey, B. L. & Smith, L. M. Enhanced global post-translational modification discovery with MetaMorpheus. *J. Proteome Res.* **17**, 1844–1851 (2018).
53. Brademan, D. R., Riley, N. M., Kwiecien, N. W. & Coon, J. J. Interactive peptide spectral annotator: a versatile web-based tool for proteomic applications. *Mol. Cell. Proteom.* **18**, S193–S201 (2019).

Acknowledgements

We thank M.A. Gray (Stanford University) for providing FGE-expressing Expi293 cells and her expertise in site-specific antibody conjugations. We thank M.A. Gray and J. Tanzo (Stanford University) for providing HIPS-azide and the Cochran laboratory for providing PIP–Fc (mIgG2a). We thank S. Pitteri and K. Lau (Canary Center at Stanford) for performing MALDI–TOF–MS characterization and analysis. We thank J. Vilches-Moure (Stanford University) and the Stanford AHS for performing liver histopathology. We thank the Stanford VSC Diagnostics Lab for liver biochemistry testing. We thank K. Pedram (Stanford University) for helpful discussions. We thank T. McLaughlin and Stanford University Mass Spectrometry for HRMS characterization. This work was supported, in part, by a National Institutes of Health grant R01GM058867 (C.R.B.) and a St. Baldrick's/Stand Up 2 Cancer Pediatric Dream Team Translational Cancer Research Grant (J.R.C.). Researchers were supported by National Science Foundation Graduate Research Fellowship (G.A. and C.L.M.), a National Institute of General Medical Sciences F32 Postdoctoral Fellowship (S.M.B.) and National Institutes of Health grant K00CA21245403 (N.M.R.).

Author contributions

G.A., S.M.B. and C.R.B. conceived the project. G.A., S.M.B., C.L.M. and N.M.R. carried out the experiments and interpreted data. G.A. and C.L.M. synthesized and purified LYTAC conjugates. G.A., C.L.M. and S.M.B. carried out and analyzed in vitro degradation experiments. N.M.R. characterized and analyzed LYTAC conjugates by MS. G.A., S.M.B. and C.L.M. conceived and performed experiments to analyze the pharmacokinetic profiles and toxicity of LYTACs in vivo. J.R.C. oversaw and provided insights and materials such as PIP–Fc. G.A. and C.R.B. wrote the manuscript with input from all authors. C.R.B. provided supervision.

Competing interests

Stanford University has filed patent applications relating to lysosome-targeting chimeras, which are licensed to Lycia Therapeutics, listing G.A., S.M.B. and C.R.B. as co-inventors. G.A., S.M.B., C.L.M., J.R.C. and C.R.B. are co-inventors on a patent application relating to PIP-LYTACs filed by Stanford University (docket number STAN-1780PRV). C.R.B. is a co-founder and Scientific Advisory Board member of Lycia Therapeutics, Palleon Pharmaceuticals, Enable Bioscience, Redwood Biosciences (a subsidiary of Catalent) and InterVenn Biosciences and a member of the Board of Directors of Eli Lilly & Company. J.R.C. is a founder of xCella Biosciences and Combangio Inc. and co-founder and director of Trapeze Therapeutics.

Additional information

Extended data is available for this paper at https://doi.org/10.1038/s41589-021-00770-1.

Supplementary information The online version contains supplementary material available at https://doi.org/10.1038/s41589-021-00770-1.

Correspondence and requests for materials should be addressed to C.R.B.

Peer review information *Nature Chemical Biology* thanks Padma Devarajan, Lindy Durrant and Joshiawa Paulk for their contribution to the peer review of this work.

Reprints and permissions information is available at www.nature.com/reprints.

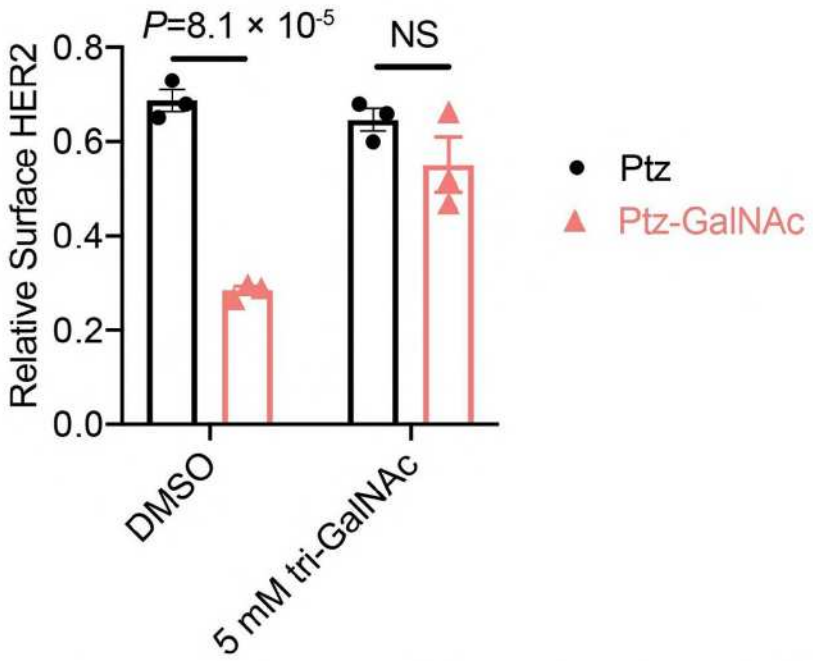

Extended Data Fig. 1 | HER2 degradation by Ptz-GalNAc is inhibited by exogenous tri-GalNAc ligand. Degradation of HER2 in HEPG2 cells determined by live-cell flow cytometry following co-treatment with DMSO or 5 mM of exogenous tri-GalNAc ligand (**10**) and 10 nM Ptz conjugates for 48 h. Data are the mean of three independent experiments ± SEM. *P* values were determined by unpaired two-tailed *t*-tests.

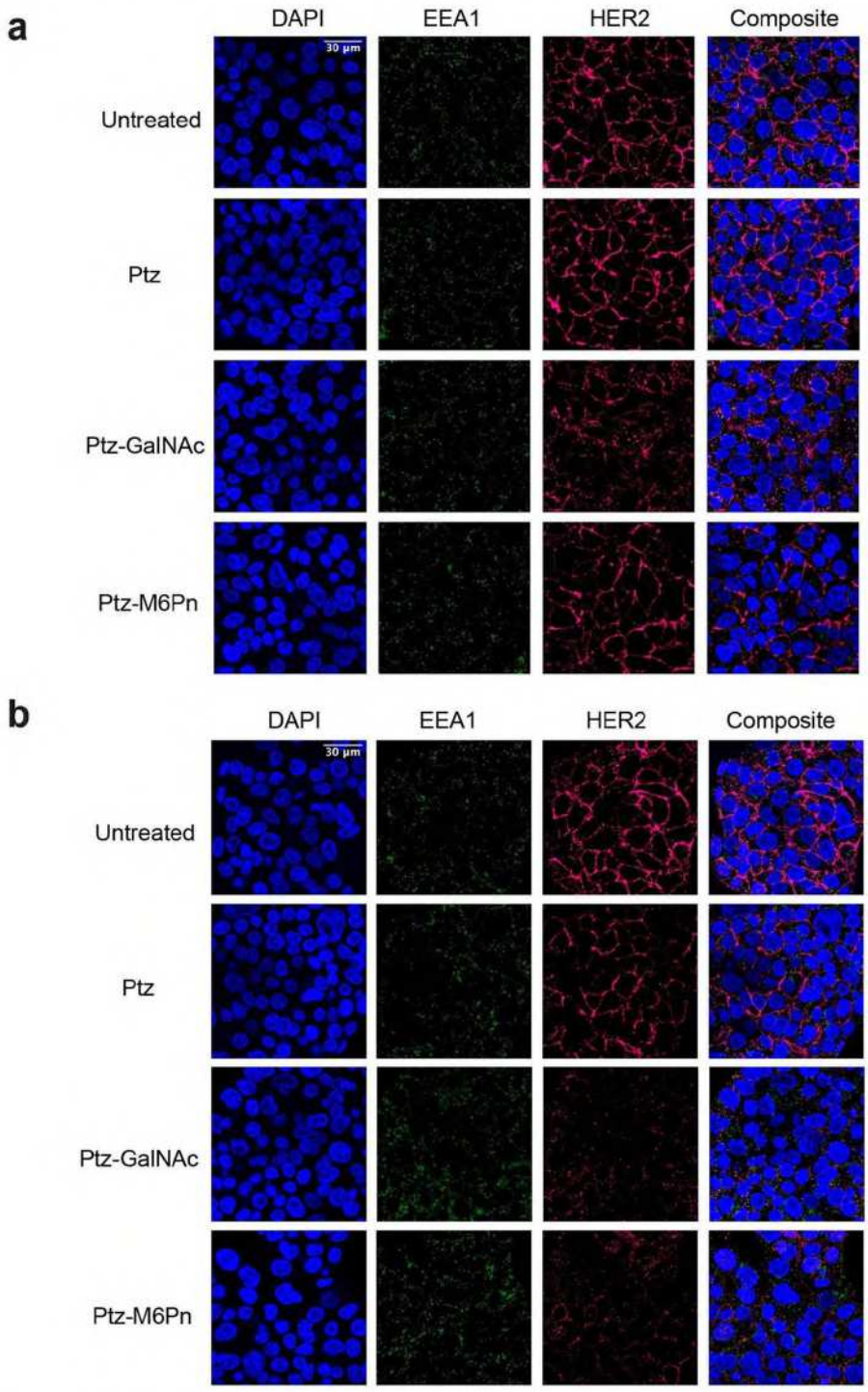

Extended Data Fig. 2 | Ptz-GalNAc internalizes membrane HER2 within 2 hours. a, Visualization of HER2 in HEPG2 cells by confocal microscopy after 10 nM pertuzumab conjugate treatments for 2 h. EEA1 is included as an early endosomal marker. **b**, Visualization of HER2 in HEPG2 cells by confocal microscopy after 10 nM pertuzumab conjugate treatments for 48 h. EEA1 is included as an early endosomal marker. Images are representative of two independent experiments. Scale bar, 30 µm.

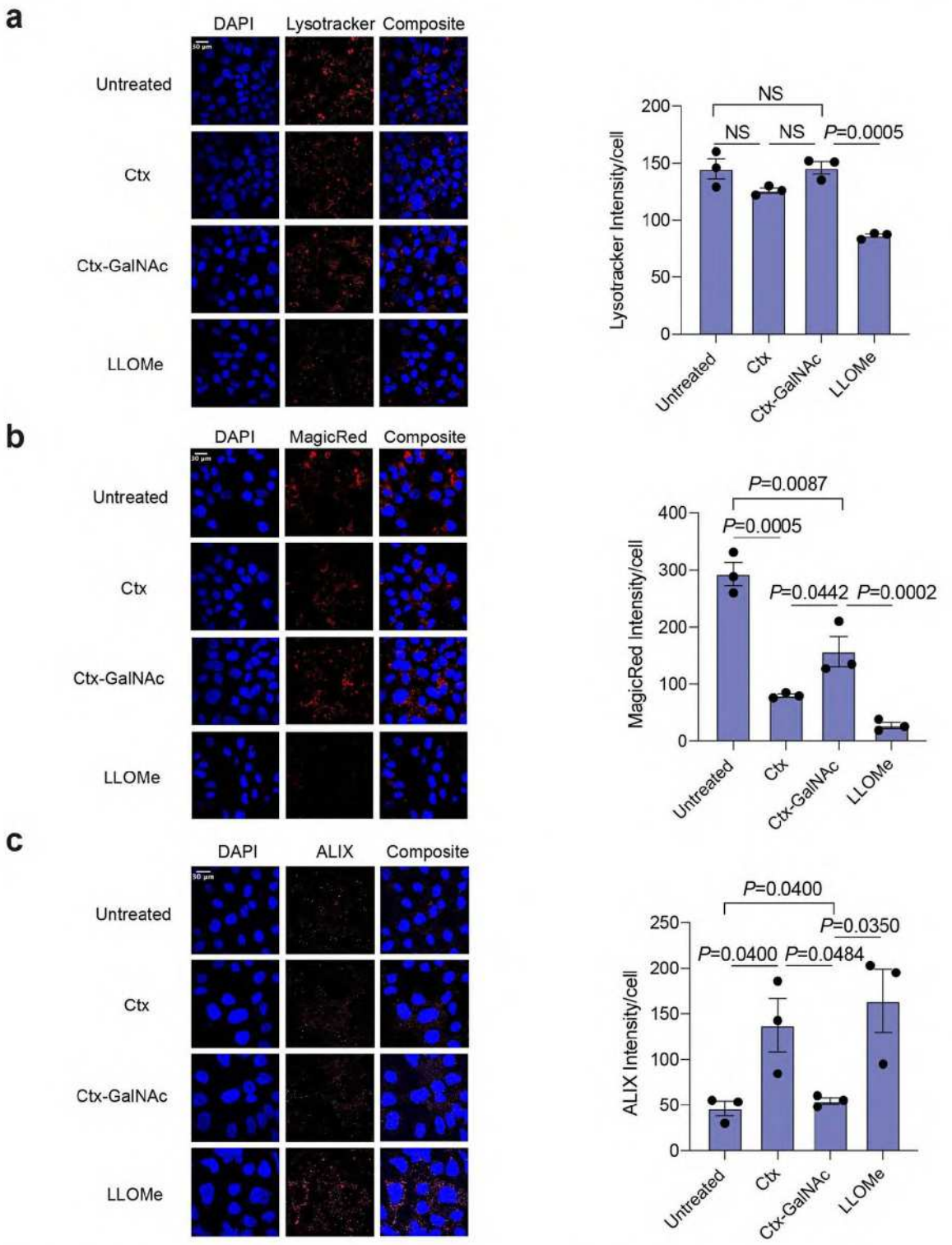

Extended Data Fig. 3 | Ctx-GalNAcs show similar lysosomal health as untreated cells. a, Visualization and quantification of Lysotracker by confocal microscopy imaging of HEP3B cells treated with 10 nM cetuximab conjugates for 48 h or 1 mM LLOMe for 1 hour. **b**, Visualization and quantification of Cathepsin B activity using Magic Red in HEP3B cells treated with 10 nM cetuximab conjugates for 48 h or 1 mM LLOMe for 1 h. **c**, Visualization and quantification of ALIX in HEP3B cells treated with 10 nM cetuximab conjugates for 48 h or 1 mM LLOMe for 1 h. Scale bar, 30 μm. Values are the average ± SEM of three separate images from confocal microscopy. *P* values were determined by unpaired two-tailed *t*-tests.

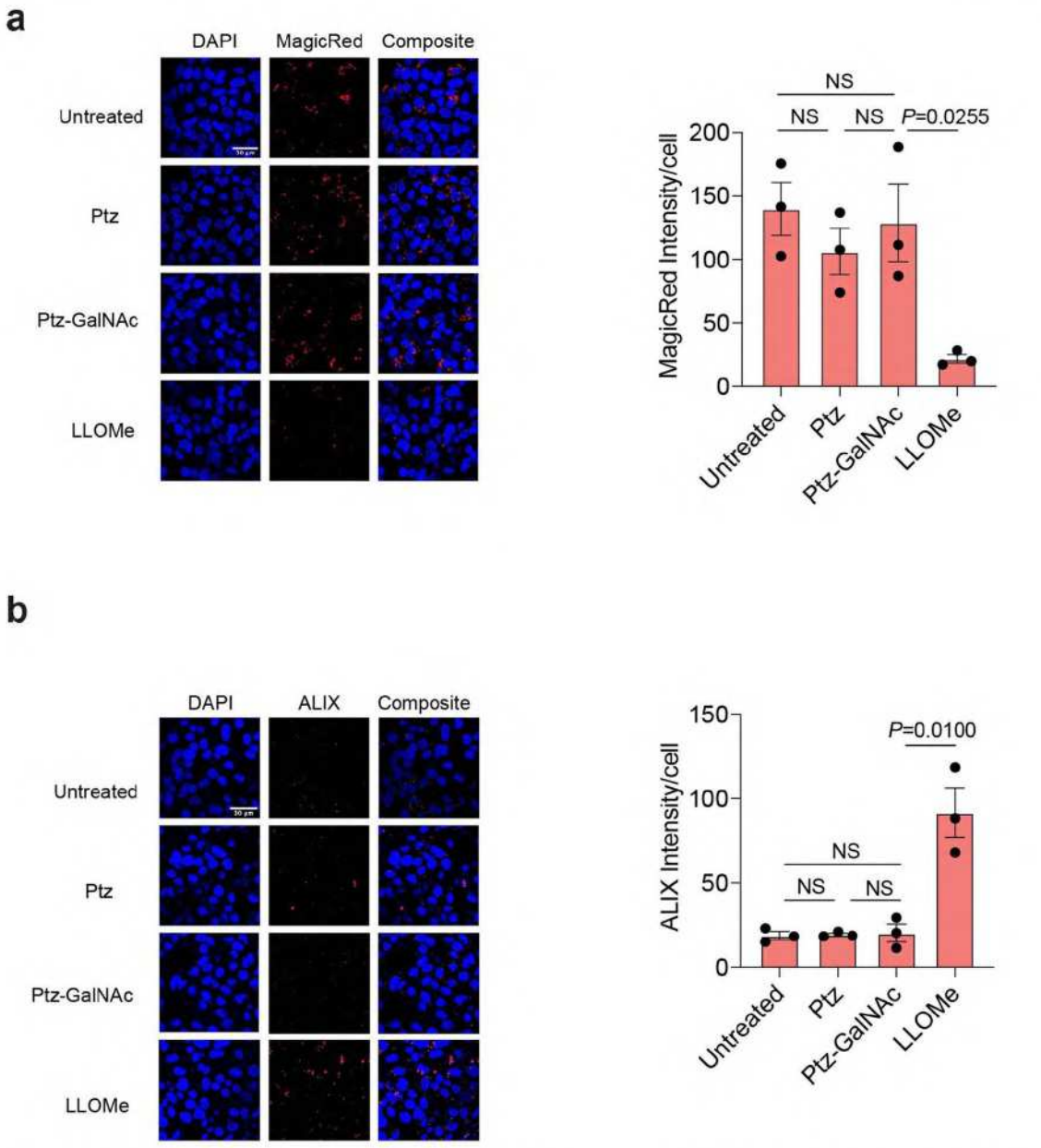

Extended Data Fig. 4 | Ptz-GalNAcs do not affect lysosomal health. a. Visualization and quantification of Cathepsin B activity using Magic Red in HEPG2 cells treated with 100 nM Ptz conjugates for 48 h or 1 mM LLOMe for 1 h. **b**, Visualization and quantification of ALIX in HEPG2 cells treated with 100 nM Ptz conjugates for 48 h or 1 mM LLOMe for 1 h. Scale bar, 30 μm. Values are the average ± SEM of three separate images from confocal microscopy. *P* values were determined by unpaired two-tailed *t*-tests.

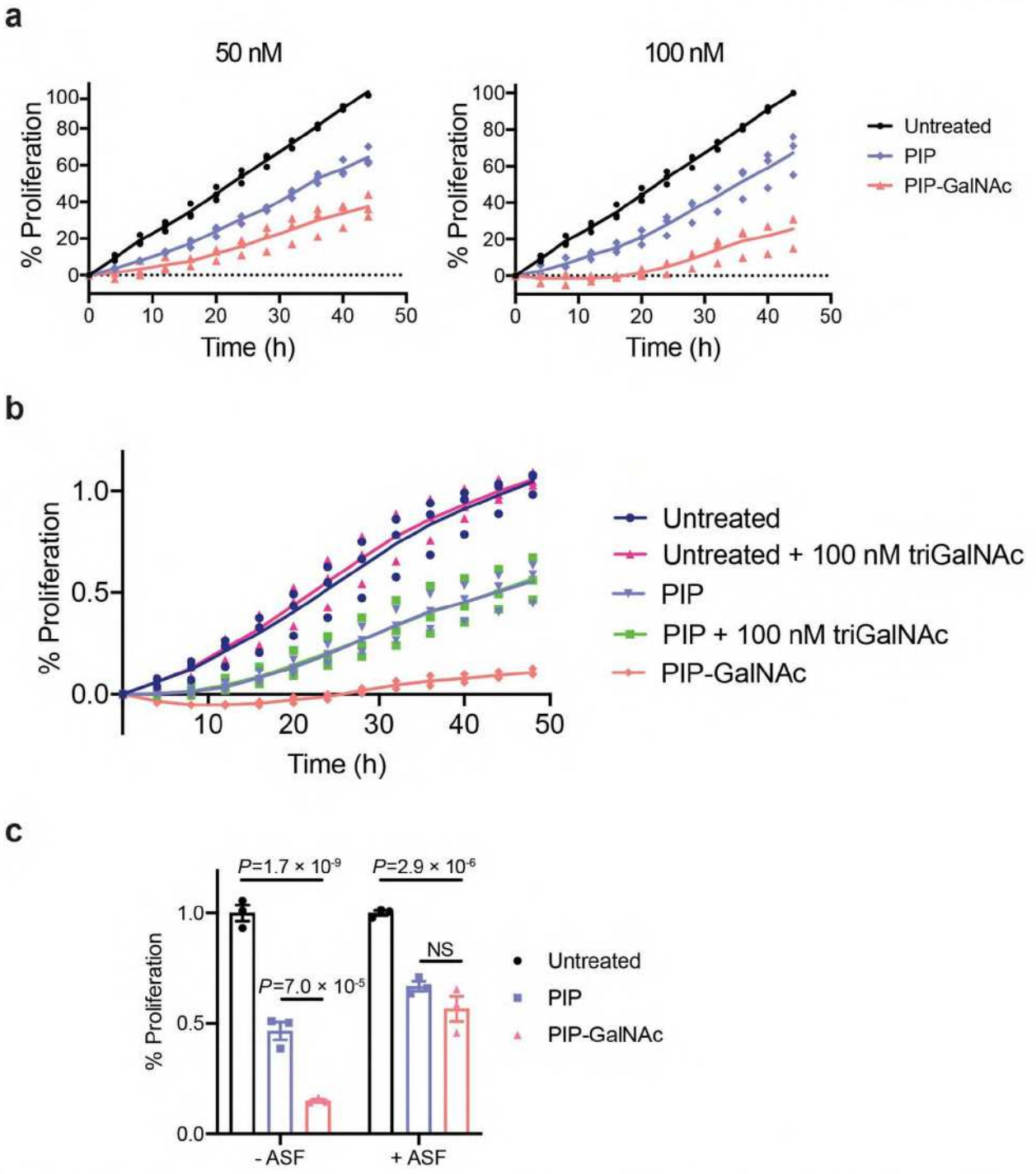

Extended Data Fig. 5 | PIP-GalNAc conjugate and ASGPR are required for enhanced anti-proliferative effect. a, Time-course percent proliferation of HEPG2 cells during 44 h of treatment with 50 or 100 nM PIP or PIP-GalNAc. **b**, Percent proliferation of HEPG2 cells over 48 h with 100 nM exogenous tri-GalNAc, 100 nM PIP, 100 nM PIP + 100 nM exogenous tri-GalNAc, or 100 nM PIP-GalNAc conjugate. **c**, Percent proliferation of HEPG2 cells at 48 h following co-incubation of 100 nM of PIP or PIP-GalNAc with or without 10 mg/ml asialofetuin (ASF). Data are three independent experiments in **b**. For **c**, values are the average of three independent experiments ± SEM. Ordinary two-way ANOVA with adjusted *P* values shown from Tukey's multiple comparisons.

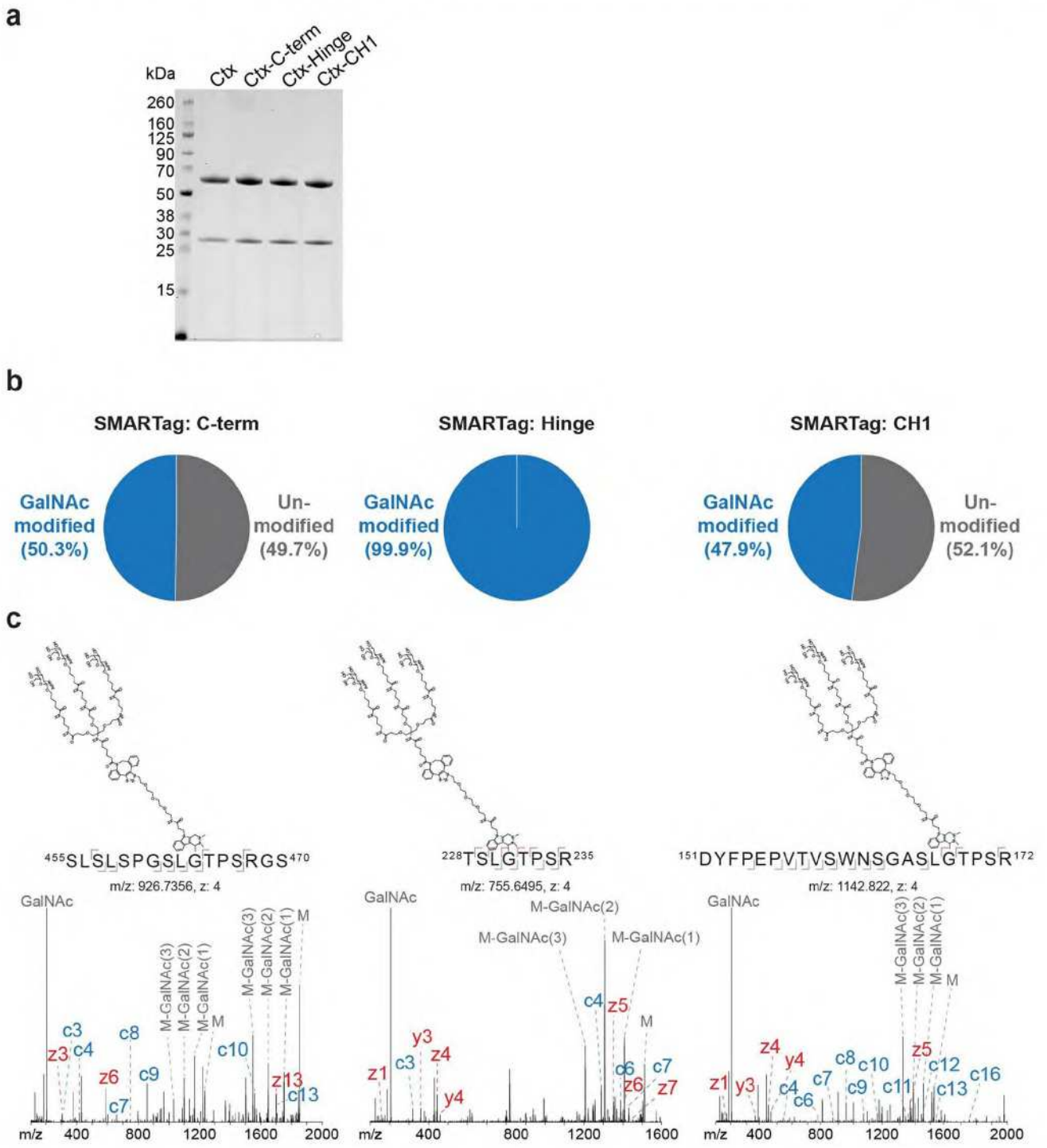

Extended Data Fig. 6 | Analysis of site-specific conjugation of the tri-GalNAc ligand to three different locations on cetuximab. a, Reducing SDS-PAGE gel of Ctx and Ctx with aldehyde tag at C-terminus, Hinge, and CH1 Heavy chain. **b**, The proportion of signal seen between tri-GalNAc-modified (blue) peptides and peptides from the sequence that should have harbored the tri-GalNAc ligand but were seen unmodified (gray). Due to the dimer nature of the antibody, 50% of signal as modified indicates one site of modification per antibody molecule while 100% of signal as modified shows two ligands per antibody molecule. **c**, EThcD spectra of peptides showing site-specific localization of the tri-GalNAc ligand in the SMARTag sequence. Note, 'M' represents the intact mass of the modified peptide, 'GalNAc' shows the oxonium ion of a GalNAc residue, and the 'M-GalNAc(x)' annotations show the intact mass minus x number of GalNAc moieties. **a** is a representative data from two independent experiments.

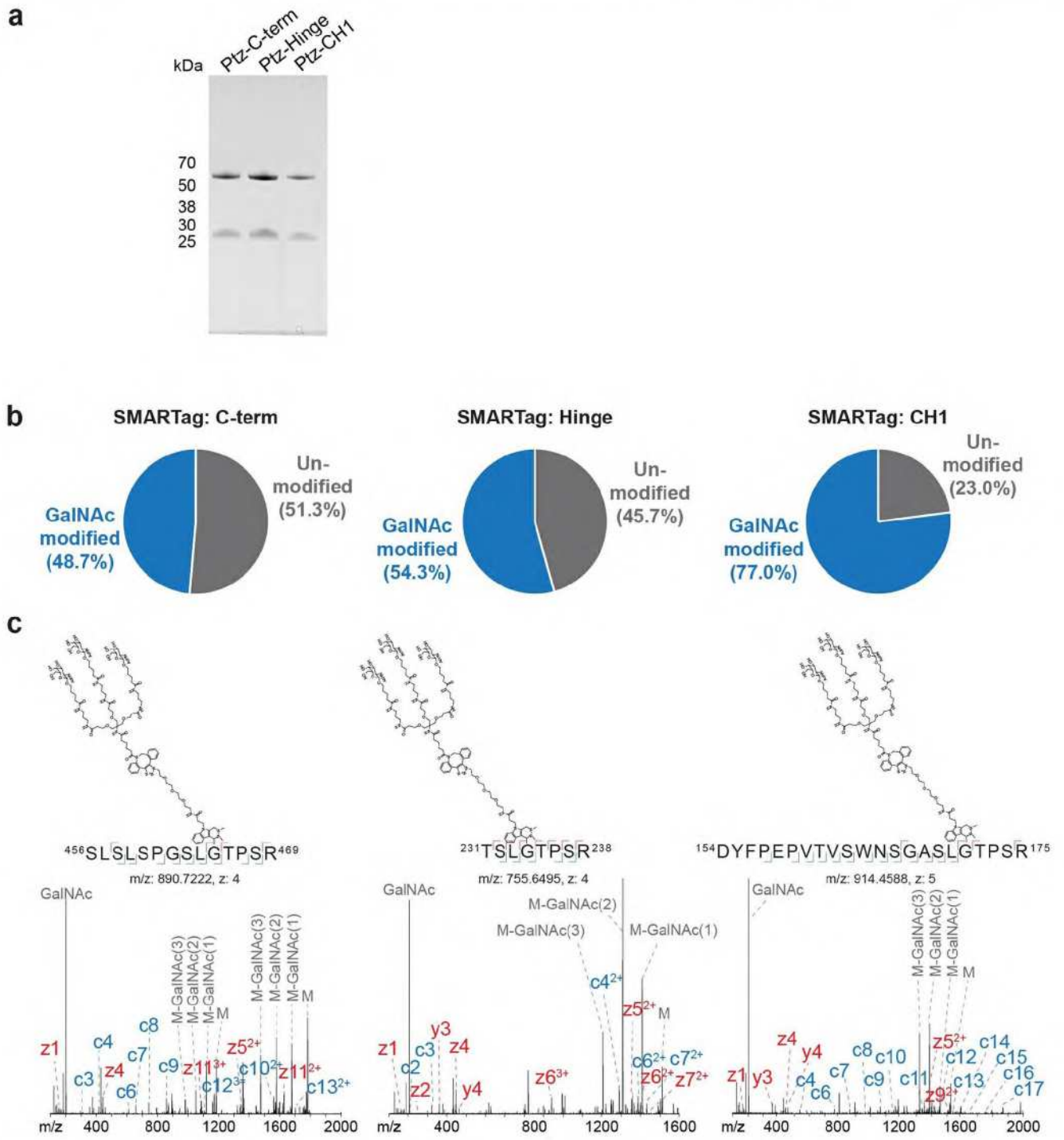

Extended Data Fig. 7 | Analysis of site-specific conjugation of the tri-GalNAc ligand to three different locations on pertuzumab. a, Reducing SDS-PAGE gel of Ptz with aldehyde tag at C-terminus, Hinge, and CH1 Heavy chain.**b**, The proportion of signal seen between tri-GalNAc-modified (blue) peptides and peptides from the sequence that should have harbored the tri-GalNAc ligand but were seen unmodified (gray). Due to the dimer nature of the antibody, 50% of signal as modified indicates one site of modification per antibody molecule while 100% of signal as modified shows two ligands per antibody molecule. **c**, EThcD spectra of peptides showing site-specific localization of the tri-GalNAc ligand in the SMARTag sequence. Note, 'M' represents the intact mass of the modified peptide, 'GalNAc' shows the oxonium ion of a GalNAc residue, and the 'M-GalNAc(x)' annotations show the intact mass minus x number of GalNAc moieties. **a** is a representative data from two independent experiments.

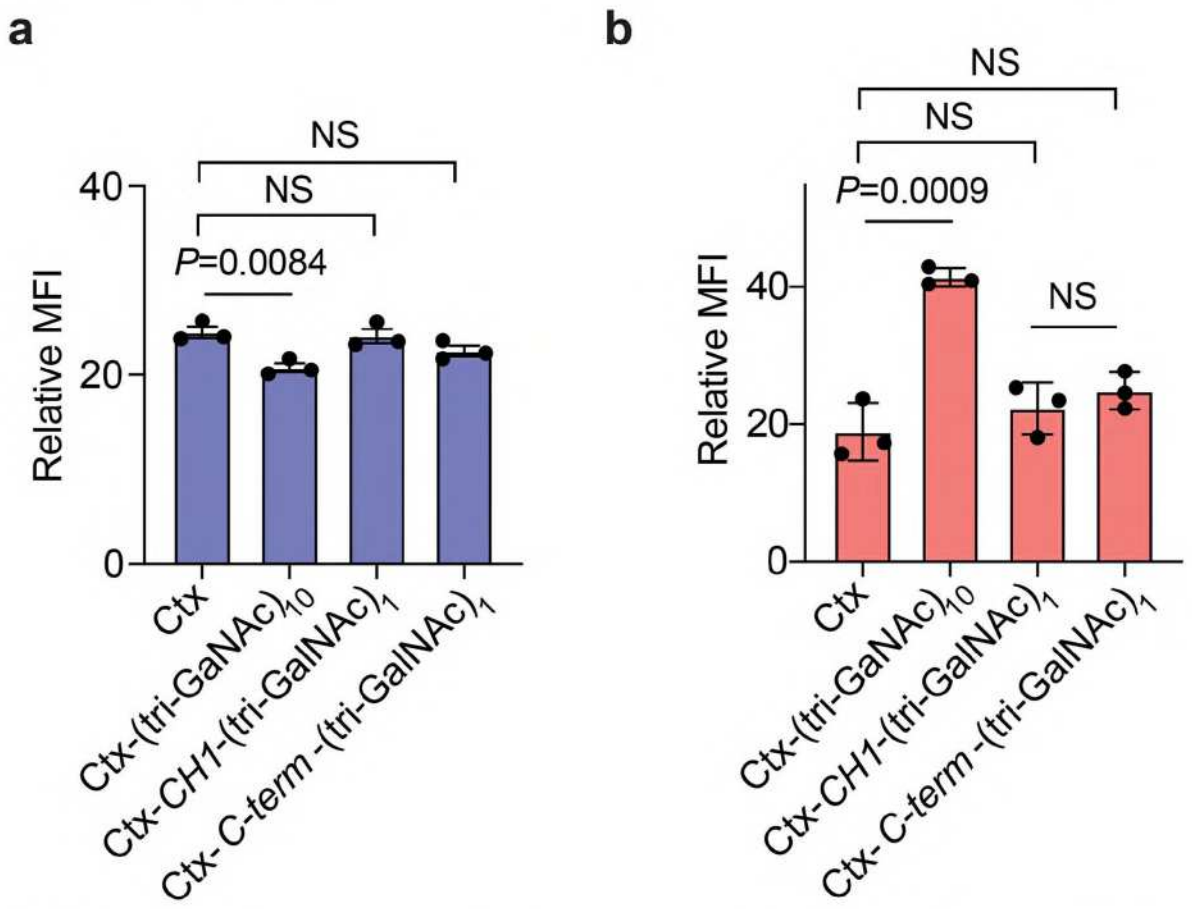

Extended Data Fig. 8 | Non-specific Ctx-GalNAc conjugates show enhanced uptake *in vitro* compared to site-specific Ctx conjugates. a, Binding of Ctx conjugates in HEPG2 cells measured by live-cell flow cytometry following 1 h incubation on ice. **b**, Mean fluorescence intensity (MFI) relative to the control (human IgG-647 only) for HEPG2 cells incubated at 37 °C for 1 h with 50 nM human IgG-647 and 25 nM Ctx, Ctx-(tri-GalNAc)$_{10}$, Ctx-*C-term*-(tri-GalNAc)$_1$, or Ctx-*CH1*-(tri-GalNAc)$_1$. MFI was determined by live cell flow cytometry. Values are the average ± SEM of three independent experiments. *P* values were determined by unpaired two-tailed *t*-tests.

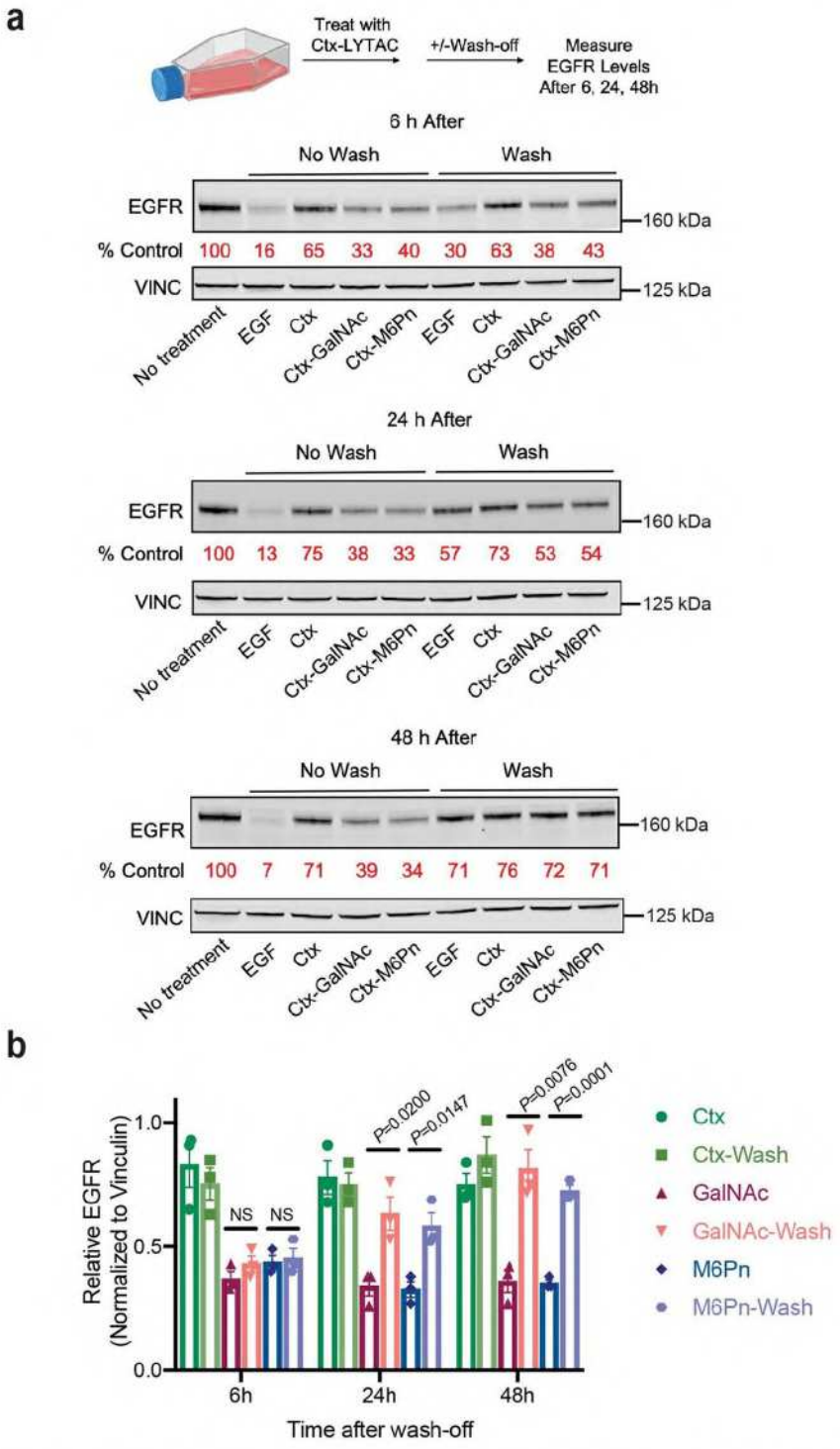

Extended Data Fig. 9 | Durability of LYTAC-mediated degradation in HEP3B cells. a, HEP3B cells were treated with 10 nM Ctx conjugates, then washed with PBS 3 times, and were incubated in fresh media for 6, 24, 48 h. EGFR levels were measured by western blot. 100 ng/ml of EGF was included as a control. **b**, Quantification of EGFR levels with and without wash-off following treatment with Ctx conjugates. Values are the average of three independent experiments ± SEM. *P* values were determined by unpaired two-tailed *t*-tests.

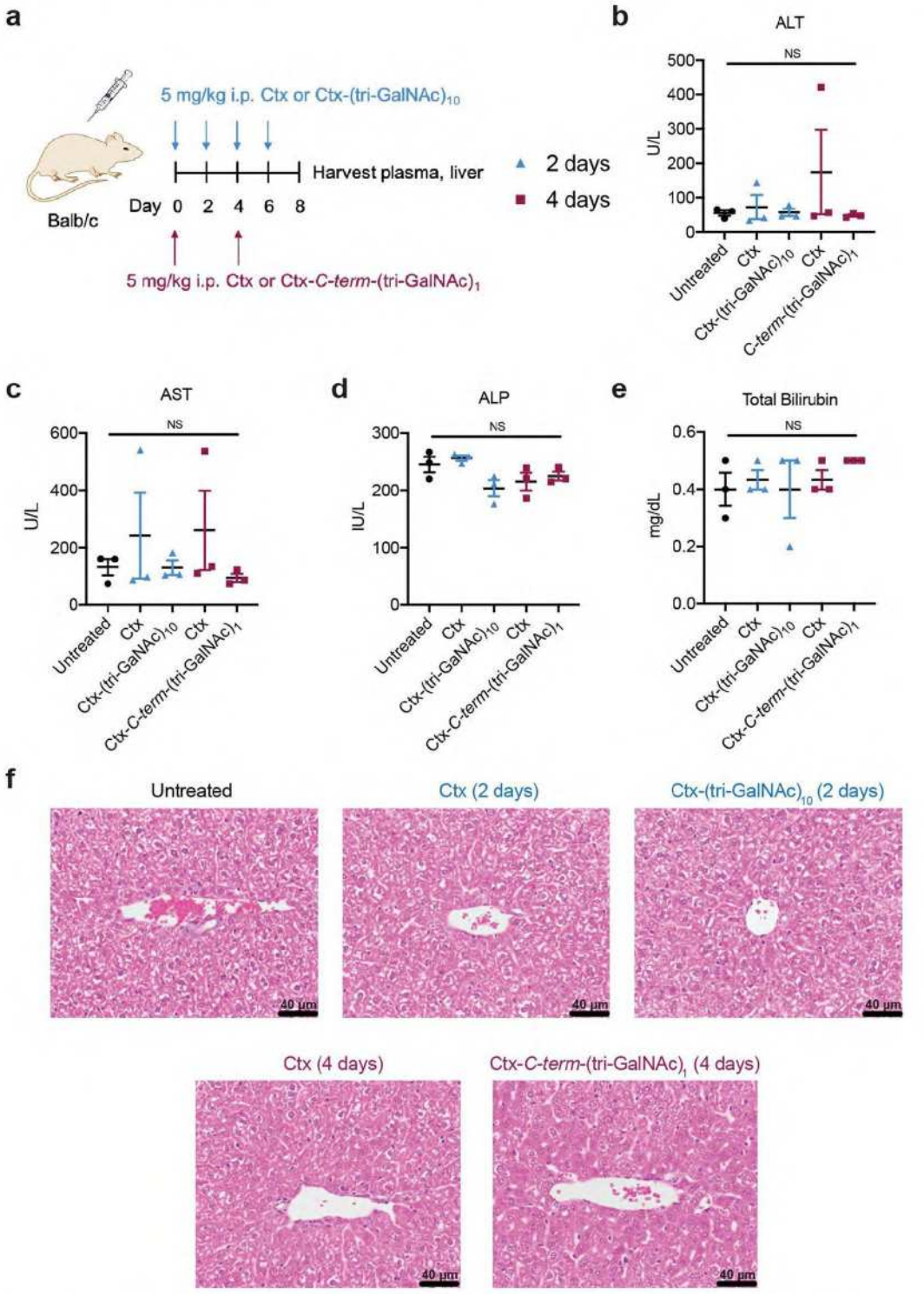

Extended Data Fig. 10 | GalNAc-LYTACs do not cause hepatic toxicity in mice. a, Balb/c mice were intraperitoneally injected with 5 mg/kg of Ctx or Ctx-$(tri\text{-}GalNAc)_{10}$ every 2 days or 5 mg/kg Ctx or Ctx-*C-term*-$(tri\text{-}GalNAc)_1$ every 4 days for a week. Plasma and liver were harvested on day 8, and levels of liver enzymes (**b** – alanine transaminase (ALT); **c** – aspartate transaminase (AST), **d**, alkaline phosphatase (ALP), **e** – total bilirubin) from plasma were measured. Values in **b-e** are the average of three independent mice ± SEM and were evaluated using Ordinary one-way ANOVA with Tukey's multiple comparisons. **f**, Representative H&E staining of the liver from three independent experiments. Scale bar, 40 µm.

nature research

Corresponding author(s): Carolyn R. Bertozzi

Last updated by author(s): Jan 27, 2021

Reporting Summary

Nature Research wishes to improve the reproducibility of the work that we publish. This form provides structure for consistency and transparency in reporting. For further information on Nature Research policies, see our Editorial Policies and the Editorial Policy Checklist.

Please do not complete any field with "not applicable" or n/a. Refer to the help text for what text to use if an item is not relevant to your study.
For final submission: please carefully check your responses for accuracy; you will not be able to make changes later.

Statistics

For all statistical analyses, confirm that the following items are present in the figure legend, table legend, main text, or Methods section.

n/a Confirmed

- [ ] [x] The exact sample size (*n*) for each experimental group/condition, given as a discrete number and unit of measurement
- [ ] [x] A statement on whether measurements were taken from distinct samples or whether the same sample was measured repeatedly
- [ ] [x] The statistical test(s) used AND whether they are one- or two-sided
  Only common tests should be described solely by name; describe more complex techniques in the Methods section.
- [x] [ ] A description of all covariates tested
- [ ] [x] A description of any assumptions or corrections, such as tests of normality and adjustment for multiple comparisons
- [ ] [x] A full description of the statistical parameters including central tendency (e.g. means) or other basic estimates (e.g. regression coefficient) AND variation (e.g. standard deviation) or associated estimates of uncertainty (e.g. confidence intervals)
- [ ] [x] For null hypothesis testing, the test statistic (e.g. *F*, *t*, *r*) with confidence intervals, effect sizes, degrees of freedom and *P* value noted
  Give P values as exact values whenever suitable.
- [x] [ ] For Bayesian analysis, information on the choice of priors and Markov chain Monte Carlo settings
- [x] [ ] For hierarchical and complex designs, identification of the appropriate level for tests and full reporting of outcomes
- [x] [ ] Estimates of effect sizes (e.g. Cohen's *d*, Pearson's *r*), indicating how they were calculated

Our web collection on statistics for biologists contains articles on many of the points above.

Software and code

Policy information about availability of computer code

Data collection	A BD Accuri C6 Plus flow cytometer, LSRII, and Quanteon flow cytometer were used for flow cytometry data acquisition. Image Studio Software (v 5.2) was used for gel scanning. A SpectraMax i3x plate reader was used for absorbance detected in a 96 well plates for BCA protein quantification. The Nanodrop 2000 Spectrophotometer (Thermo Fischer) was used to characterize proteins. An IncuCyte S3 Live Cell Analysis system (Sartorious) equipped with a 10x objective lens in phase contrast was used to monitor live cells confluence over time. An Orbitrap Fusion Tribrid mass spectrometer was used to analyze protein tryptic digest masses, and AB SCIEX TOF/TOF and 5800 CovalX High Mass Detector were used to analyze full protein MALDI MS. A Bruker MicroTOF-Q II was used to analyze peptide masses, and HRMS of small molecules were analyzed on a Thermo Exactive Orbitrap Mass Spectrometer. A Nikon A1R confocal miscrope using Plan Fluor 60x oil immersion 1.30-numerical aperture objective was used for confocal microscopy imaging with 405-nm violet laser, 488-nm blue laser, 561-nm green laser, and 639-nm red laser. For site-specific antibody characterization, MetaMorpheus was used to search against fasta sequences and Xcalibur 3.1 QualBrowser software was used to calculate areas under the curve for m/z values of appropriate charge states for each peptide species.
Data analysis	MestReNova (v12.0.3) was used for all chemical NMR analysis. GraphPad Prism (v6) were used for data analysis and curve-fitting. FlowJo (v10.0) was used for flow cytometry data analysis. Incucyte S3 Software (v2018B) was used for cell-proliferation analysis.

For manuscripts utilizing custom algorithms or software that are central to the research but not yet described in published literature, software must be made available to editors and reviewers. We strongly encourage code deposition in a community repository (e.g. GitHub). See the Nature Research guidelines for submitting code & software for further information.

Data

Policy information about availability of data

All manuscripts must include a data availability statement. This statement should provide the following information, where applicable:

- Accession codes, unique identifiers, or web links for publicly available datasets
- A list of figures that have associated raw data
- A description of any restrictions on data availability

All data that supported the findings of this study are available from the corresponding author upon request.

Field-specific reporting

Please select the one below that is the best fit for your research. If you are not sure, read the appropriate sections before making your selection.

☒ Life sciences ☐ Behavioural & social sciences ☐ Ecological, evolutionary & environmental sciences

For a reference copy of the document with all sections, see nature.com/documents/nr-reporting-summary-flat.pdf

Life sciences study design

All studies must disclose on these points even when the disclosure is negative.

Sample size	No sample size calculation was performed. Typically three experimental replicates were performed in order to show standard error of mean (SEM) for experiments. Sample size choice was based on our experience with variability in experiments and ability to observe meaningful differences between treatments. In vitro experiments such as western blot, flow cytometry, and proliferation showed low variability. The sample size for mouse pharmacokinetic and toxicity experiments was chosen based on our previous experience with variability among different mouse groups.
Data exclusions	There were no data exclusions. For integrin degradation analysis, a subet of integrins could not be analyzed due to lack of specific commerical antibodies or lack of surface expression of the integrins.
Replication	All biological data were confirmed with multiple replicates as noted in the methods and figure legends. For site specific MS analysis and MALDI-MS analysis, the average of at least 5 spectra were used.
Randomization	The order of analysis for flow cytometry experiment was randomized. No other randomization was used as internal controls were used for quantitative comparisons.
Blinding	No blinding was performed in vitro and in vivo experiments in order to make comparisons between specific treatments. MS sample processing and MS analysis were blinded from one another.

Reporting for specific materials, systems and methods

We require information from authors about some types of materials, experimental systems and methods used in many studies. Here, indicate whether each material, system or method listed is relevant to your study. If you are not sure if a list item applies to your research, read the appropriate section before selecting a response.

Materials & experimental systems

n/a	Involved in the study
☐	☒ Antibodies
☐	☒ Eukaryotic cell lines
☒	☐ Palaeontology and archaeology
☐	☒ Animals and other organisms
☒	☐ Human research participants
☒	☐ Clinical data
☒	☐ Dual use research of concern

Methods

n/a	Involved in the study
☒	☐ ChIP-seq
☐	☒ Flow cytometry
☒	☐ MRI-based neuroimaging

Antibodies

Antibodies used	Rabbit IgG Bio X Cell (BE0095) Functional Goat Anti-Rabbit IgG Jackson ImmunoResearch (111-005-144) Functional Rabbit-anti-EGFR CST (D38B1) WB, 1:1000 Mouse anti-Vinculin Bio-Rad (V284) WB, 1:1000 Mouse-anti-EGFR Invitrogen (MA513319) Flow Cytometry, 10 µg/ml

Cetuximab Eli Lilly F
Phospho-EGF Receptor (Tyr1068) CST (2234S) 1:1000
Phospho-Akt (Ser473) CST (9271S) 1:1000
Phospho-p44/42 MAPK (Erk1/2) (Thr202/Tyr204) CST (4376S) 1:1000
ALIX BioLegend (634502) IF, 1:500
Pertuzumab Selleck Chemicals (A2008) Functional
HER2/ErbB2 CST (2242S) WB, 1:1000
HER2 CST (2165S) IF 1:100
Alpha V Beta 3 integrin R&D (MAB3050) 1 µg/100 µl
Alpha V Beta 5 integrin R&D (MAB2528) 1 µg/100 µl
IRDye 800CW Goat-anti-rabbit IgG (H+L) LI-COR (926-32211) WB, 1:10000
IRDye 800CW Goat-anti-mouse IgG (H+L) LI-COR WB, 1:10000
IRDye 800CW Goat-anti-human IgG (H+L) LI-COR WB, 1:1000

Validation

All antibodies were used for applications validated by antibody suppliers per quality assurance provided by each supplier.

Rabbit IgG Bio X Cell (BE0095): validated from manufacturer's website and citations therein.

Goat Anti-Rabbit IgG Jackson ImmunoResearch (111-005-144): validated from manufacturer's website and citations therein.

Rabbit-anti-EGFR CST (D38B1): Validated from manufacturer's website for western blot and citations therein, validation included EGFR knock-out.

Mouse anti-Vinculin Bio-Rad (V284) : Validated from manufacturer's website for western blotand citations therein.

Mouse-anti-EGFR Invitrogen (MA513319): Validated from manufacturer's website for flow cytometry and citations therein.

Goat anti-mouse IgG-Alexa Fluor 647 Jackson ImmunoResearch (115-605-071): Validated from manufacturer's website for flow cytometry and citations therein.

Cetuximab (anti-EGFR) is an United States FDA-approved antibody against EGFR.

Phospho-EGF Receptor (Tyr1068) CST (2234S): Validated from manufacturer's website and citations therein, validation included stimulation with EGF.

Phospho-Akt (Ser473) CST (9271S): Validated from manufacturer's website and citations therein, validation included stimulation with AKT activating ligands (i.e. PDGF) as well transfection with phospho-inactive AKT mutants.

Phospho-p44/42 MAPK (Erk1/2) (Thr202/Tyr204) CST (4376S): Validated from manufacturer's website and citations therein. Validation included comparison with p38 and protein levels in the presence and absence of MAPK activating ligands.

ALIX Biolegend (634502): Validated from manufacturer's website and citations therein.

Pertuzumab (anti-HER2) is an United States FDA-approved antibody against HER2.

HER2/ErbB2 CST (2242S): Validated from manufacturer's website and citations therein.

HER2 CST (2165S): Validated from manufacturer's website and citations therein.

Alpha V Beta 3 integrin R&D (MAB3050): Validated from manufacturer's website and citations therein.

Alpha V Beta 5 integrin R&D (MAB2528): Validated from manufacturer's website and citations therein.

Goat anti-Rabbit IgG 800CW (926-32211, LI-COR): Validated from manufacturer's website.

Goat anti-Human IgG 800CW (926-32232, LI-COR, 1:1000): Validated from manufacturer's website.

Goat anti-Mouse IgG 800CW (926-32210, LI-COR): Validated from manufacturer's website.

Eukaryotic cell lines

Policy information about cell lines

Cell line source(s)	HEPG2 and HEP3B cells were obtained from the American Tissue Culture Collection (ATCC). HUH7 cells were obtained from Japanese Collection of Research Bioresources Cell Bank (JCRB Cell Bank). HeLa-GFP cells were obtained from MyBioSource. FGE-expressing Expi293 cells, derived from Expi293 (Thermo Fischer), were generous gifts from M. Gray.
Authentication	Cell lines have not been subjected to additional authentication.
Mycoplasma contamination	All cell lines regularly tested negative for mycoplasma infection by the Lonza MycoAlert Mycoplasma Detection Assay.
Commonly misidentified lines (See ICLAC register)	No commonly misidentified cells were used in this study.

Animals and other organisms

Policy information about studies involving animals; ARRIVE guidelines recommended for reporting animal research

Laboratory animals	7-9 week old female Balb/c mice were used for pharmacokinetic study. Mice were housed in the animal care facility at Stanford where they were kept at a constant temperature and humidity and exposed to 12 h cycles of alternating light and dark. They were continuously provided water and standard rodent food.
Wild animals	No wild animals were involved in this study.
Field-collected samples	The study did not involve field-collected samples.
Ethics oversight	Mouse experiments were performed at Stanford University, and the mouse care was monitored by the Veterinary Service Center at Stanford University under APLAC protocol 31511.

Note that full information on the approval of the study protocol must also be provided in the manuscript.

Flow Cytometry

Plots

Confirm that:

☒ The axis labels state the marker and fluorochrome used (e.g. CD4-FITC).

☒ The axis scales are clearly visible. Include numbers along axes only for bottom left plot of group (a 'group' is an analysis of identical markers).

☒ All plots are contour plots with outliers or pseudocolor plots.

☒ A numerical value for number of cells or percentage (with statistics) is provided.

Methodology

Sample preparation	For HEPG2 uptake experiment, cells were incubated with indicated treatments for 1 hour and cells were washed with PBS three times, trypsinized, then transferred to a 96 well V-bottom plate. The cells were washed 3 times with PBS + 0.5% BSA + 5 mM EDTA, then incubated with Sytox Green for 15 minutes on ice prior to flow cytometry analysis. For cell-surface staining experiment, Acells were incubated with indicated treatments for indicated time. Cells were then washed with PBS 3 times, trypsinized for <5 minutes, and transferred to a 96-well V-bottom plate. The cells were washed 3 times with PBS + 0.5% BSA + 5 mM EDTA (FACS buffer) and incubated with primary antibody for 30 minutes on ice. The cells were washed 3 times with PBS + 0.5% BSA + 5 mM EDTA (FACS buffer) and incubated with secondary antibody for 30 minutes on ice. After washing 3 times with FACS buffer, cells were incubated with either Sytox Green or Sytox Blue for 15 minutes on ice.
Instrument	BD-Accuri C6 Plus, LSR II, Quanteon
Software	Data analysis was performed using the FlowJo v10.0.
Cell population abundance	N/A - cell sorting was not performed.
Gating strategy	Representative gating strategies are in the Supplementary Fig. 13. Debris was gated out by the FSC and SSC area, and single cells were gated on FSC-A and FSC-H, and live cells were gated (Sytox Green or Sytox Blue were used).

☒ Tick this box to confirm that a figure exemplifying the gating strategy is provided in the Supplementary Information.

nature portfolio

https://doi.org/10.1038/s41589-021-00770-1

Supplementary information

LYTACs that engage the asialoglycoprotein receptor for targeted protein degradation

In the format provided by the authors and unedited

Supplementary Materials for

LYTACs that engage the asialoglycoprotein receptor for targeted protein degradation

Green Ahn, Steven M. Banik, Caitlyn L. Miller, Nicholas M. Riley, Jennifer R. Cochran, Carolyn R. Bertozzi*

*All correspondence should be addressed to bertozzi@stanford.edu

This PDF file includes:

Supplementary Table 1. Antibody information and concentrations

Antibody	Source (#)	Usage, Dilution
Rabbit IgG	Bio X Cell (BE0095)	Functional (50 nM)
Goat Anti-Rabbit IgG	Jackson ImmunoResearch (111-005-144)	Functional (25 nM)
Rabbit-anti-EGFR	CST (D38B1)	WB, 1:1000
Mouse anti-Vinculin	Bio-Rad (V284)	WB, 1:1000
Mouse anti-EGFR	Invitrogen (MA513319)	Flow Cytometry, 10 µg/ml
Mouse anti-M6PR	Abcam (ab2733)	Flow Cytometry, 10 µg/ml
Rabbit anti-ASGR1	Proteintech (11739-1-AP)	WB, 1:1000, Flow Cytometry 10 µg/ml
Rabbit anti-ASGR2	Invitrogen (PA5-53249)	WB, 0.4 µg/ml
Goat anti-mouse IgG-Alexa Fluor 647	Jackson ImmunoResearch (115-605-071)	Flow cytometry, IF 1:375
Cetuximab	Eli Lilly	Functional (10nM-100nM)
Phospho-EGF Receptor (Tyr1068)	CST (2234S)	1:1000
Phospho-Akt (Ser473)	CST (9271S)	1:1000
Phospho-p44/42 MAPK (Erk1/2) (Thr202/Tyr204)	CST (4376S)	1:1000
ALIX	BioLegend (634502)	IF, 1:500
Pertuzumab	Selleck Chemicals (A2008)	Functional (10nM-100nM)
HER2/ErbB2	CST (2242S)	WB, 1:1000
HER2	CST (2165S)	IF 1:100
Alpha V Beta 3 integrin	R&D (MAB3050)	1 µg/100 µl
Alpha V Beta 5 integrin	R&D (MAB2528)	1 µg/100 µl
IRDye 800CW Goat-anti-rabbit IgG (H+L)	LI-COR (926-32211)	WB, 1:10000
IRDye 800CW Goat-anti-mouse IgG (H+L)	LI-COR (926-32210)	WB, 1:10000
IRDye 800CW Goat-anti-human IgG (H+L)	LI-COR (926-32232)	WB, 1:1000

Supplemental Figures

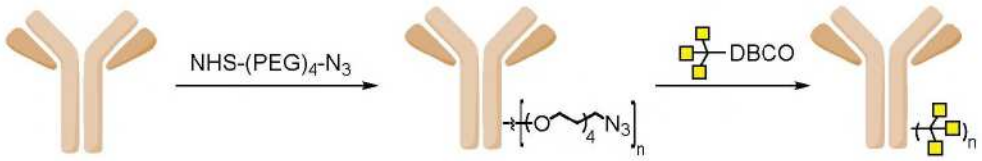

Supplementary Fig. 1. General conjugation strategy for GalNAc-LYTACs. Antibodies were non-specifically functionalized with NHS-$(PEG)_4$-N_3. Azide-labeled antibodies were then reacted with tri-GalNAc-DBCO via Cu-free strain-promoted azide-cycloaddition (SPAAC).

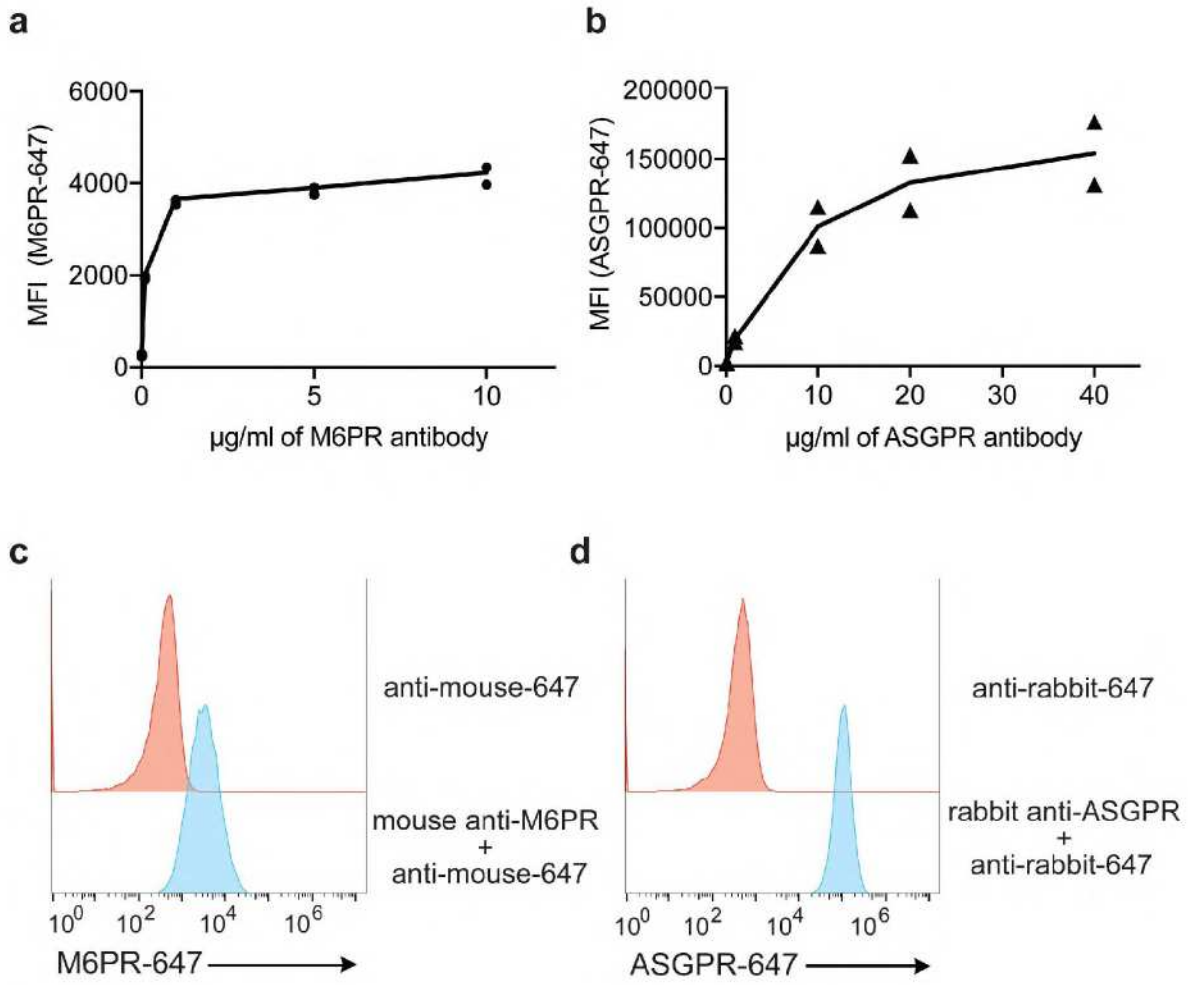

Supplementary Fig. 2. HEPG2 cells express more cell-surface ASGPR than M6PR. anti-M6PR (**a**) or anti-ASGPR (**b**) antibody titration in HEPG2 cells using live-cell flow cytometry to determine antibody saturation. Cell-surface levels of M6PR (**c**) and ASGPR (**d**) were measured in HEPG2 cells using live-cell flow cytometry with saturating concentrations of antibody. 10 µg/ml of anti-M6PR and 20 µg/ml of anti-ASGPR were used. Data are from two independent experiments.

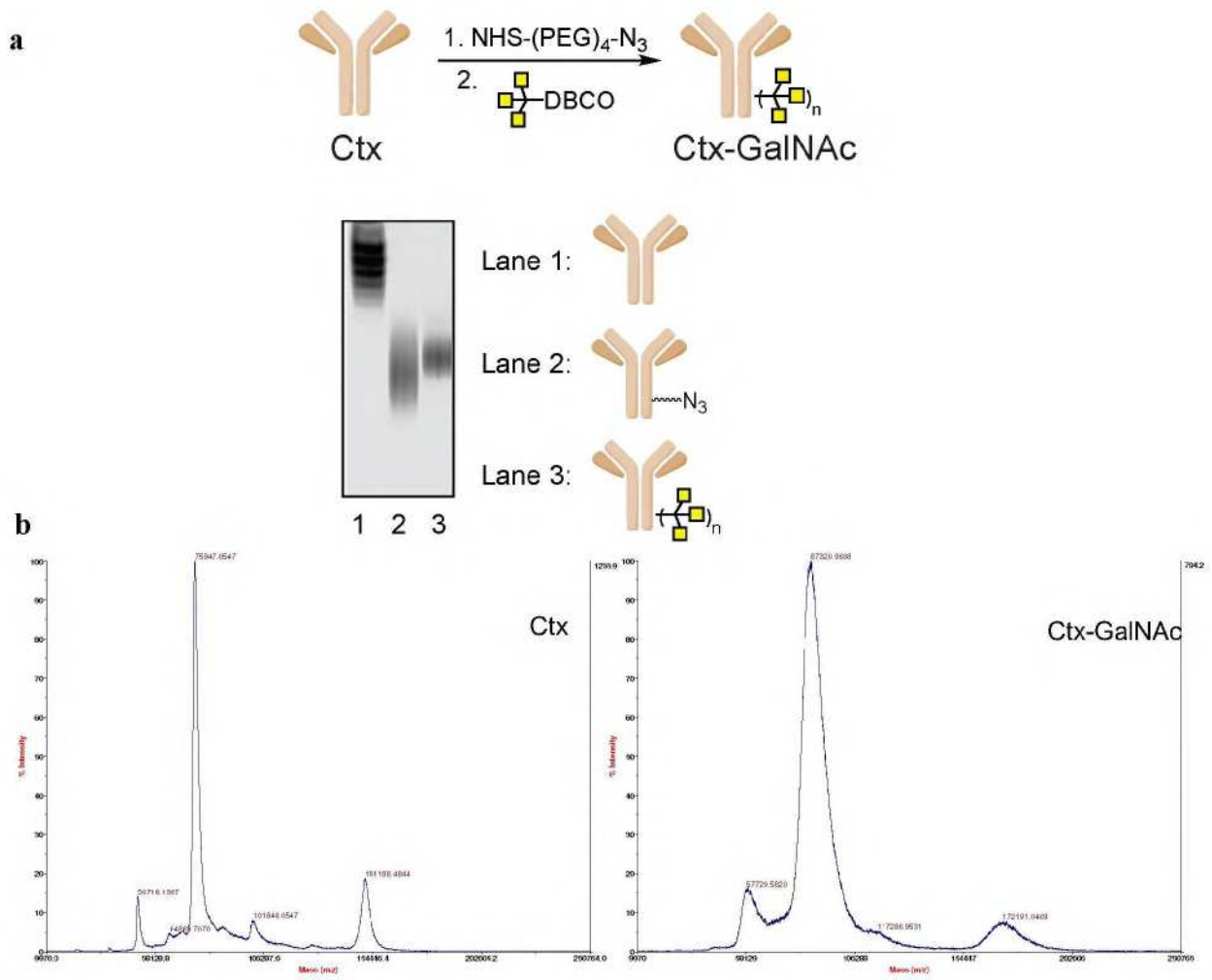

Ligand to Antibody Ratio (LAR) = 10.5

Supplementary Fig. 3. Synthesis of Ctx-GalNAc. a, Ctx was reacted with NHS-$(PEG)_4$-N_3 then with DBCO-tri-GalNAc to yield Ctx-GalNAc. Native gel electrophoresis was used to monitor conversion of Ctx to Ctx-N_3 and Ctx-GalNAc. **b**, MALDI-TOF-MS spectra of Ctx and Ctx-GalNAc, and calculated number of GalNAc ligands per antibody (LAR). The expected mass shift per a single conjugation of NHS-$(PEG)_4$-N_3 and DBCO-tri-GalNAc is 2006.31. The mass shift between Ctx-GalNAc and Ctx was 21,002.56. **a** is a representative data from two independent experiments.

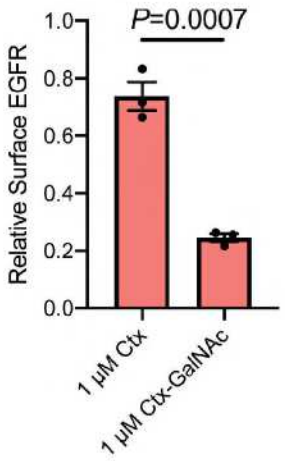

Supplementary Fig. 4. Ctx-GalNAc degrades EGFR at high concentration. Degradation of cell surface EGFR in HEP3B cells determined by live cell flow cytometry following 48 h of treatment with 1 μM Ctx or Ctx-GalNAc. Data are from three independent experiments and are mean ± SEM. *P* values were determined by unpaired two-tailed *t*-tests.

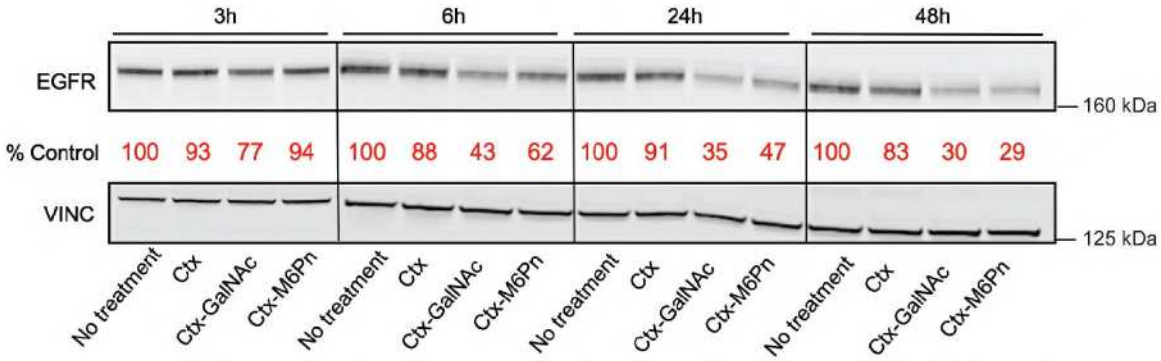

Supplementary Fig. 5. Total EGFR expression decreases over time in HEP3B with LYTAC treatment. Western blot analysis of HEP3B cells incubated with 10 nM cetuximab conjugates for 3, 6, 24, and 48 h. Total EGFR levels were normalized to untreated cells at each time point. Date are representative of two independent experiments.

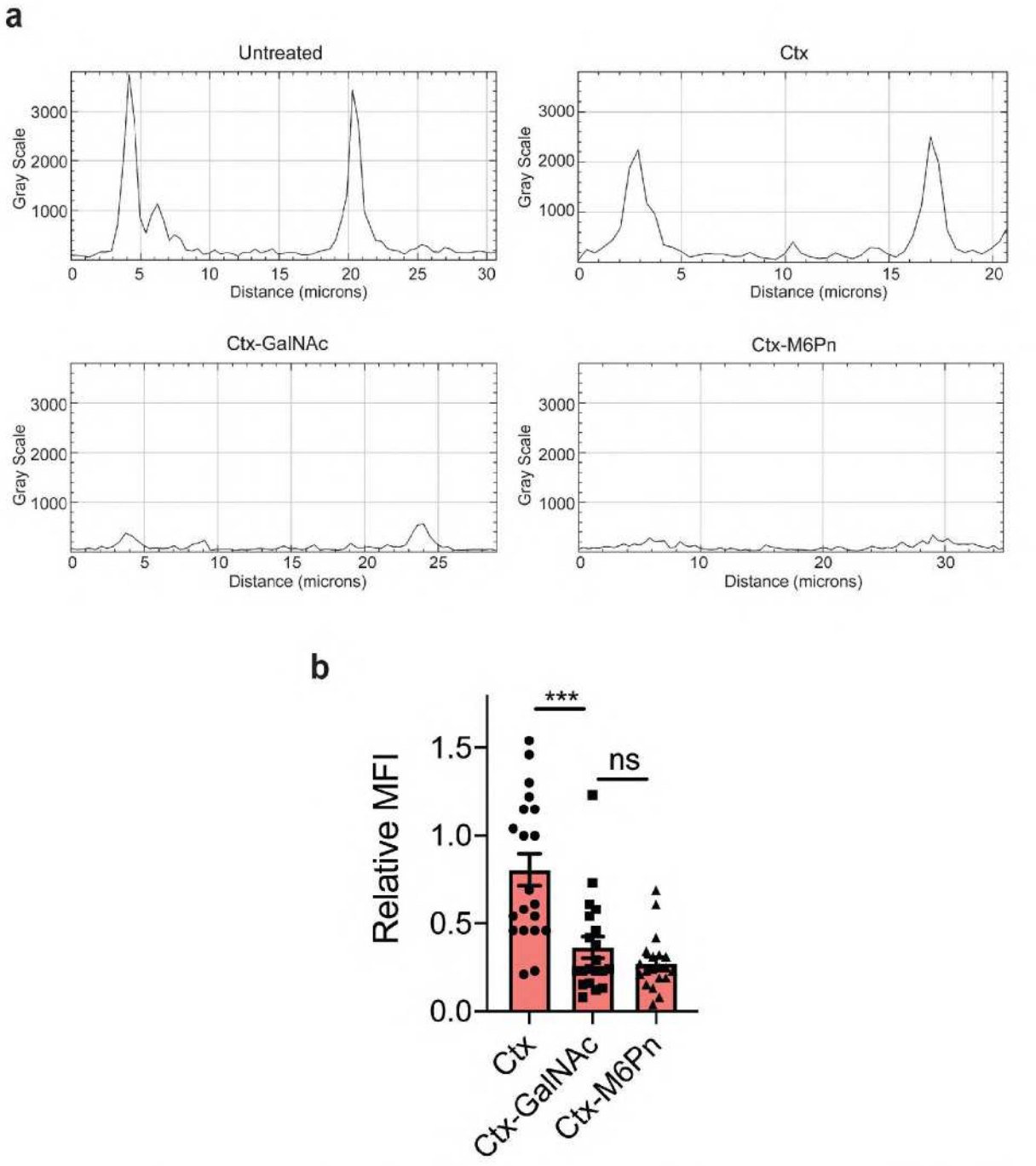

Supplementary Fig. 6. Line-plot quantification of membrane EGFR expression in HEP3B cells. a, Representative line-plot histograms of HEP3B cells treated with 10 nM Ctx conjugates for 48 h. Confocal microscopy was used to visualize cells (Fig. 2F) and the graphs were generated using ImageJ. **b,** Quantification of membrane EGFR signals from line-plot normalized to untreated cells. Values are the average of 20 cells ± SEM. *P* values were determined by unpaired two-tailed *t*-tests.

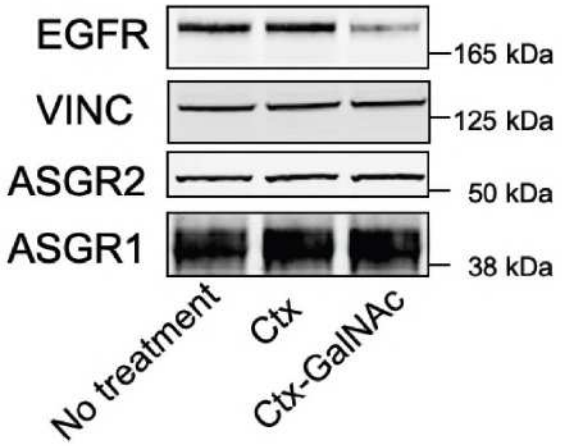

Supplementary Fig. 7. Expressions of both ASGPR subunits are unchanged by Ctx-GalNAc. Western blot of EGFR, vinculin (loading control), and the two subunits of ASGPR – ASGR1 and ASGR2 – following 10 nM treatment of Ctx or Ctx-GalNAc in HEP3B cells after 48 h. Data are representative of two independent experiments.

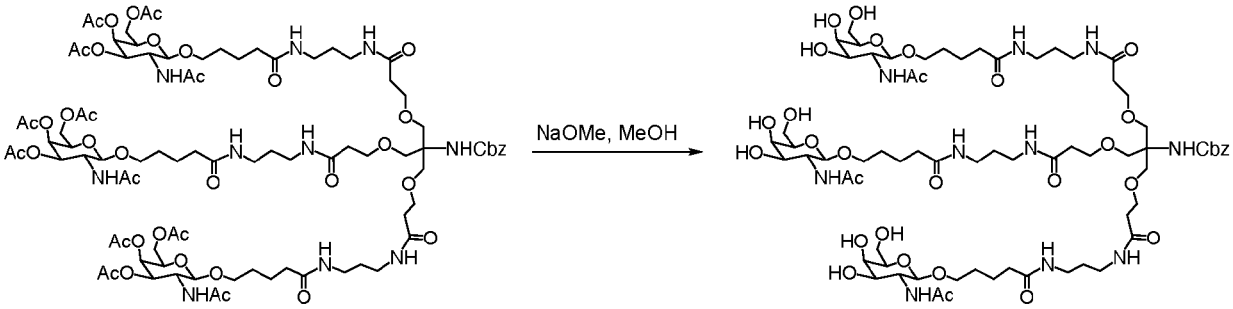

8 **10**

Supplementary Fig. 8. Synthesis of exogenous tri-GalNAc ligand (10).

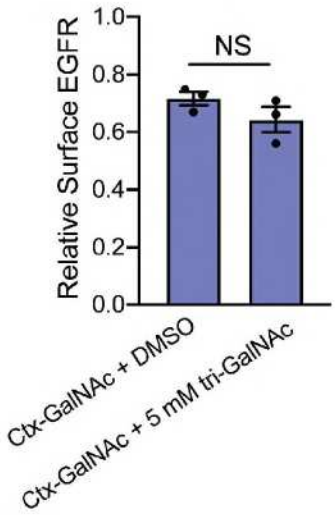

Supplementary Fig. 9. Minor reduction of EGFR upon conjugation in HeLa-GFP is independent of ASGPR. Cell-surface levels of EGFR in HeLa-GFP after co-incubation of 50 nM Ctx-GalNAc and 5 mM exogenous tri-GalNAc (**10**). Data are from three independent experiments and mean ± SEM. *P* values were determined by unpaired two-tailed *t*-tests.

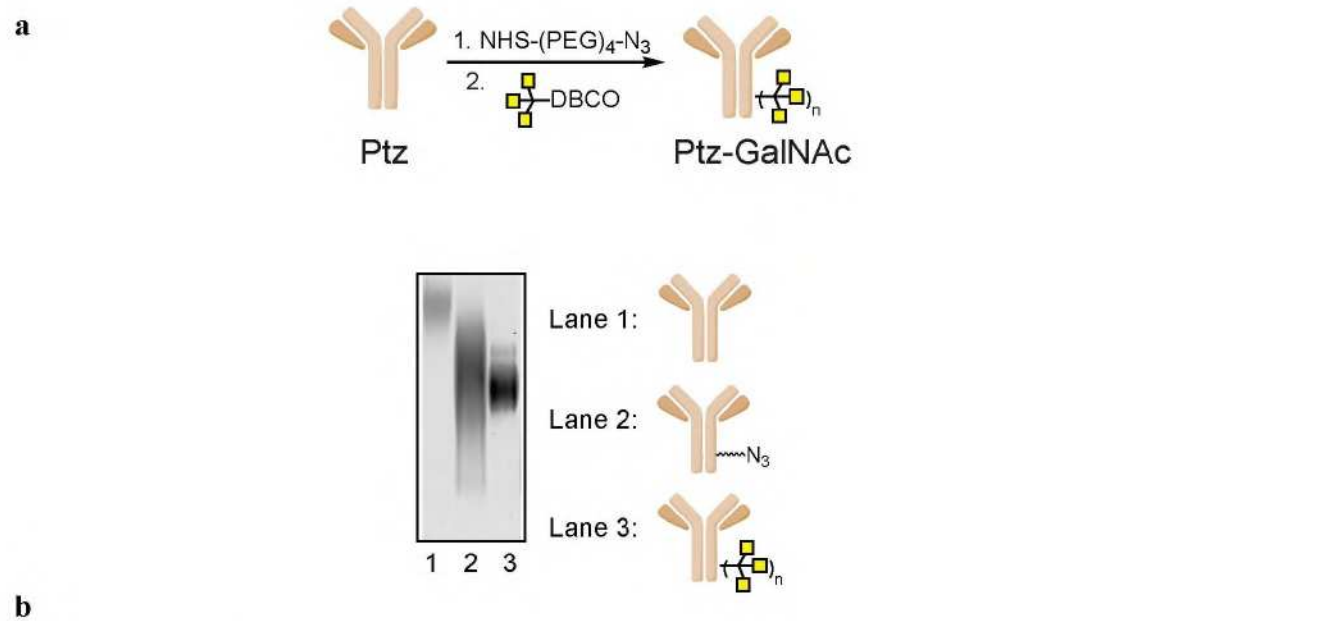

Ligand to Antibody Ratio (LAR) = 11.0

Supplementary Fig. 10. Synthesis of Ptz-GalNAc. a, Ptz was reacted with NHS-$(PEG)_4$-N_3 then with DBCO-tri-GalNAc to synthesize Ptz-GalNAc. Native gel electrophoresis was used to monitor conversion of Ptz to Ptz-N_3 and Ptz-GalNAc. **b**, MALDI-TOF-MS spectra of Ptz and Ptz-GalNAc, and the calculated number of GalNAc ligands per antibody (LAR). The expected mass shift per a single conjugation of NHS-$(PEG)_4$-N_3 and DBCO-tri-GalNAc is 2006.31. The mass shift between Ptz-GalNAc and Ptz was 22,003.47. **a** is a representative data from two independent experiments.

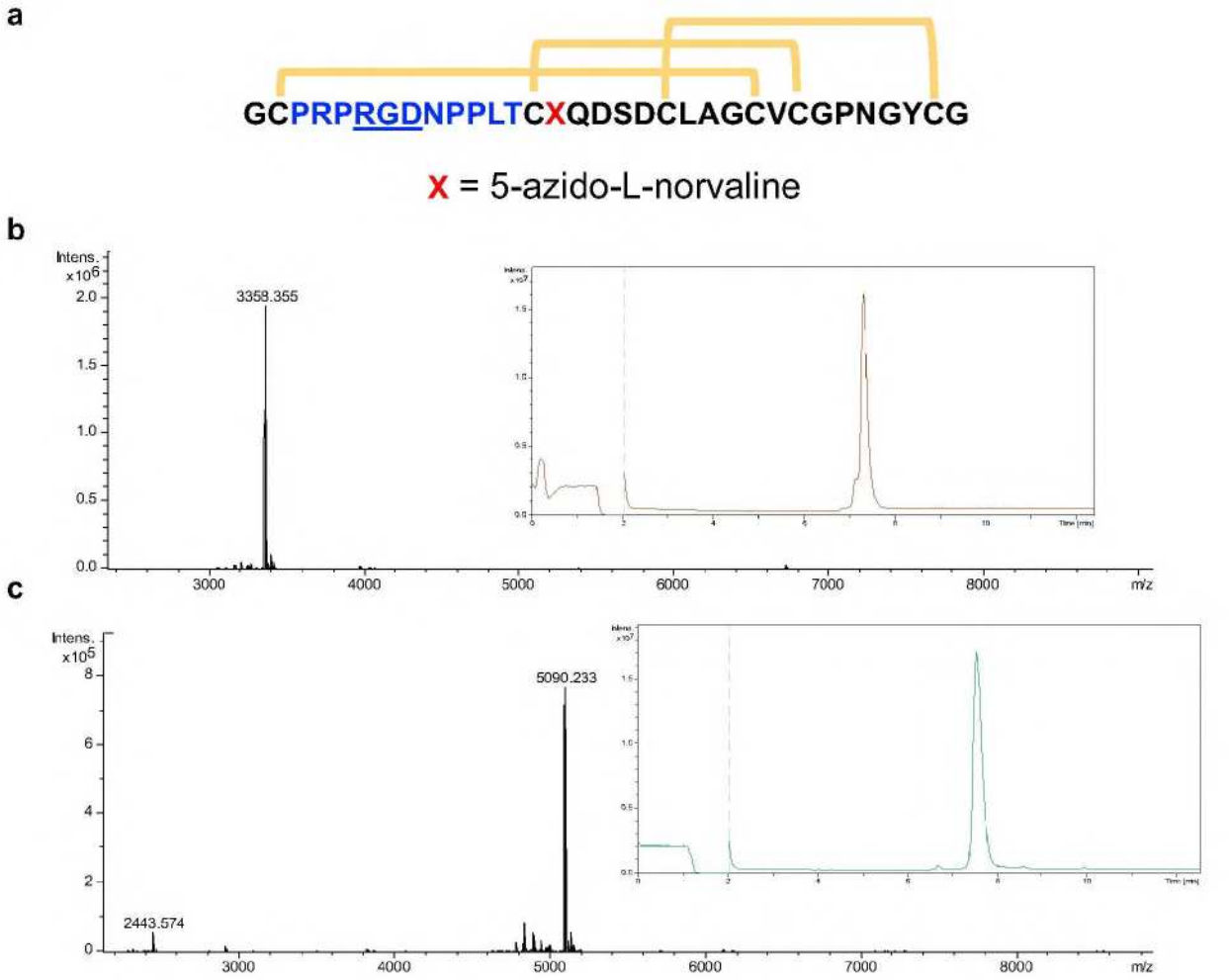

Supplementary Fig. 11. Peptide sequence of PIP and ESI-MS of PIP and PIP-GalNAc. **a**, Peptide sequence of 33-mer PIP knottin. Sequence in blue represents the binding loop with the integrin binding domain underlined, and yellow brackets represent disulfide bridges. 5-azido-L-norvaline was incorporated as a click handle. **b**, Deconvoluted ESI-MS spectrum and total ion chromatogram of PIP. **c**, Deconvoluted ESI-MS spectrum and total ion chromatogram of PIP-GalNAc. Calibration mix (ESI-L Low Concentration Tuning Mix Agilent P/N G1969-85000) was infused during the LC divert step.

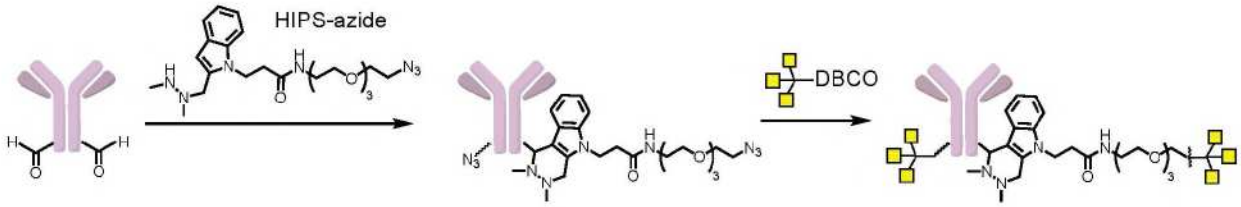

Supplementary Fig. 12. Site-specific conjugation of antibody using the SMARTag technology[43]. Ctx or Ptz was expressed with formylglycine residue in 3 different positions, and was reacted with HIPS-azide[44,45] followed by tri-GalNAc-DBCO **(1)**.

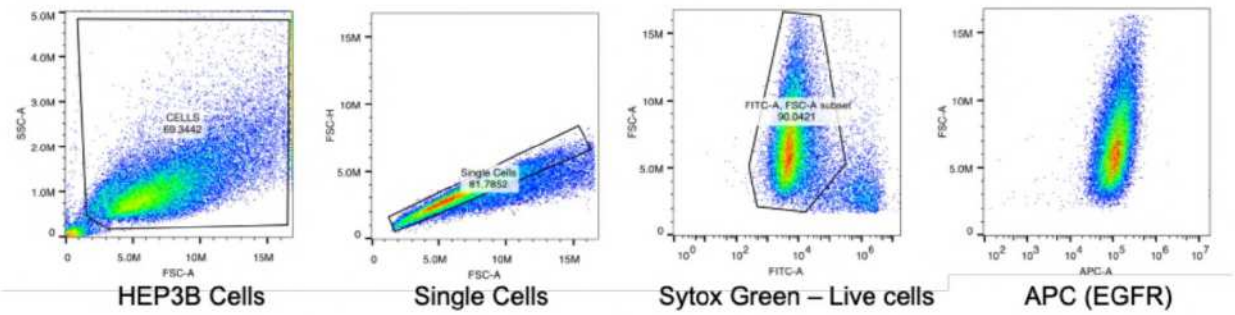

Supplementary Fig. 13. Representative flow cytometry gating for surface EGFR expression in HEP3B cells. HEP3B cells were gated for single cells, then for live cells using Sytox Green. Cells were then analyzed for surface EGFR expression.

Supplementary Fig. 3a

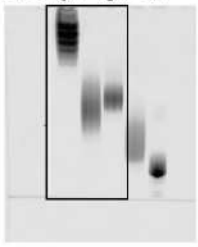

Supplementary Fig. 5 3h

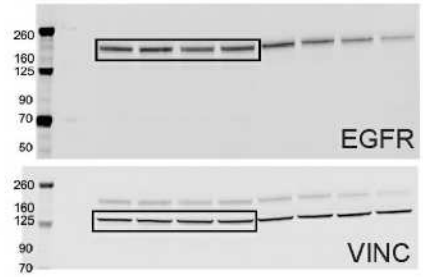

Supplementary Fig. 5 6h, 24h, 48h

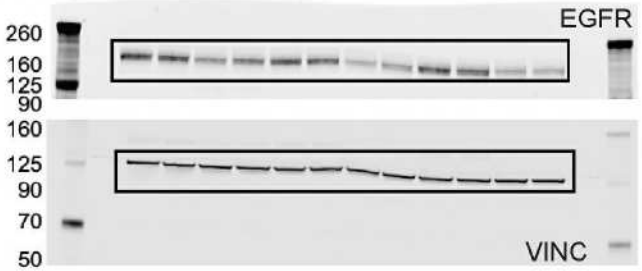

Supplementary Fig. 7

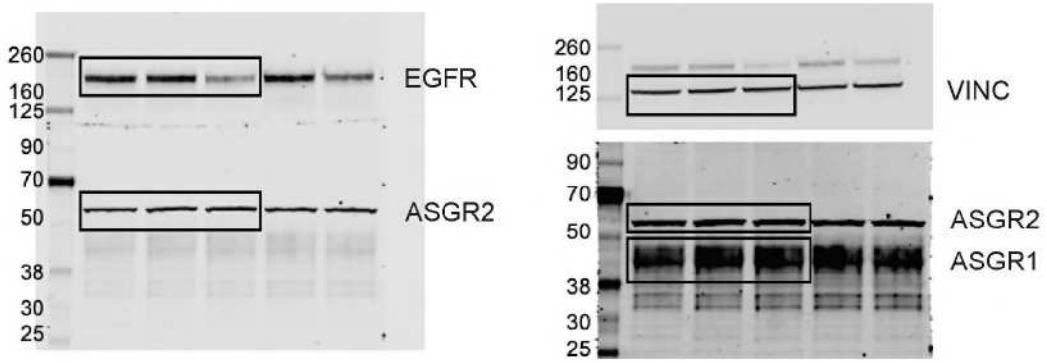

Supplementary Fig. 10a

Unprocessed blots for Supplementary Figures

Supplementary Note 1 - Synthetic Procedures

Synthetic Scheme

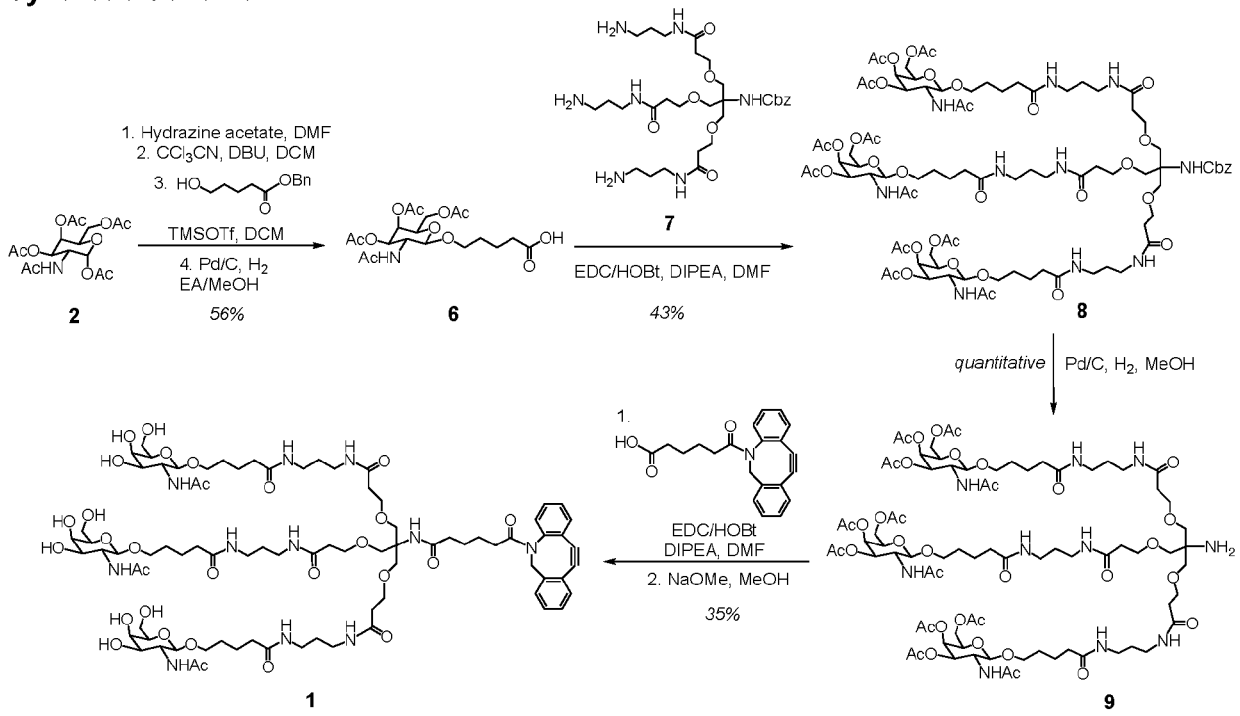

Synthetic Procedures

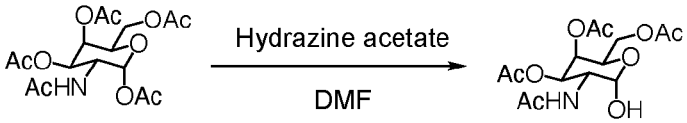

2 **3**

2 (Carbosynth, >95% purity) (5.00 g, 12.8 mmol, 1 equiv.) was dissolved in anhydrous DMF (128 ml, 0.1M) and hydrazine acetate (2.36 g, 25.6 mmol, 2 equiv.) was added to the reaction mixture. The reaction was allowed to stir for 4 hours. Upon completion, the reaction mixture was concentrated under reduced pressure. The resulting residue was purified by flash column chromatography on silica gel (0 → 15% methanol in dichloromethane) to give a white foam (88%). NMR spectra were consistent with previous literature reports[28].

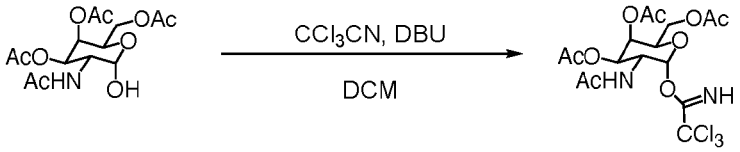

3 **4**

To **3** (4.10 g, 11.8 mmol, 1 equiv) was added anhydrous dichloromethane (150 ml) followed by trichloroacetonitrile (35.4 ml, 354 mmol, 30 equiv.) and DBU (0.60 ml, 3.54 mmol, 0.3 equiv.). The reaction mixture was allowed to stir for 2 hours and concentrated under reduced pressure. The resulting residue was purified by flash column chromatography on silica gel (20 → 100 % ethyl acetate in hexane) to give a yellow foam (75%). NMR spectra were consistent with previous literature reports[28].

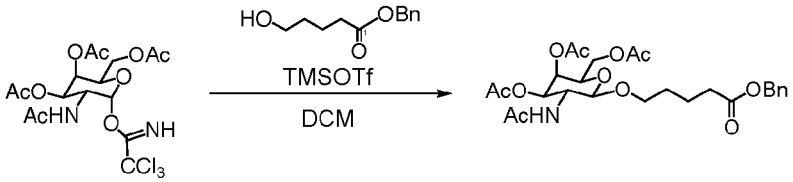

4 **5**

In a flame-dried flask with activated 4Å molecular sieves, **4** (4.35 g, 8.85 mmol, 1 equiv.) and benzyl 5-hydroxypentanoate (3.68 g, 17.7 mmol, 2 equiv.) were added with anhydrous DCM (68 ml, 0.13 M). After stirring for 30 mins, TMSOTf (0.24 ml, 1.33 mmol, 0.15 eq) was added. The reaction was stirred overnight at rt. Upon completion, the reaction was quenched with triethylamine, filtered through celite, and concentrated under reduced pressure. The resulting residue was purified by flash column chromatography on silica gel (30→ 100 % ethyl acetate in hexane) to give a white foam (85%). NMR spectra were consistent with previous literature reports[21].

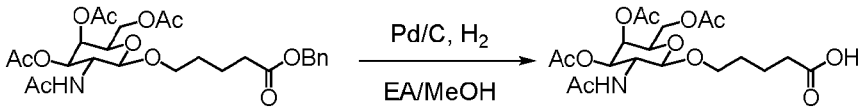

5 **6**

6 was prepared from **5** according to a procedure described previously[21] (quantitative yield).

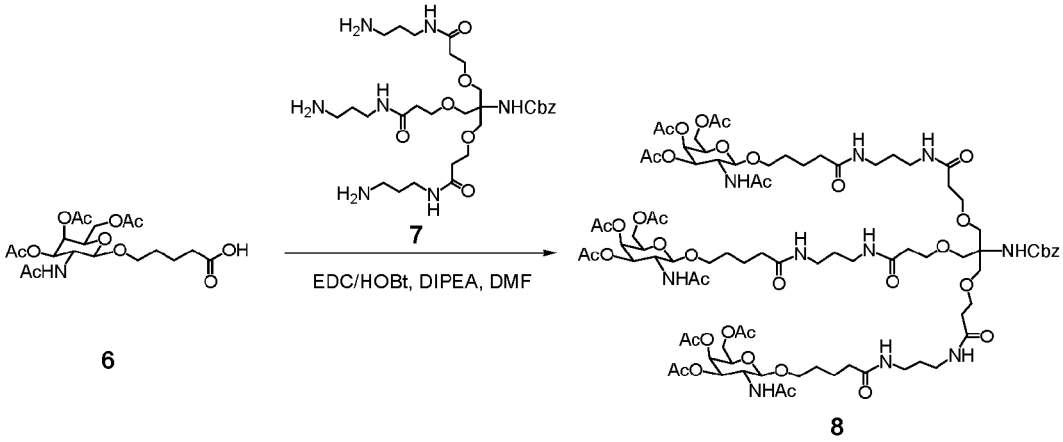

6 **8**

To **6** (1.00 g, 2.24 mmol, 1 equiv.) was added anhydrous DMF (12 ml, 0.2 M), EDC-HCl (1.72 g, 8.95 mmol, 4 equiv.), and HOBt (1.21 g, 8.95 mmol, 4 equiv.). Subsequently, **7** (0.40 g, 0.627 mmol, 0.28 equiv.), synthesized according to the previous literature[21], and DIPEA (3.90 ml, 22.4 mmol, 10 equiv.) were added and the reaction mixture was stirred overnight at rt. The reaction was then concentrated under reduced pressure, diluted with DCM, and extracted with 1 M HCl followed by saturated sodium bicarbonate. The mixture was concentrated and purified by flash column chromatography on silica gel (30 → 100% ethyl acetate in hexane followed by 2 →20% methanol in dichloromethane) (43 %). NMR spectra were consistent with previous literature reports[21].

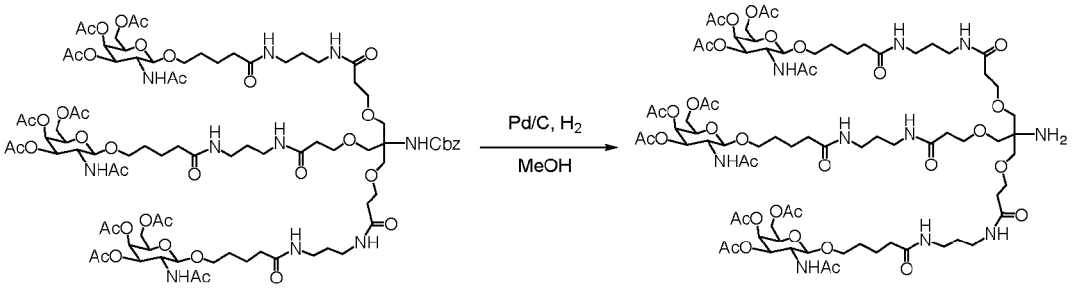

8 **9**

9 was prepared from **8** according to a procedure described previously[21] (quantitative yield).

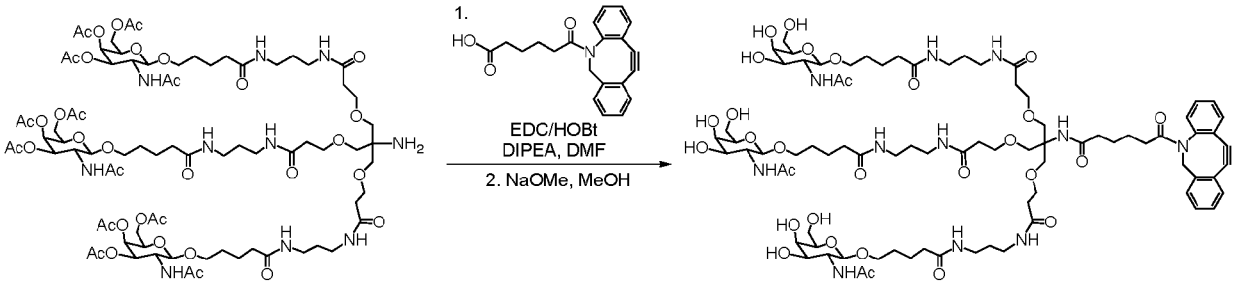

9 **1**

To **9** (1.81 g, 1.01 mmol, 1 equiv.) was added anhydrous DMF (5.0 ml, 0.2 M), EDC-HCl (0.59 g, 3.10 mmol, 3 equiv.) and HOBt (0.41g, 3.1 mmol, 3 equiv.). Subsequently, DBCO-C_6-COOH (0.50 g, 1.51 mmol,1.5 equiv., Click Chemistry Tools) was added. Finally, DIPEA (0.88 ml, ,5.05 mmol, 5 equiv.) was added and the reaction was stirred overnight. The reaction was then concentrated under reduced pressure, diluted with DCM, and extracted with 1 M HCl followed by saturated sodium bicarbonate. The mixture was concentrated and purified by flash column chromatography on silica gel (0 → 20% methanol in dichloromethane). The purified product was dissolved in methanol (0.05 M), and 0.5 M solution of sodium methoxide in MeOH was added to the reaction mixture until the pH reached 9-10. The reaction was allowed to stir for 3 hours. Upon completion, the reaction was quenched with formic acid and concentrated in vacuo. The product was obtained with no further purification (35% over two steps). ^{1}H NMR (400 MHz, Methanol-d_4) δ 7.94 (dt, J = 19.8, 5.7 Hz, 5H), 7.61 (d, J = 7.2 Hz, 1H), 7.52 – 7.38 (m, 4H), 7.34 – 7.19 (m, 4H), 5.10 (d, J = 14.0 Hz, 1H), 4.32 (d, J = 8.4 Hz, 3H), 3.96 – 3.78 (m, 8H), 3.78 – 3.66 (m, 6H), 3.64 – 3.50 (m, 14H), 3.50 – 3.38 (m, 6H), 3.16 (d, J = 6.5 Hz, 12H), 2.30 (t, J = 6.0 Hz, 6H), 2.17 (t, J = 7.5 Hz, 7H), 1.94 (d, J = 6.6 Hz, 9H), 1.69 – 1.48 (m, 17H), 1.34 – 1.17 (m, 6H).^{13}C NMR (126 MHz, Methanol-d_4) δ 175.89, 175.60, 175.11, 174.03, 173.83, 170.40, 152.81, 149.49, 133.37, 130.39, 129.97, 129.61, 129.16, 128.87, 128.05, 126.44, 124.20, 123.52, 115.65, 108.83, 102.99, 76.36, 73.10, 70.08, 69.89, 69.74, 68.57, 62.50, 61.25, 56.57, 49.85, 37.87, 37.80, 37.57, 37.08, 36.64, 35.72, 30.28, 29.92, 26.30, 25.72, 23.62, 23.21. ESI-HRMS Calc'd [M+H$^+$]=1730.8874; found 1730.8878, Calc'd [M+2H^{2+}]=865.9473; found 865.9468.

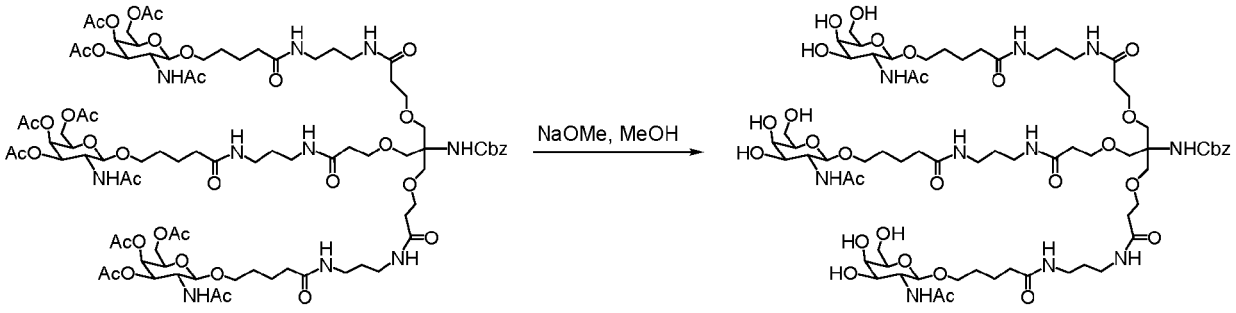

8 **10**

8 was dissolved in methanol (0.05 M), and 0.5 M solution of sodium methoxide in MeOH was added to the reaction mixture until the pH reached 9-10. The reaction was allowed to stir for 3 hours. Upon completion, the reaction was quenched with formic acid and concentrated in vacuo. The product was obtained with no further purification. ^{1}H NMR (400 MHz, Methanol-*d*4) δ 7.95 (dt, *J* = 28.3, 5.7 Hz, 4H), 7.71 – 7.56 (m, 4H), 7.30 (d, *J* = 4.4 Hz, 4H), 7.25 (dt, *J* = 6.0, 2.7 Hz, 4H), 4.99 (s, 3H), 4.32 (d, *J* = 8.4 Hz, 4H), 3.96 – 3.90 (m, 3H), 3.84 (dd, *J* = 10.5, 4.2 Hz, 7H), 3.73 (d, *J* = 5.9 Hz, 8H), 3.61 (dq, *J* = 11.8, 7.6, 5.4 Hz, 16H), 3.47 (t, *J* = 6.1 Hz, 7H), 3.16 (p, *J* = 6.2, 5.7 Hz, 14H), 2.84 (d, *J* = 11.0 Hz, 3H), 2.38 (t, *J* = 5.9 Hz, 6H), 2.16 (t, *J* = 7.4 Hz, 6H), 1.96 (s, 9H), 1.70 – 1.49 (m, 19H). ^{13}C NMR (101 MHz, Methanol-*d*4) δ 174.61, 172.75, 172.56, 128.12, 127.50, 127.44, 124.01, 123.97, 117.35, 111.00, 101.68, 75.01, 71.75, 69.02, 68.78, 68.43, 67.30, 61.18, 58.95, 52.63, 48.52, 48.31, 48.10, 47.89, 47.68, 47.46, 47.25, 47.04, 42.03, 36.50, 36.41, 36.33, 35.30, 28.93, 28.58, 22.27, 21.87. ESI-HRMS Calc'd $[M+H^{+}]$=1549.7982; found 1549.7953, Calc'd $[M+2H^{2+}]$=775.4028; found 775.4009.

^{1}H and ^{13}C NMR spectra

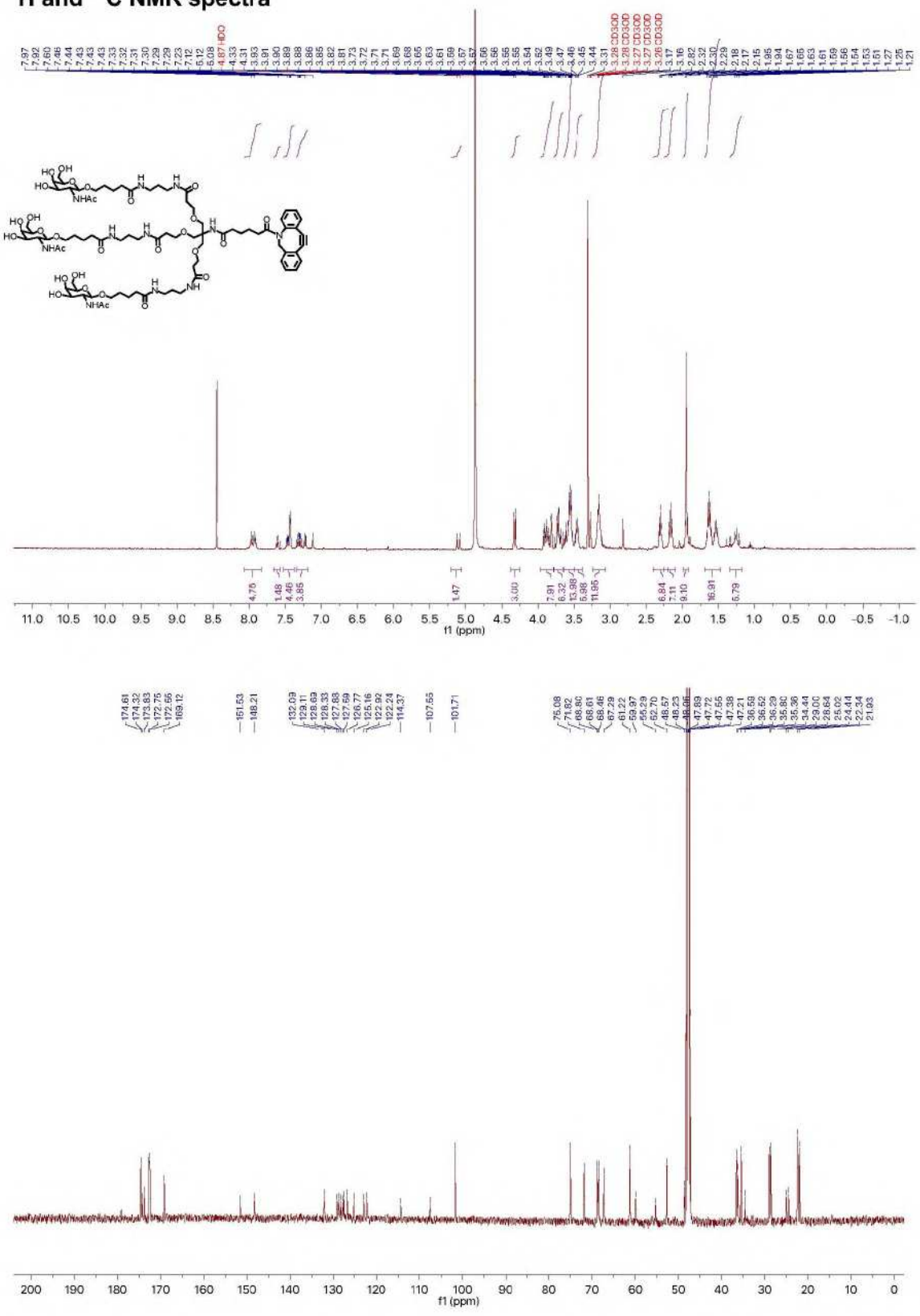

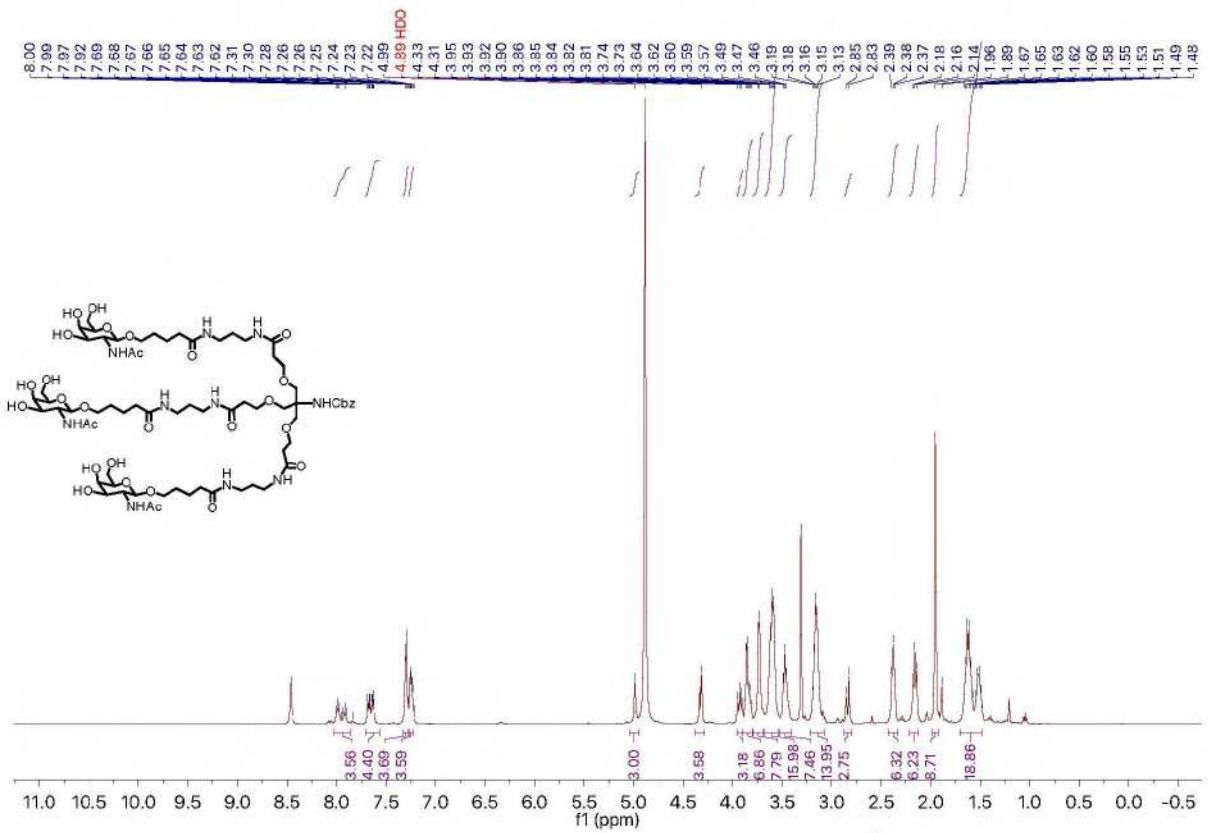
HDO
NHAc
NHCbz
f1 (ppm)

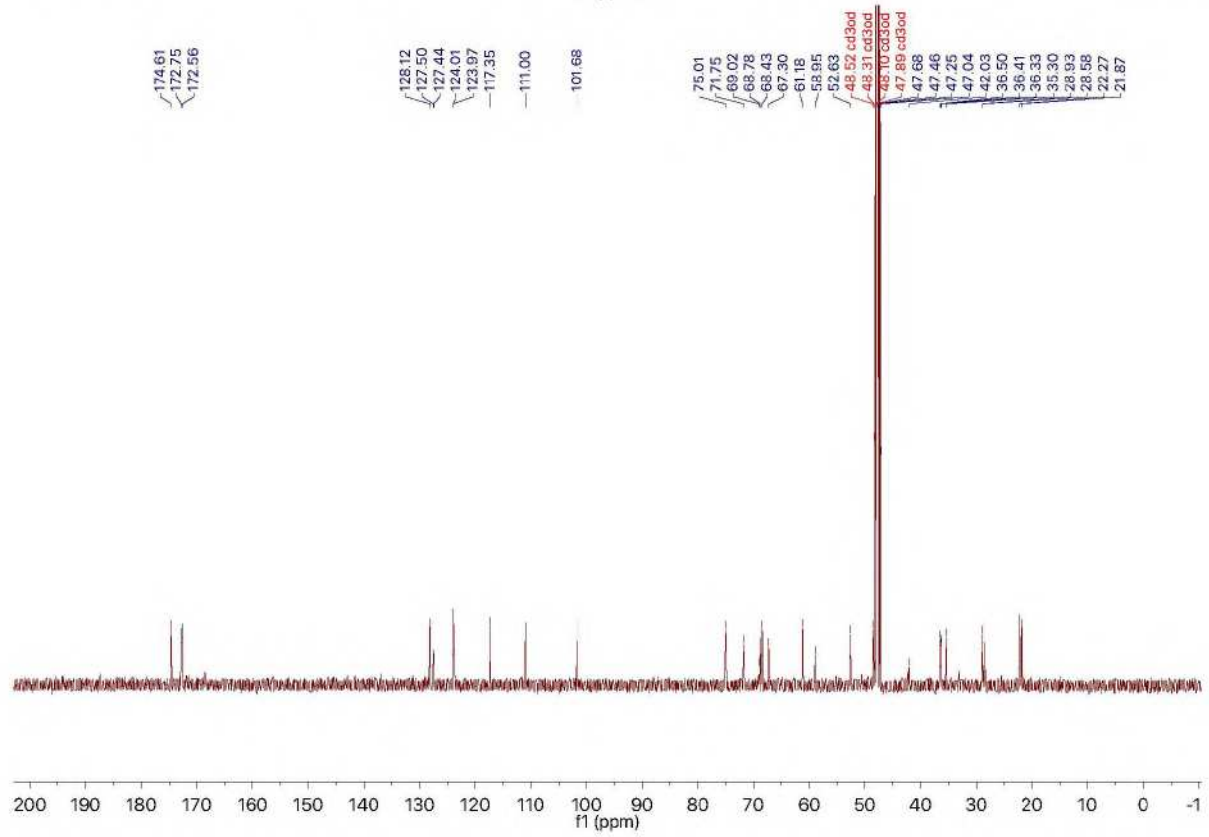
f1 (ppm)

Supplementary Note 2

Amino Acid Sequences for Cetuximab and Pertuzumab with SMARTag

Name	Amino Acid Sequence
Cetuximab heavy chain with C-terminal SMARTag and signal peptide	MGWSCIILFLVATATGVHSQVQLKQSGPGLVQPSQSLSITCTVSGFSLTNYGVH WVRQSPGKGLEWLGVIWSGGNTDYNTPFTSRLSINKDNSKSQVFFKMNSLQSN DTAIYYCARALTYYDYEFAYWGQGTLVTVSAASTKGPSVFPLAPSSKSTSGGTA ALGCLVKDYFPEPVTVSWNSGALTSGVHTFPAVLQSSGLYSLSSVVTVPSSSLG TQTYICNVNHKPSNTKVDKRVEPKSCDKTHTCPPCPAPELLGGPSVFLFPPKPK DTLMISRTPEVTCVVVDVSHEDPEVKFNWYVDGVEVHNAKTKPREEQYNSTYR VVSVLTVLHQDWLNGKEYKCKVSNKALPAPIEKTISKAKGQPREPQVYTLPPSR DELTKNQVSLTCLVKGFYPSDIAVEWESNGQPENNYKTTPPVLDSDGSFFLYSK LTVDKSRWQQGNVFSCSVMHEALHNHYTQKSLSLSPGSLCTPSRGS
Cetuximab heavy chain with Hinge SMARTag and signal peptide	MGWSCIILFLVATATGVHSQVQLKQSGPGLVQPSQSLSITCTVSGFSLTNYGVH WVRQSPGKGLEWLGVIWSGGNTDYNTPFTSRLSINKDNSKSQVFFKMNSLQSN DTAIYYCARALTYYDYEFAYWGQGTLVTVSAASTKGPSVFPLAPSSKSTSGGTA ALGCLVKDYFPEPVTVSWNSGALTSGVHTFPAVLQSSGLYSLSSVVTVPSSSLG TQTYICNVNHKPSNTKVDKRVEPKSCDKTSLCTPSRGSHTCPPCPAPELLGGPS VFLFPPKPKDTLMISRTPEVTCVVVDVSHEDPEVKFNWYVDGVEVHNAKTKPRE EQYNSTYRVVSVLTVLHQDWLNGKEYKCKVSNKALPAPIEKTISKAKGQPREPQ VYTLPPSRDELTKNQVSLTCLVKGFYPSDIAVEWESNGQPENNYKTTPPVLDSD GSFFLYSKLTVDKSRWQQGNVFSCSVMHEALHNHYTQKSLSLSPG
Cetuximab heavy chain with CH-1 SMARTag and signal peptide	MGWSCIILFLVATATGVHSQVQLKQSGPGLVQPSQSLSITCTVSGFSLTNYGVH WVRQSPGKGLEWLGVIWSGGNTDYNTPFTSRLSINKDNSKSQVFFKMNSLQSN DTAIYYCARALTYYDYEFAYWGQGTLVTVSAASTKGPSVFPLAPSSKSTSGGTA ALGCLVKDYFPEPVTVSWNSGASLCTPSRGSLTSGVHTFPAVLQSSGLYSLSSV VTVPSSSLGTQTYICNVNHKPSNTKVDKRVEPKSCDKTHTCPPCPAPELLGGPS VFLFPPKPKDTLMISRTPEVTCVVVDVSHEDPEVKFNWYVDGVEVHNAKTKPRE EQYNSTYRVVSVLTVLHQDWLNGKEYKCKVSNKALPAPIEKTISKAKGQPREPQ VYTLPPSRDELTKNQVSLTCLVKGFYPSDIAVEWESNGQPENNYKTTPPVLDSD GSFFLYSKLTVDKSRWQQGNVFSCSVMHEALHNHYTQKSLSLSPG
Cetuximab light chain with signal peptide	MGWSCIILFLVATATGVHSDILLTQSPVILSVSPGERVSFSCRASQSIGTNIHWYQ QRTNGSPRLLIKYASESISGIPSRFSGSGSGTDFTLSINSVESEDIADYYCQQNN NWPTTFGAGTKLELKRTVAAPSVFIFPPSDEQLKSGTASVVCLLNNFYPREAKV QWKVDNALQSGNSQESVTEQDSKDSTYSLSSTLTLSKADYEKHKVYACEVTHQ GLSSPVTKSFNRGEC
Pertuzumab heavy chain with C-terminal SMARTag and signal peptide	MGWSLILLFLVAVATRVHSEVQLVESGGGLVQPGGSLRLSCAASGFTFTDYTM DWVRQAPGKGLEWVADVNPNSGGSIYNQRFKGRFTLSVDRSKNTLYLQMNSL RAEDTAVYYCARNLGPSFYFDYWGQGTLVTVSSASTKGPSVFPLAPSSKSTSG GTAALGCLVKDYFPEPVTVSWNSGALTSGVHTFPAVLQSSGLYSLSSVVTVPSS SLGTQTYICNVNHKPSNTKVDKKVEPKSCDKTHTCPPCPAPELLGGPSVFLFPP KPKDTLMISRTPEVTCVVVDVSHEDPEVKFNWYVDGVEVHNAKTKPREEQYNS TYRVVSVLTVLHQDWLNGKEYKCKVSNKALPAPIEKTISKAKGQPREPQVYTLP PSRDELTKNQVSLTCLVKGFYPSDIAVEWESNGQPENNYKTTPPVLDSDGSFFL YSKLTVDKSRWQQGNVFSCSVMHEALHNHYTQKSLSLSPGSLCTPSRGS
Pertuzumab heavy chain with Hinge SMARTag and signal peptide	MGWSLILLFLVAVATRVHSEVQLVESGGGLVQPGGSLRLSCAASGFTFTDYTM DWVRQAPGKGLEWVADVNPNSGGSIYNQRFKGRFTLSVDRSKNTLYLQMNSL RAEDTAVYYCARNLGPSFYFDYWGQGTLVTVSSASTKGPSVFPLAPSSKSTSG GTAALGCLVKDYFPEPVTVSWNSGALTSGVHTFPAVLQSSGLYSLSSVVTVPSS SLGTQTYICNVNHKPSNTKVDKKVEPKSCDKTSLCTPSRGSHTCPPCPAPELLG GPSVFLFPPKPKDTLMISRTPEVTCVVVDVSHEDPEVKFNWYVDGVEVHNAKTK PREEQYNSTYRVVSVLTVLHQDWLNGKEYKCKVSNKALPAPIEKTISKAKGQPR EPQVYTLPPSRDELTKNQVSLTCLVKGFYPSDIAVEWESNGQPENNYKTTPPVL DSDGSFFLYSKLTVDKSRWQQGNVFSCSVMHEALHNHYTQKSLSLSPG

Pertuzumab heavy chain with CH1 SMARTag and signal peptide	MGWSLILLFLVAVATRVHSEVQLVESGGGLVQPGGSLRLSCAASGFTFTDYTM DWVRQAPGKGLEWVADVNPNSGGSIYNQRFKGRFTLSVDRSKNTLYLQMNSL RAEDTAVYYCARNLGPSFYFDYWGQGTLVTVSSASTKGPSVFPLAPSSKSTSG GTAALGCLVKDYFPEPVTVSWNSGASLCTPSRGSLTSGVHTFPAVLQSSGLYSL SSVVTVPSSSLGTQTYICNVNHKPSNTKVDKKVEPKSCDKTHTCPPCPAPELLG GPSVFLFPPKPKDTLMISRTPEVTCVVVDVSHEDPEVKFNWYVDGVEVHNAKTK PREEQYNSTYRVVSVLTVLHQDWLNGKEYKCKVSNKALPAPIEKTISKAKGQPR EPQVYTLPPSRDELTKNQVSLTCLVKGFYPSDIAVEWESNGQPENNYKTTPPVL DSDGSFFLYSKLTVDKSRWQQGNVFSCSVMHEALHNHYTQKSLSLSPG
Pertuzumab light chain with signal peptide	MRVPAQLLGLLLLWLPGARCDIQMTQSPSSLSASVGDRVTITCKASQDVSIGVA WYQQKPGKAPKLLIYSASYRYTGVPSRFSGSGSGTDFTLTISSLQPEDFATYYC QQYYIYPYTFGQGTKVEIKRTVAAPSVFIFPPSDEQLKSGTASVVCLLNNFYPRE AKVQWKVDNALQSGNSQESVTEQDSKDSTYSLSSTLTLSKADYEKHKVYACEV THQGLSSPVTKSFNRGEC

DNA Sequences for Cetuximab and Pertuzumab with SMARTag

Name	DNA Sequence
Cetuximab heavy chain with C-terminal SMARTag and signal peptide	ATGGGATGGTCATGTATCATCCTTTTTCTAGTAGCAACTGCAACCGGTGTAC ATTCCCAGGTGCAGCTGAAACAGAGCGGCCCGGGCCTGGTGCAGCCGAGC CAGAGCCTGAGCATTACCTGCACCGTGAGCGGCTTTAGCCTGACCAACTAT GGCGTGCATTGGGTGCGCCAGAGCCCGGGCAAAGGCCTGGAATGGCTGGG CGTGATTTGGAGCGGCGGCAACACCGATTATAACACCCCGTTTACCAGCCG CCTGAGCATTAACAAAGATAACAGCAAAAGCCAGGTGTTTTTTAAAATGAACA GCCTGCAGAGCAACGATACCGCGATTTATTATTGCGCGCGCGCGCTGACCT ATTATGATTATGAATTTGCGTATTGGGGCCAGGGCACCCTGGTGACCGTGAG CGCGGCGAGCACCAAAGGCCCGAGCGTGTTTCCGCTGGCGCCGAGCAGCA AAAGCACCAGCGGCGGCACCGCGGCGCTGGGCTGCCTGGTGAAAGATTAT TTTCCGGAACCGGTGACCGTGAGCTGGAACAGCGGCGCGCTGACCAGCGG CGTGCATACCTTTCCGGCGGTGCTGCAGAGCAGCGGCCTGTATAGCCTCAG CTCGGTGGTGACCGTGCCGAGCAGCAGCCTGGGCACCCAGACCTATATTTG CAACGTGAACCATAAACCGAGCAACACCAAAGTGGATAAACGCGTGGAACC GAAAAGCTGCGATAAAACCCATACCTGCCCGCCGTGCCCGGCGCCGGAACT GCTGGGCGGCCCGAGCGTGTTTCTGTTTCCGCCGAAACCGAAAGATACCCT GATGATTAGCCGCACCCCGGAAGTGACCTGCGTGGTGGTGGATGTGAGCCA TGAAGATCCGGAAGTGAAATTTAACTGGTATGTGGATGGCGTGGAAGTGCAT AACGCGAAAACCAAACCGCGCGAAGAACAGTATAACAGCACCTATCGCGTG GTGAGCGTGCTGACCGTGCTGCATCAGGATTGGCTGAACGGCAAAGAATAT AAATGCAAAGTGAGCAACAAAGCGCTGCCGGCGCCGATTGAAAAAACCATT AGCAAAGCGAAAGGCCAGCCGCGCGAACCGCAGGTGTATACCCTGCCGCC GAGCCGCGATGAACTGACCAAAAACCAGGTGAGCCTGACCTGCCTGGTGAA AGGCTTTTATCCGAGCGATATTGCGGTGGAATGGGAAAGCAACGGCCAGCC GGAAAACAACTATAAAACCACCCCGCCGGTGCTGGATAGCGATGGCAGCTT TTTTCTGTATAGCAAACTGACCGTGGATAAAAGCCGCTGGCAGCAGGGCAA CGTGTTTAGCTGCAGCGTGATGCATGAAGCGCTGCATAACCATTATACCCAG AAAAGCCTGAGCCTGAGCCCGGGCTCTCTCTGCACCCCCTCCCGAGGTTCA TGA
Cetuximab heavy chain with Hinge SMARTag and signal peptide	ATGGGATGGTCATGTATCATCCTTTTTCTAGTAGCAACTGCAACCGGTGTAC ATTCCCAGGTGCAGCTGAAACAGAGCGGCCCGGGCCTGGTGCAGCCGAGC CAGAGCCTGAGCATTACCTGCACCGTGAGCGGCTTTAGCCTGACCAACTAT GGCGTGCATTGGGTGCGCCAGAGCCCGGGCAAAGGCCTGGAATGGCTGGG CGTGATTTGGAGCGGCGGCAACACCGATTATAACACCCCGTTTACCAGCCG CCTGAGCATTAACAAAGATAACAGCAAAAGCCAGGTGTTTTTTAAAATGAACA GCCTGCAGAGCAACGATACCGCGATTTATTATTGCGCGCGCGCGCTGACCT

	ATTATGATTATGAATTTGCGTATTGGGGCCAGGGCACCCTGGTGACCGTGAG CGCGGCGAGCACCAAAGGCCCGAGCGTGTTTCCGCTGGCGCCGAGCAGCA AAAGCACCAGCGGCGGCACCGCGGCGCTGGGCTGCCTGGTGAAAGATTAT TTTCCGGAACCGGTGACCGTGAGCTGGAACAGCGGCGCGCTGACCAGCGG CGTGCATACCTTTCCGGCGGTGCTGCAGAGCAGCGGCCTGTATAGCCTCAG CTCGGTGGTGACCGTGCCGAGCAGCAGCCTGGGCACCCAGACCTATATTTG CAACGTGAACCATAAACCGAGCAACACCAAAGTGGATAAACGCGTGGAACC GAAAAGCTGCGATAAAACCTCTCTCTGCACCCCCTCCCGAGGTTCACATACC TGCCCGCCGTGCCCGGCGCCGGAACTGCTGGGCGGCCCGAGCGTGTTTCT GTTTCCGCCGAAACCGAAAGATACCCTGATGATTAGCCGCACCCCGGAAGT GACCTGCGTGGTGGTGGATGTGAGCCATGAAGATCCGGAAGTGAAATTTAA CTGGTATGTGGATGGCGTGGAAGTGCATAACGCGAAAACCAAACCGCGCGA AGAACAGTATAACAGCACCTATCGCGTGGTGAGCGTGCTGACCGTGCTGCA TCAGGATTGGCTGAACGGCAAAGAATATAAATGCAAAGTGAGCAACAAAGCG CTGCCGGCGCCGATTGAAAAAACCATTAGCAAAGCGAAAGGCCAGCCGCGC GAACCGCAGGTGTATACCCTGCCGCCGAGCCGCGATGAACTGACCAAAAAC CAGGTGAGCCTGACCTGCCTGGTGAAAGGCTTTTATCCGAGCGATATTGCG GTGGAATGGGAAAGCAACGGCCAGCCGGAAAACAACTATAAAACCACCCCG CCGGTGCTGGATAGCGATGGCAGCTTTTTTCTGTATAGCAAACTGACCGTGG ATAAAAGCCGCTGGCAGCAGGGCAACGTGTTTAGCTGCAGCGTGATGCATG AAGCGCTGCATAACCATTATACCCAGAAAAGCCTGAGCCTGAGCCCGGGCT GA
Cetuximab heavy chain with CH-1 SMARTag and signal peptide	ATGGGATGGTCATGTATCATCCTTTTTCTAGTAGCAACTGCAACCGGTGTAC ATTCCCAGGTGCAGCTGAAACAGAGCGGCCCGGGCCTGGTGCAGCCGAGC CAGAGCCTGAGCATTACCTGCACCGTGAGCGGCTTTAGCCTGACCAACTAT GGCGTGCATTGGGTGCGCCAGAGCCCGGGCAAAGGCCTGGAATGGCTGGG CGTGATTTGGAGCGGCGGCAACACCGATTATAACACCCCGTTTACCAGCCG CCTGAGCATTAACAAAGATAACAGCAAAAGCCAGGTGTTTTTTAAAATGAACA GCCTGCAGAGCAACGATACCGCGATTTATTATTGCGCGCGCGCGCTGACCT ATTATGATTATGAATTTGCGTATTGGGGCCAGGGCACCCTGGTGACCGTGAG CGCGGCGAGCACCAAAGGCCCGAGCGTGTTTCCGCTGGCGCCGAGCAGCA AAAGCACCAGCGGCGGCACCGCGGCGCTGGGCTGCCTGGTGAAAGATTAT TTTCCGGAACCGGTGACCGTGAGCTGGAACAGCGGCGCGTCTCTCTGCACC CCCTCCCGAGGTTCACTGACCAGCGGCGTGCATACCTTTCCGGCGGTGCTG CAGAGCAGCGGCCTGTATAGCCTCAGCTCGGTGGTGACCGTGCCGAGCAG CAGCCTGGGCACCCAGACCTATATTTGCAACGTGAACCATAAACCGAGCAA CACCAAAGTGGATAAACGCGTGGAACCGAAAAGCTGCGATAAAACCCATAC CTGCCCGCCGTGCCCGGCGCCGGAACTGCTGGGCGGCCCGAGCGTGTTTC TGTTTCCGCCGAAACCGAAAGATACCCTGATGATTAGCCGCACCCCGGAAG TGACCTGCGTGGTGGTGGATGTGAGCCATGAAGATCCGGAAGTGAAATTTA ACTGGTATGTGGATGGCGTGGAAGTGCATAACGCGAAAACCAAACCGCGCG AAGAACAGTATAACAGCACCTATCGCGTGGTGAGCGTGCTGACCGTGCTGC ATCAGGATTGGCTGAACGGCAAAGAATATAAATGCAAAGTGAGCAACAAAGC GCTGCCGGCGCCGATTGAAAAAACCATTAGCAAAGCGAAAGGCCAGCCGCG CGAACCGCAGGTGTATACCCTGCCGCCGAGCCGCGATGAACTGACCAAAAA CCAGGTGAGCCTGACCTGCCTGGTGAAAGGCTTTTATCCGAGCGATATTGC GGTGGAATGGGAAAGCAACGGCCAGCCGGAAAACAACTATAAAACCACCCC GCCGGTGCTGGATAGCGATGGCAGCTTTTTTCTGTATAGCAAACTGACCGTG GATAAAAGCCGCTGGCAGCAGGGCAACGTGTTTAGCTGCAGCGTGATGCAT GAAGCGCTGCATAACCATTATACCCAGAAAAGCCTGAGCCTGAGCCCGGGC TGA
Cetuximab light chain with signal peptide	ATGGGATGGTCATGTATCATCCTTTTTCTAGTAGCAACTGCAACCGGTGTAC ATTCCGACATCCTGCTCACCCAGAGCCCGGTGATCCTGTCGGTCAGCCCCG GCGAGCGGGTGAGCTTCAGCTGCCGCGCCAGCCAGTCGATCGGGACGAAC ATCCACTGGTACCAGCAGCGGACCAACGGCAGCCCCCGCCTGCTCATCAAG TACGCGAGCGAGAGCATCAGCGGGATCCCCTCGCGGTTCAGCGGCAGCGG

	GAGCGGCACCGACTTCACCCTGAGCATCAACAGCGTGGAGTCGGAGGACAT CGCCGACTACTACTGCCAGCAGAACAACAACTGGCCGACGACCTTCGGCGC CGGGACCAAGCTGGAGCTCAAGCGCACCGTCGCCGCGCCCAGCGTGTTCA TCTTCCCGCCCAGCGACGAGCAGCTGAAGAGCGGCACGGCCAGCGTGGTC TGCCTGCTCAACAACTTCTACCCCCGGGAGGCCAAGGTGCAGTGGAAGGTG GACAACGCCCTGCAGTCGGGGAACAGCCAGGAGAGCGTCACCGAGCAGGA CAGCAAGGACAGCACCTACAGCCTGTCGAGCACCCTCACGCTGAGCAAGGC CGACTACGAGAAGCACAAGGTGTACGCGTGCGAGGTGACCCACCAGGGCC TGAGCAGCCCCGTCACCAAGTCGTTCAACCGCGGAGAATGCTGA
Pertuzumab heavy chain with C-terminal SMARTag and signal peptide	ATGGGTTGGAGCCTCATCTTGCTCTTCCTTGTCGCTGTTGCTACGCGTGTCC ACTCCGAGGTGCAGCTGGTGGAGAGCGGAGGAGGACTGGTGCAGCCTGGA GGATCCCTGAGGCTGAGCTGTGCCGCTTCTGGCTTCACCTTTACAGACTACA CCATGGATTGGGTGCGGCAGGCTCCTGGCAAGGGACTGGAGTGGGTGGCT GATGTGAACCCAAATTCCGGCGGCAGCATCTACAACCAGAGGTTCAAGGGC CGGTTTACCCTGTCCGTGGACAGGAGCAAGAACACACTGTATCTGCAGATG AATAGCCTGAGGGCCGAGGATACCGCCGTGTACTATTGCGCCCGGAATCTG GGCCCCTCTTTCTACTTTGACTATTGGGGCCAGGGCACCCTGGTGACAGTG TCCAGCGCTAGCACCAAGGGCCCATCGGTCTTCCCCCTGGCACCCTCCTCC AAGAGCACCTCTGGGGGCACAGCGGCCCTGGGCTGCCTGGTCAAGGACTA CTTCCCCGAACCGGTGACGGTGTCGTGGAACTCAGGCGCCCTGACCAGCG GCGTGCACACCTTCCCGGCTGTCCTACAGTCCTCAGGACTCTACTCCCTCA GCAGCGTGGTGACCGTGCCCTCCAGCAGCTTGGGCACCCAGACCTACATCT GCAACGTGAATCACAAGCCCAGCAACACCAAGGTGGACAAGAAAGTTGAGC CCAAATCTTGTGACAAAACTCACACATGCCCACCGTGCCCAGCACCTGAACT CCTGGGGGGACCGTCAGTCTTCCTCTTCCCCCCAAAACCCAAGGACACCCT CATGATCTCCCGGACCCCTGAGGTCACATGCGTGGTGGTGGACGTGAGCCA CGAAGACCCTGAGGTCAAGTTCAACTGGTACGTGGACGGCGTGGAGGTGCA TAATGCCAAGACAAAGCCGCGGGAGGAGCAGTACAACAGCACGTACCGTGT GGTCAGCGTCCTCACCGTCCTGCACCAGGACTGGCTGAATGGCAAGGAGTA CAAGTGCAAGGTCTCCAACAAAGCCCTCCCAGCCCCCATCGAGAAAACCAT CTCCAAAGCCAAAGGGCAGCCCCGAGAACCACAGGTGTACACCCTGCCCCC ATCCCGGGATGAGCTGACCAAGAACCAGGTCAGCCTGACCTGCCTGGTCAA AGGCTTCTATCCCAGCGACATCGCCGTGGAGTGGGAGAGCAATGGGCAGC CGGAGAACAACTACAAGACCACGCCTCCCGTGCTGGACTCCGACGGCTCCT TCTTCCTCTACAGCAAGCTCACCGTGGACAAGAGCAGGTGGCAGCAGGGGA ACGTCTTCTCATGCTCCGTGATGCATGAGGCTCTGCACAACCACTACACGCA GAAGAGCCTCTCCCTGTCTCCGGGTTCTCTCTGCACCCCCTCCCGAGGTTC ATGA
Pertuzumab heavy chain with Hinge SMARTag and signal peptide	ATGGGTTGGAGCCTCATCTTGCTCTTCCTTGTCGCTGTTGCTACGCGTGTCC ACTCCGAGGTGCAGCTGGTGGAGAGCGGAGGAGGACTGGTGCAGCCTGGA GGATCCCTGAGGCTGAGCTGTGCCGCTTCTGGCTTCACCTTTACAGACTACA CCATGGATTGGGTGCGGCAGGCTCCTGGCAAGGGACTGGAGTGGGTGGCT GATGTGAACCCAAATTCCGGCGGCAGCATCTACAACCAGAGGTTCAAGGGC CGGTTTACCCTGTCCGTGGACAGGAGCAAGAACACACTGTATCTGCAGATG AATAGCCTGAGGGCCGAGGATACCGCCGTGTACTATTGCGCCCGGAATCTG GGCCCCTCTTTCTACTTTGACTATTGGGGCCAGGGCACCCTGGTGACAGTG TCCAGCGCTAGCACCAAGGGCCCATCGGTCTTCCCCCTGGCACCCTCCTCC AAGAGCACCTCTGGGGGCACAGCGGCCCTGGGCTGCCTGGTCAAGGACTA CTTCCCCGAACCGGTGACGGTGTCGTGGAACTCAGGCGCCCTGACCAGCG GCGTGCACACCTTCCCGGCTGTCCTACAGTCCTCAGGACTCTACTCCCTCA GCAGCGTGGTGACCGTGCCCTCCAGCAGCTTGGGCACCCAGACCTACATCT GCAACGTGAATCACAAGCCCAGCAACACCAAGGTGGACAAGAAAGTTGAGC CCAAATCTTGTGACAAAACTTCTCTCTGCACCCCCTCCCGAGGTTCACACAC ATGCCCACCGTGCCCAGCACCTGAACTCCTGGGGGGACCGTCAGTCTTCCT CTTCCCCCCAAAACCCAAGGACACCCTCATGATCTCCCGGACCCCTGAGGT CACATGCGTGGTGGTGGACGTGAGCCACGAAGACCCTGAGGTCAAGTTCAA

	CTGGTACGTGGACGGCGTGGAGGTGCATAATGCCAAGACAAAGCCGCGGG AGGAGCAGTACAACAGCACGTACCGTGTGGTCAGCGTCCTCACCGTCCTGC ACCAGGACTGGCTGAATGGCAAGGAGTACAAGTGCAAGGTCTCCAACAAAG CCCTCCCAGCCCCCATCGAGAAAACCATCTCCAAAGCCAAAGGGCAGCCCC GAGAACCACAGGTGTACACCCTGCCCCCATCCCGGGATGAGCTGACCAAGA ACCAGGTCAGCCTGACCTGCCTGGTCAAAGGCTTCTATCCCAGCGACATCG CCGTGGAGTGGGAGAGCAATGGGCAGCCGGAGAACAACTACAAGACCACG CCTCCCGTGCTGGACTCCGACGGCTCCTTCTTCCTCTACAGCAAGCTCACC GTGGACAAGAGCAGGTGGCAGCAGGGGAACGTCTTCTCATGCTCCGTGATG CATGAGGCTCTGCACAACCACTACACGCAGAAGAGCCTCTCCCTGTCTCCG GGTTGA
Pertuzumab heavy chain with CH1 SMARTag and signal peptide	ATGGGTTGGAGCCTCATCTTGCTCTTCCTTGTCGCTGTTGCTACGCGTGTCC ACTCCGAGGTGCAGCTGGTGGAGAGCGGAGGAGGACTGGTGCAGCCTGGA GGATCCCTGAGGCTGAGCTGTGCCGCTTCTGGCTTCACCTTTACAGACTACA CCATGGATTGGGTGCGGCAGGCTCCTGGCAAGGGACTGGAGTGGGTGGCT GATGTGAACCCAAATTCCGGCGGCAGCATCTACAACCAGAGGTTCAAGGGC CGGTTTACCCTGTCCGTGGACAGGAGCAAGAACACACTGTATCTGCAGATG AATAGCCTGAGGGCCGAGGATACCGCCGTGTACTATTGCGCCCGGAATCTG GGCCCCTCTTTCTACTTTGACTATTGGGGCCAGGGCACCCTGGTGACAGTG TCCAGCGCTAGCACCAAGGGCCCATCGGTCTTCCCCCTGGCACCCTCCTCC AAGAGCACCTCTGGGGGCACAGCGGCCCTGGGCTGCCTGGTCAAGGACTA CTTCCCCGAACCGGTGACGGTGTCGTGGAACTCAGGCGCCTCTCTCTGCAC CCCCTCCCGAGGTTCACTGACCAGCGGCGTGCACACCTTCCCGGCTGTCCT ACAGTCCTCAGGACTCTACTCCCTCAGCAGCGTGGTGACCGTGCCCTCCAG CAGCTTGGGCACCCAGACCTACATCTGCAACGTGAATCACAAGCCCAGCAA CACCAAGGTGGACAAGAAAGTTGAGCCCAAATCTTGTGACAAAACTCACACA TGCCCACCGTGCCCAGCACCTGAACTCCTGGGGGGACCGTCAGTCTTCCTC TTCCCCCCAAAACCCAAGGACACCCTCATGATCTCCCGGACCCCTGAGGTC ACATGCGTGGTGGTGGACGTGAGCCACGAAGACCCTGAGGTCAAGTTCAAC TGGTACGTGGACGGCGTGGAGGTGCATAATGCCAAGACAAAGCCGCGGGA GGAGCAGTACAACAGCACGTACCGTGTGGTCAGCGTCCTCACCGTCCTGCA CCAGGACTGGCTGAATGGCAAGGAGTACAAGTGCAAGGTCTCCAACAAAGC CCTCCCAGCCCCCATCGAGAAAACCATCTCCAAAGCCAAAGGGCAGCCCCG AGAACCACAGGTGTACACCCTGCCCCCATCCCGGGATGAGCTGACCAAGAA CCAGGTCAGCCTGACCTGCCTGGTCAAAGGCTTCTATCCCAGCGACATCGC CGTGGAGTGGGAGAGCAATGGGCAGCCGGAGAACAACTACAAGACCACGC CTCCCGTGCTGGACTCCGACGGCTCCTTCTTCCTCTACAGCAAGCTCACCG TGGACAAGAGCAGGTGGCAGCAGGGGAACGTCTTCTCATGCTCCGTGATGC ATGAGGCTCTGCACAACCACTACACGCAGAAGAGCCTCTCCCTGTCTCCGG GTTGA
Pertuzumab light chain with signal peptide	ATGAGGGTCCCCGCTCAGCTCCTGGGGCTCCTGCTGCTCTGGCTCCCAGGT GCACGATGTGACATCCAGATGACCCAGTCTCCATCCAGCCTGTCTGCCTCC GTGGGCGACAGGGTGACCATCACCTGTAAGGCCTCCCAGGATGTGAGCATC GGCGTGGCTTGGTACCAGCAGAAGCCAGGCAAGGCCCCCAAGCTGCTGAT CTATTCCGCCTCTTACAGGTACACCGGAGTGCCCTCTCGGTTCTCCGGAAG CGGATCTGGCACAGACTTTACCCTGACAATCTCTTCCCTGCAGCCTGAGGAT TTCGCCACCTACTATTGCCAGCAGTACTATATCTACCCATATACCTTTGGCCA GGGCACAAAGGTGGAGATCAAGCGTACGGTGGCTGCACCATCTGTCTTCAT CTTCCCGCCATCTGATGAGCAGTTGAAATCTGGAACTGCCTCTGTTGTGTGC CTGCTGAATAACTTCTATCCCAGAGAGGCCAAAGTACAGTGGAAGGTGGATA ACGCCCTCCAATCGGGTAACTCCCAGGAGAGTGTCACAGAGCAGGACAGCA AGGACAGCACCTACAGCCTCAGCAGCACCCTGACGCTGAGCAAAGCAGACT ACGAGAAACACAAAGTCTACGCCTGCGAAGTCACCCATCAGGGCCTGAGCT CGCCCGTCACAAAGAGCTTCAACAGGGGAGAGTGTTGA